New Slow Wave Structures for Travelling Wave Tubes

By

Jonathan Hazell

A thesis submitted for the Doctor of Philosophy degree and Diploma of Imperial College London

Imperial College London

Department of Electrical and Electronic Engineering

Optical and Semiconductor Devices Group

2017

__Declaration of Originality__

I hereby declare that that thesis entitled "New slow wave structures for travelling wave tubes", is an original work and any material used from other resources has been appropriately referenced

Jonathan Hazell

Acknowledgements

I would like to express my sincere thanks to Professor Richard Syms for teaching me how to write, proof reading and motivation. Without his help this thesis would not have been possible.

I would also like to thank Ruth for her support and above all else patience whilst I was writing up.

Finally, I would like to thank Professor Stepan Lucyszyn and Dr William Otter for all their help over the years.

Abstract

This thesis covers the design of slow wave structures for travelling wave tubes, with a specific focus on those that could be used for operation at millimetre or shorter wavelengths. Serpentine and a coupled cavity photonic crystal structure are covered in detail, together with the interaction between the electromagnetic waves they support and the electron gun and magnetic beam focusing systems needed for a travelling wave interaction.

In Chapter 2, the existing small-signal theory of the travelling wave interaction is introduced and applied to a serpentine travelling wave tube. A set of synthesis equations for the serpentine structure are then derived from the analysis and verified with simulation. In Chapter 3, possible improvements to the serpentine structure for high frequency operation, and operation on harmonics other than the fundamental (for both the phase and the interaction impedance) are considered. From the investigation it can be concluded that higher harmonics allow a larger beam current than the fundamental. In Chapter 4, slow wave structures based on photonic crystals are proposed for use in travelling wave tubes. A specific photonic crystal arrangement – the coupled resonator optical waveguide (CROW) - that does not appear to have been studied previously in this application is then investigated. The conclusion is that a CROW is suitable for use in a travelling wave tube and is significantly more manufacturable than existing approaches. In Chapter 5, the design of a full electron beam system for use with both the original and the improved slow wave structures is presented. The design of an electron gun, cathode and collimating magnet using an immersed flow insertion are all covered in detail. In Chapter 6, conclusions are drawn and avenues for possible future work are presented.

Table of Contents

List of Figures

15

List of Tables

List of Symbols

μ_0	Permeability of free space [H/m]
Γ_c	Complex propagation constant of the circuit [rad/s]
B_z	Magnetic field strength to contain a beam at the Brillouin limit [T]
C_u	Per-unit-length capacitance [F]
I_0	Current of electron beam [A]
I_w	Current in the solenoid windings [A]
K_{ab}	Ratio between a and b
K_{pb}	Ratio between p and b
L_n	Length per period, normalised to a
L_u	Per-unit-length inductance [H]
N_p	Number of integer periods
$P_C(T)$	Power of conductive cooling, dependant on temperature T [W]
$P_E(T)$	Power of emitted electrons, dependant on temperature T [W]
$P_R(T)$	Power of radiative cooling, dependant on temperature T [W]
$P_T(I)$	Power from restive heating of the cathode, dependant on heater current I [W]
R_a	Anode radius [m]
R_c	Cathode radius [m]
$R_{cathode}$	Resistance of the cathode wire [Ω]
V_0	Accelerating voltage of electron beam [V]
V_z	Voltage on the circuit [V]
Z_w	Impedance of waveguide [Ω]
Z_w	Impedance of the waveguide [Ω]
b_0	Tunnel opening width [m]
b_m	Beam minimum [m]
d_b	Beam tunnel diameter (serpentine waveguide) [mm]
f_c	Cutoff frequency of the waveguide [Hz]
f_{max}	Operating point of the waveguide [Hz]
f_{op}	Operating frequency [Hz]
i_z	Beam current [A]
k_1	Constant $\left(\frac{cp_n}{L_n}\right)$
k_2	Constant $\left(\frac{1+2n}{L_n}\right)$
k_{wall}	Minimum machinable waveguide wall thickness
m_e	Mass of an electron [Kg]
p_n	Period, normalised to a
r_b	Beam radius [m]
r_c	Axial cathode radius [m]
s_n	Straight length, normalised to a
u_0	Electron beam velocity [m/s]
v_T	Phase velocity of the wave along the beam tunnel [m/s]
v_{beam}	Normalised electron beam velocity [c]
v_p	Phase velocity of the circuit [m/s]
z_{offset}	Difference in position between solenoid and electrodes [m]
β_T	Phase constant of the wave along the beam tunnel [rad/m]
β_c	Phase constant of the circuit [rad/s]
β_e	Phase constant of the electron beam [rad/m]

β_w	Propagation constant along a waveguide [rad/m]
ε_ρ	Cathode emissivity
λ_T	Wavelength of the wave along the beam tunnel [m]
λ_c	Wavelength in free space [m]
ω_{op}	Operating angular frequency [rad/s]
ϵ_0	Permittivity of free space [F/m]
ϕ_T	Phase shift between beam crossings [rad]
Γ	Complex propagation constant of the travelling wave [rad/m]
A	Pierce coupling loss [dB]
A	Cross sectional area [m²]
B	Pierce propagation parameter
C	Pierce gain parameter [dB]
F	Force [N]
G	Gain of the tube (Pierce) [dB]
K	Arbitrary constant
L	Length per period (serpentine waveguide) [m]
L	Length of the wire [m]
N	Number of turns on solenoid
P	Perveance
Q	Space charge parameter
R	Resistance [Ω]
R	Radius of the solenoid [m]
S	Surface area [m²]
T	Temperature [K]
X	Normalised cathode length
Y	Slot beam tunnel length [m]
a	Waveguide width (serpentine waveguide) [m]
a	Constant $a = \frac{S\epsilon\sigma L^2}{Ak}$
a	Equilibrium radius of electron beam under Brillouin flow [m]
b	Waveguide height (serpentine waveguide) [m]
b	Normalised difference between phase velocity of circuit and beam (Pierce)
b	Constant $b = \frac{\alpha I^2 L^2}{kA^2}$
c	Speed on light [m/s]
c	Constant $c = \frac{\rho I^2 L^2}{kA^2}$
d	Ratio between β_T and b [rad]
d	Pierce loss parameter
e	Charge of an electron [C]
k	Thermal conductivity [W/mK]
l	Length of the solenoid [m]
p	Period length (serpentine waveguide) [m]
q	Charge [C]
s	Straight length (serpentine waveguide) [m]
v	Velocity [m/s]
x	Position along the filament [m]
α	Temperature dependant resistivity [Ω/K]
β	Phase constant [rad/s]
η	Electron charge to mass ratio [C/kg]

θ	Cathode angle [degrees]
κ	Interaction impedance [Ω] n.b Pierce uses Z_0 here
λ	Guide wavelength [m]
ρ	Resistivity [Ω/m]
σ	Stefan-Boltzmann constant [Wm^{-2}K^{-4}]
ω	Angular frequency [rad/s]

List of Abbreviations

TWT	Travelling Wave Tube
SWS	Slow Wave Structure
PC	Photonic Crystal
CROW	Coupled Resonator Optical Waveguide
TV	Television
EIK	Extended Interaction Klystron
EM	Electromagnetic
CAD	Computer Aided Design
PIC	Particle in Cell

1   Introduction

The modern world has an insatiable desire for wireless data transfer, causing the currently utilised radio spectrum to become increasingly crowded. Higher bit rates are also demanded, requiring larger channel bandwidths. Both these problems can be solved, by exploiting the under-utilised higher frequency parts of the spectrum. For example, the entire consumer spectrum up to 3 GHz (covering, Wi-Fi, TV, broadcast radio, amateur radio and mobile phones) only represents 3 % bandwidth at W-band. Consequently, there has been a major effort to extend the operating frequency of existing microwave devices.

The higher frequency parts of the spectrum have significantly larger atmospheric attenuation, thus requiring high power devices to compensate. Unfortunately, the operating frequency of a microwave device is linked to its size. Consequently, practical devices for high frequency communication links must have a power density proportional to their operating frequency.

Whilst solid-state devices have dominated the power amplifier market, this new need for high power density has caused a resurgence in vacuum tube devices (so called because they contain an electron beam that must be operated in a vacuum) due to their natural power handling capability. The advantage that vacuum tube devices have over solid-state devices for high frequency, high power operation can clearly be seen when comparing current state of the art devices. For example, a recent solid-state design [1] only provided 1 W of continuous power at 94 GHz, compared to 2 kW from a similarly modern Extended Interaction Klystron (EIK) device [2].

Within the family of vacuum tube amplifiers that have found commercial acceptance there are several types of device, normally categorised according to the nature of the interaction between the electron beam and EM wave: linear beam, crossed field and fast wave. Within the topic of high frequency operation, the most important fast wave device is the Gyrotron. More variety exists among linear beam devices which can broadly be split into travelling wave devices and Klystrons. A popular type of high frequency tube, the extended interaction Klystron, is a refined combination of those two separate

approaches. The most common example of a crossed field tube is a Magnetron. A brief summary of all of these types of tubes follows.

A Gyrotron is capable of producing extremely high output power at millimetre frequencies, for example a Gyrotron used in the W7-X fusion reactor [3] gives 0.92 MW at 140 GHz over a 1800s pulse. Development of Gyrotrons has been spurred on by fusion research, where they are used for plasma heating. The operating principle behind a Gyrotron is the cyclotron maser instability [4], which can be described as follows. An electron beam is injected into an area of extremely high magnetic field (of the order of 10 T) causing the cyclotron frequency of the electron to be so high that a significant part of the electron's kinetic energy is rotational (implying that the electron's path is a tightly wound corkscrew). The electrons then pass into a microwave cavity, which has a resonant mode (usually a higher order mode) of the correct frequency to couple strongly with the rotating electrons. Figure 1.1 shows a labelled diagram of a Gyrotron.
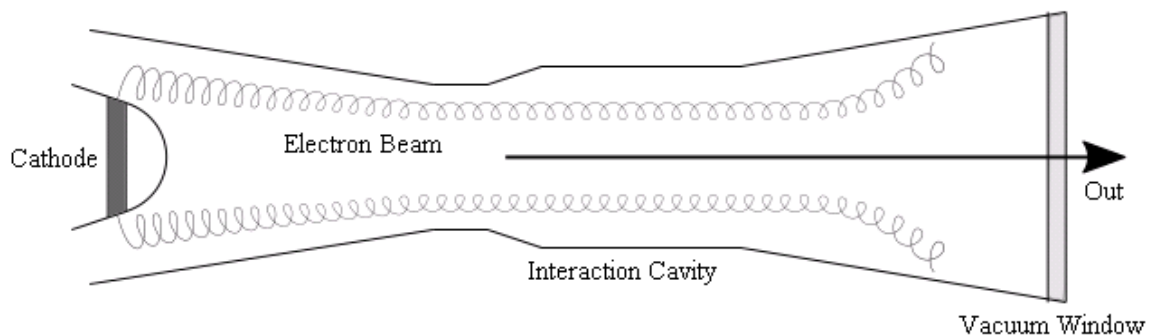
Figure 1.1 - Labelled diagram of a Gyrotron.

However, the cyclotron frequency of the electrons is linked to the strength of the magnetic field applied. Whilst higher harmonics can be used, the maximum operating frequency of a Gyrotron is fundamentally limited by magnet technology. Typical production devices use superconducting magnets, making the device physically large and expensive – consequently, an airborne phased array using Gyrotrons is extremely unlikely. These issues mean that research has continued to be carried out on millimetre-wave versions of conventional slow wave devices such as travelling wave tubes (TWTs) and klystrons.

A TWT is a linear beam device containing a slow wave structure that supports an electromagnetic (EM) wave, which passes through the device at the same speed as the electron beam. Because the velocity difference between the beam and wave is low, they can easily perturb each other. With the correct design a significant amount of power can be transferred from the beam into the EM wave, thus allowing amplification. The first slow wave structure used was a helix, with the beam passing through the centre, and is still used today as it offers excellent bandwidth. However other slow wave structures are used for more specialised devices, with coupled cavity slow wave structures offering higher output power at the expense of bandwidth. At very high frequencies (over 100 GHz) the helix is no longer viable (since the wire used to wind it becomes too small, limiting power handling and increasing manufacturing difficulties) so alternative slow wave structures have been investigated. Figure 1.2 shows a diagram of a TWT with the electron beam, slow wave structure and RF ports labelled.
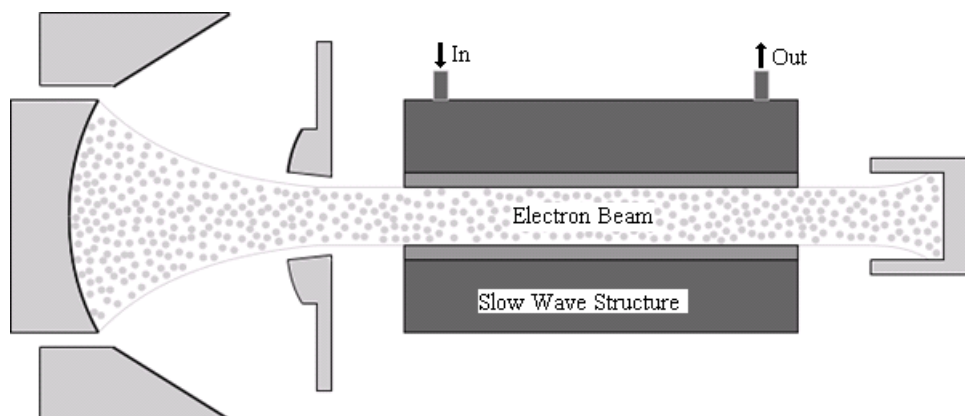
Figure 1.2- Labelled diagram of a travelling wave tube.

A Klystron is a rather different linear beam-type device containing a set of cavities placed along the electron beam. There is no direct microwave path, so microwave power would not propagate between the input and output couplers in the absence of an electron beam (this is a key distinguishing feature between a klystron and a coupled cavity travelling wave tube). The first cavity in the chain is excited using the input coupler, with the electric field in the cavity inducing a current in the electron beam that results in bunches of electrons forming. The bunching then excites subsequent cavities, which in turn induce currents in the beam that cause further bunching. The power is then coupled out of the structure

by a cavity containing a coupling loop, in the same fashion as the input coupler. Figure 1.3 shows a diagram of a Klystron with the electron beam, cavities and RF ports labelled.
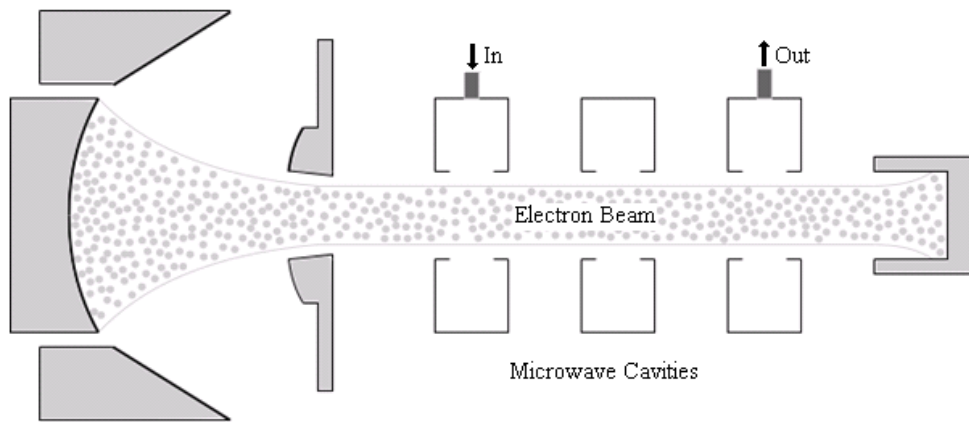
Figure 1.3 - Labelled diagram of a Klystron.

Whilst capable of high output power, a Klystron is fundamentally a limited bandwidth device. In addition, at high frequencies the cavities become increasingly difficult to manufacture. Some of these limitations are overcome using the Extended Interaction Klystron, broadly describable as a combination of a TWT and a Klystron, although it still suffers from limited bandwidth.

The final main category of classical microwave tubes are crossed field devices, the most well-known example being a magnetron. The key difference between crossed field devices and the tubes presented earlier is that the magnetic field is perpendicular (rather than parallel) to the direction of electron motion. Figure 1.4 shows the basic configuration of a magnetron with the cathode, anode and resonant cavities labelled, the magnetic field is out of the page. The accelerating field causes electrons to initially travel radially, however the magnetic field imparts a tangential force on the electrons resulting in a spiral path. When an RF field is introduced 'spoke' like bunches form which can then be used to extract energy from the electron velocity into the RF field.
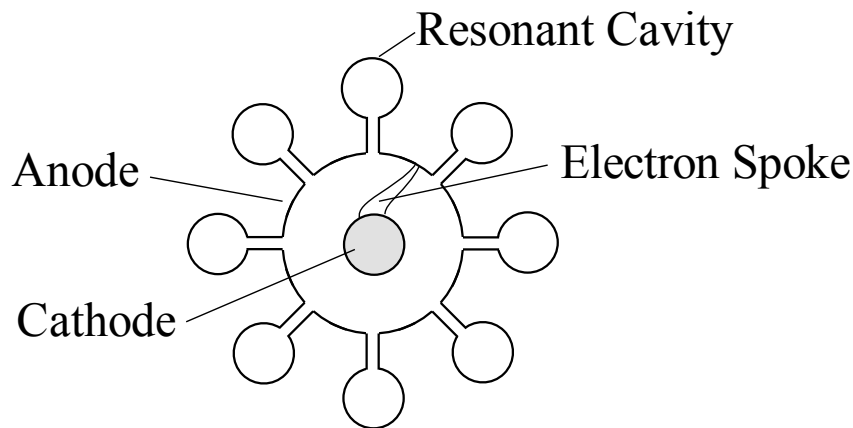
Figure 1.4 – Labelled diagram of a magnetron, magnetic field is out of the page.

In a magnetron the RF circuit is a series of coupled resonant cavities placed along the anode such that the entire structure resonates at a single frequency but that the electric field in adjacent cavities is opposed. As a spoke rotates around the cathode it interacts with the electric field from the cavities, if the electric field oscillation and cavity spacing are synchronised to the spoke rotation then the spoke sees a net force and power is transferred from the electrons into the RF field in the cavities.

In a Crossed field amplifier, the interaction cavities are designed such that the EM wave travels around the outside of the structure in synchronisation with the electron spoke allowing an interaction similar to that in a TWT to occur.

The main types of vacuum tubes used for millimetre-wave operation have now been presented. The travelling wave tube, the focus of this thesis, will be covered in more detail in the next section.

1.1   History of TWT Development

The invention of the travelling wave tube is normally attributed to Kompfner, Lindenblad or Haeff [5][6], who discovered the effect at similar times using a helix as the slow wave structure. Pierce and Fields working at Bell telephone labs developed the design further [7]. An excellent description of the early history and more recent developments has been published by Gilmour [8]. However, as the frequency increases, helices encounter problems with power dissipation and eventually become

extremely difficult to manufacture (although recent efforts have reported operating frequencies up to 46 GHz [9]). Consequently, a different slow wave structure is required.

A suitable structure is provided by the serpentine (or folded waveguide) TWT, which has attracted considerable research interest for high frequency operation. Originally designed by Dohler [10], it has several key advantages over a helix. The most important is that as a waveguide structure it is significantly stronger, and can be cooled much more effectively. In addition it can be described as a pseudo two-dimensional (2D) structure, and can be machined using conventional techniques for manufacturing split block waveguides. Following the first reports in the literature, the operating frequency of serpentine TWTs has steadily increased [11]. However as the size of the slow wave structure must shrink in proportion to its operating frequency, conventional machining techniques cannot fabricate mm-wave TWTs and micromachining techniques must be used.

Micromachining of travelling wave tubes began around the turn of the millennium. Ives provides a good summary of the early efforts and possibilities in [12], generally based on some combination of lithographic patterning and high-aspect-ratio etching. Bhattacharjee first proposed using a micro-fabricated serpentine waveguide for a THz travelling wave tube in 2004 [13]. Since then, many groups [14][15][16] have fabricated and measured devices of this style around W band (possibly due to the availability of measurement equipment). The Naval Research Lab (USA) presented an all-metal 220 GHz design fabricated using the German LIGA (Lithographie, Galvanoformung, Abformung) process, which involves electroforming metal parts inside a high-aspect ratio photoresist mould patterned using synchrotron radiation [17]. L-3 Communications show a commercially available 94 GHz serpentine TWT producing 100 W power over a 4 GHz bandwidth [18]. There was also a pan European effort to develop a 1 THz vacuum device using a double corrugated rectangular waveguide called OPTHER [19]. A parallel effort has been undertaken by Northrop-Grumman [20], later as part of the DARPA funded HiFIVE and then THZ circuits programs [21]. They first demonstrated a 650 GHz serpentine in 2007 [22], with further increases in operating frequency to 850 GHz [23] and finally to 1.03 THz [24] in 2016.

Also of interest are TWTs that use slow wave structures that have been specifically designed for mm-wave operation. Considerable effort has been put into development of slow wave structures that offer higher beam diameters, coupling impedances or are more suitable for miniaturisation. Specific examples include: overmoded coupled cavities [25], double corrugated waveguides [26], ladder circuits [27], photonic crystals [28] and cascaded serpentines [29]. Wang also provides an excellent summary of all-metal slow wave structures that have been experimentally investigated [30].

In summary, the current highest frequency serpentine (and of any type of TWT) is a micromachined serpentine TWT produced by Northrop Grumman as part of a DARPA funded programme into terahertz circuits which operates at 1.03 THz. We can therefore say that there are two clear lines of enquiry for future mm-wave TWTs; either marginal improvements could be sought for the serpentine structure, or a completely new slow wave structure that attempts to avoid some of the limitations with existing structures.

1.2   Alternative Slow Wave Structures

The previous section summarised early advances in travelling wave tubes based on a spiral wire structure before discussing high frequency serpentine travelling wave tubes in more detail. However, there are many alternative slow wave structures that are suitable for a travelling wave tube, this section introduces the most popular of these.

There are two categories of slow wave structure used for travelling wave tubes: continuous and discrete. A continuous tube is one where the beam and wave interact continuously over the length of the structure, e.g spiral wire or periodically loaded waveguide. Alternatively, a structure can be created where the beam and wave only interact at discrete points e.g serpentine or coupled cavity. Most continuous interaction tubes are formed by using a waveguide which has a suitable phase velocity to allow synchronisation with the beam and an electric field component in the propagation direction. Among periodic structures there can be more variety as the interaction sites can contain either a travelling wave (serpentine) or a standing wave (coupled cavity) and can be coupled using either phase delay (coupled cavity structures use coupling slots with a specific coupling angle) or true time delay (waveguide helix).

A coupled cavity slow wave structure is made from a stack of coupled resonant cavities, each with a hole in the centre allowing the electron beam to pass through and coupling slots between cavities. Compared to a traditional spiral TWT the bandwidth of a coupled cavity TWT is reduced although the output power can be much higher as it can support a higher beam voltage and has significantly better cooling. It has been extensively studied in both academic and industrial circles[31].

Periodic loaded waveguide has been studied for some time, the two main forms that have been applied to travelling wave tubes are disc loaded waveguide and ring plane waveguide. The first treatment of disc loaded waveguide's dispersion relation appears to be by Chu[32]. Today it is commonly used as an accelerator structure and has been studied for use in TWTs[33]. Ring plane waveguide was first proposed by White [34] and consists of a circular waveguide with a pair of ridges running the length of the tube which support a series of annular rings.

Due to the success of the spiral wire TWT there has been extensive study of waveguide based helical structures, of which there are two main types. The first is a circular waveguide with a helical groove cut into the waveguide wall, similar to rifling on a barrel. It was first proposed by Field in 1949[35] and developed further by several authors. Liss et al[36] demonstrated a TWT using a helical groove slow wave structure at 42GHz with an output power of 163W in 1988. Development seems to have stalled after that point probably due to the performance not exceeding that of conventional structures despite much more complicated machining. Although there was a recent paper by Henke in 2016[37]

The other type is simply a rectangular waveguide that has been wrapped into a helix and was first proposed by Waidron[38]. This type of structure offers some advantages as it has true time delay between beam crossings rather than phase delay and allows a larger beam tunnel than other types of SWS. Unfortunately, in addition to the machining complexity, the forward gain of the tube is limited by the need to avoid a large backward wave oscillation as shown by [39].

1.3   TWT system overview

A travelling wave tube is a complicated device containing several interacting systems. Figure 1.5 shows a labelled diagram of a TWT, showing the electron gun, electron beam, collimating magnet, slow wave structure, input and output couplers and collector.
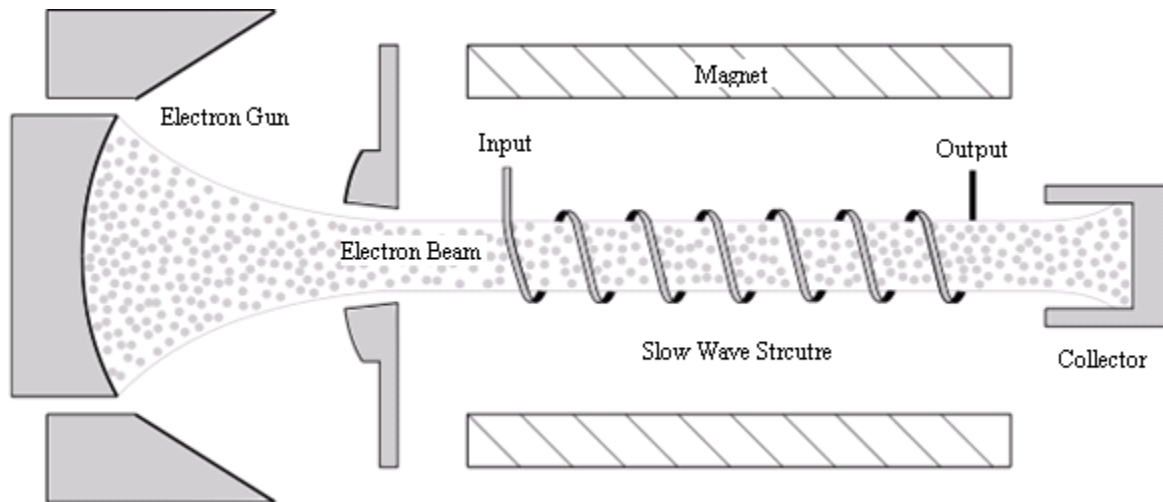
Figure 1.5 – Labelled diagram of a helix TWT.

Considering the figure from left to right, the cathode produces a certain current of electrons, which are then accelerated and focussed by the electron gun. The beam from the electron gun is of a specific current, velocity and diameter, and is collimated by a magnet. The beam then passes through the slow wave structure, where it interacts with the electromagnetic wave applied to the input coupler, and is absorbed by the collector. The combination of electron gun, collimating magnet and collector is often termed a beamstick, and can be operated completely separately from the slow wave structure.

Different designs of electron gun can produce different types of electron beams. Common types include a solid round beam (called a pencil beam) and a thin wide beam (known as a sheet beam). Hollow beams are also possible, and arbitrary shapes can be made from an array of small separate pencil beams. Typically tubes try and use a pencil beam, since the rotational symmetry of the beam greatly simplifies design and operation. However, high performance designs often require more complicated sheet and beamlet-based beams.

Returning to the slow wave structure, within a travelling wave tube the aim of the slow wave structure is to synchronise the phase velocity of the electromagnetic wave with the electron beam. When

synchronised, the beam and wave can interact strongly. With the correct design this interaction will cause energy to be transferred from the beam to the wave, resulting in an amplification of the wave. The theory of the beam-wave interaction is covered in detail in Chapter 2.

Similar to the electron gun there are a variety of slow wave structures. The original and most common type is a helix, which offers a good balance between bandwidth and power handling (typically 10-100 W with 2 octaves of bandwidth [8]). Higher-power operation can be obtained, though lower bandwidth, through the use of a coupled cavity slow wave structure. For mm-wave devices an additional type of slow wave structure becomes important, the serpentine (formed from a folded waveguide). Beyond these, there are a huge variety of addition types of slow wave structures that are used for specialist purposes or of research interest as discussed earlier.

1.4   Summary

The current state of the field has been presented and shows that there is continuing research interest in high frequency travelling wave tubes. From the literature there seem to be two possible approaches to high frequency TWT development, improving the serpentine style device or designing a new slow wave structure, which is more amenable to micromachining and allows a larger beam area.

A system level overview of a TWT has been shown with the two main parts (electron beam and slow wave structure) covered in detail in their respective chapters. The specific operation of the travelling wave interaction and how it relates to the current preferred high frequency slow wave structure (serpentine) will be given in Chapter 2. Chapter 3 covers possible improvements to the serpentine structure and investigates the most promising design in more detail. Chapter 4 explores a new slow wave structure based on a coupled cavity photonic crystal and finally Chapter 5 shows the design work carried out for a possible attempt to fabricate the tube design shown in Chapter 3. Chapter 6 concludes the thesis by presenting an overview and suggestions for further work.

References

[1] Millitech, "Millimetre-wave GaN Power Amplifiers," Available:

 http://www.millitech.com/pdfs/specsheets/IS000100-GaNAMP.pdf

[2] CPI, "mmW Products ,"Available:

http://www.cpii.com/docs/related/40/Family%20of%20MMW%20Products.pdf

[3] M. Thumm, "Progress on gyrotrons for ITER and future thermonuclear fusion reactors," *IEEE Transactions on Plasma Science,* vol. 39, no. 4, pp. 971-979, 2011.

[4] J. H. Booske *et al.*, "Vacuum electronic high power terahertz sources," *IEEE Transactions on Terahertz Science and Technology,* vol. 1, no. 1, pp. 54-75, 2011.

[5] R. Kompfner, *The invention of the traveling-wave tube*. San Francisco, CA: San Francisco Press, 1964

[6] J. Copeland and A. A. Haeff, "The true history of the traveling wave tube," in *IEEE Spectrum*, vol. 52, no. 9, pp. 38-43, Sept. 2015.

[7] J. R. Pierce, *Traveling-wave Tubes*. Van Nostrand, New York, 1950.

[8] A. S. Gilmour, Jr., *Principles of Traveling Wave Tubes*. Boston: Artech House, 1994

[9] C. K. Chong and W. L. Menninger, "Latest advancements in high-power millimeter-wave helix TWTs," *IEEE Transactions on Plasma Science,* vol. 38, no. 6, pp. 1227-1238, 2010.

[10] G. Dohler, D. Gagne, D. Gallagher, and R. Moats, "Serpentine waveguide TWT," in *Electron Devices Meeting, 1987 International*, 1987, pp. 485-488: IEEE.

[11] G. Dohler, D. Gallagher, and J. Richards, "Millimeter wave folded waveguide TWTs," *Vacuum. Electron. Ann. Rev. Proc,* vol. 15, p. 20, 1993.

[12] R. L. Ives, "Microfabrication of high-frequency vacuum electron devices," *IEEE Transactions on Plasma Science,* vol. 32, no. 3, pp. 1277-1291, 2004.

[13] S. Bhattacharjee *et al.*, "Folded waveguide traveling-wave tube sources for terahertz radiation," *IEEE Transactions on Plasma Science,* vol. 32, no. 3, pp. 1002-1014, 2004.

[14] J. Cai, J. Feng, Y. Hu, X. Wu, Y. Du, and J. Liu, "10 GHz bandwidth 100 watt W-band folded waveguide pulsed TWTs," *IEEE Microwave and Wireless Components Letters,* vol. 24, no. 9, pp. 620-621, 2014.

[15] S. Han *et al.*, "Experimental investigation of millimeter wave folded-waveguide TWT," in *Vacuum Electronics, 2003 4th IEEE International Conference on*, 2003, pp. 322-323: IEEE.

[16] A. J. Theiss, C. J. Meadows, R. Freeman, R. B. True, J. M. Martin, and K. L. Montgomery, "High-average-power W-band TWT development," *IEEE Transactions on Plasma Science,* vol. 38, no. 6, pp. 1239-1243, 2010.

[17] C. D. Joye *et al.*, "Demonstration of a high power, wideband 220-GHz traveling wave amplifier fabricated by UV-LIGA," *IEEE Transactions on Electron Devices,* vol. 61, no. 6, pp. 1672-1678, 2014.

[18] R. Kowalczyk *et al.*, "A 100 watt W-band MPM TWT," in *Vacuum Electronics Conference (IVEC), 2013 IEEE 14th International*, 2013, pp. 1-2: IEEE.

[19] C. Paoloni *et al.*, "Design and fabrication of a 1 THz backward wave amplifier," *Terahertz Science and Technology,* vol. 4, pp. 149-163, 2011.

[20] D. Gallagher, J. Richards, and C. Armstrong, "Millimeter-wave folded waveguide TWT development at Northrop Grumman," in *Plasma Science, 1997. IEEE Conference Record-Abstracts., 1997 IEEE International Conference on*, 1997, p. 161: IEEE.

[21] J. Tucek, M. Basten, D. Gallagher, and K. Kreischer, "1.2: Sub-millimeter and THz power amplifier development at Northrop Grumman," in *Vacuum Electronics Conference (IVEC), 2010 IEEE International*, 2010, pp. 19-20: IEEE.

[22] J. Tucek, K. Kreischer, D. Gallagher, R. Vogel, and R. Mihailovich, "Development and operation of a 650 GHz folded waveguide source," in *Vacuum Electronics Conference, 2007. IVEC'07. IEEE International*, 2007, pp. 1-2: IEEE.

[23] J. Tucek, M. Basten, D. Gallagher, and K. Kreischer, "Testing of a 0.850 THz vacuum electronic power amplifier," in *Vacuum Electronics Conference (IVEC), 2013 IEEE 14th International*, 2013, pp. 1-2: IEEE.

[24] J. C. Tucek, M. A. Basten, D. A. Gallagher, and K. E. Kreischer, "Operation of a compact 1.03 THz power amplifier," in *Vacuum Electronics Conference (IVEC), 2016 IEEE International*, 2016, pp. 1-2: IEEE.

[25] E. J. Kowalski, M. A. Shapiro, and R. J. Temkin, "An overmoded W-band coupled-cavity TWT," *IEEE Transactions on Electron Devices,* vol. 62, no. 5, pp. 1609-1616, 2015.

[26] M. Mineo and C. Paoloni, "Double-corrugated rectangular waveguide slow-wave structure for terahertz vacuum devices," *IEEE Transactions on Electron Devices,* vol. 57, no. 11, pp. 3169-3175, 2010.

[27] C. L. Kory, M. E. Read, R. L. Ives, J. H. Booske, and P. Borchard, "Design of overmoded interaction circuit for 1-kW 95-GHz TWT," *IEEE Transactions on Electron Devices,* vol. 56, no. 5, pp. 713-720, 2009.

[28] E. I. Smirnova, B. E. Carlsten, and L. M. Earley, "Design, fabrication, and low-power tests of a W-band omniguide traveling-wave tube structure," *IEEE Transactions on Plasma Science,* vol. 36, no. 3, pp. 763-767, 2008.

[29] K. Nguyen *et al.*, "1.4: Design of a high-gain wideband high-power 220-GHz multiple-beam serpentine TWT," in *Vacuum Electronics Conference (IVEC), 2010 IEEE International*, 2010, pp. 23-24: IEEE.

[30] W. Wang, Y. Wei, G. Yu, Y. Gong, M. Huang, and G. Zhao, "Review of the novel slow-wave structures for high-power traveling-wave tube," *International Journal of Infrared and Millimeter Waves,* vol. 24, no. 9, pp. 1469-1484, 2003.

[31] R. Luis, *A comprehensive review of travelling wave tube technology*, Defence Research Establishment Ottawa, Nov. 1979.

[32] E. L. Chu and W. W. Hansen "The Theory of Disk-Loaded Wave Guides" *Journal of Applied Physics*, vol. 18, no.11, pp. 996-1008, November 1947

[33] R.J. Barker and E. Schamiloglu, Eds., *High Power Microwave Sources and Technologies*, New York, IEEE Press/J. Wiley & Sons, 2001.

[34] R. M. White, C. E. Enderby and C. K. Birdsall, "Properties of ring-plane slow-wave circuits," *IEEE Transactions on Electron Devices*, vol. 11, no. 6, pp. 247-261, June 1964.

[35] L. M. Field, "Some Slow-Wave Structures for Traveling-Wave Tubes," in *Proceedings of the IRE*, vol. 37, no. 1, pp. 34-40, January 1949

[36] C. Liss, R. Harper and M. P. Puri, "Helical waveguide millimeter wave TWT," *Technical Digest., International Electron Devices Meeting*, San Francisco, CA, USA, 1988, pp. 374-377.

[37] H. Henke, "Small Signal Treatment of a 94-GHz Helical Waveguide TWT," *IEEE Transactions on Electron Devices*, vol. 63, no. 3, pp. 1322-1325, March 2016

[38] R. A. Waidron, "Theory of the helical waveguide of rectangular cross-section," *Journal of the British Institution of Radio Engineers*, vol. 17, no. 10, pp. 577-592, October 1957.

[39] S. Ahn and A. K. Ganguly, "Analysis of helical waveguide," *IEEE Transactions on Electron Devices*, vol. 33, no. 9, pp. 1348-1355, September 1986.

2 Slow Wave Structure Design

The aim of this chapter is to discuss the theory of the travelling wave interaction and to develop a set of techniques to both design and verify slow wave structures. The theory of operation for travelling wave tubes is first introduced and discussed, and then an overview of the techniques used for simulation is presented. Next the current preferred high frequency slow wave structure, the serpentine, is analysed in detail using both theory and simulation. Finally the analytical and computational techniques are combined and applied to design a realistic serpentine travelling wave tube.

2.1 Travelling Wave Interaction

2.1.1 Overview

The interaction between an electron beam and a travelling wave of a similar velocity has been analysed in a variety of ways, with the most popular being the small signal circuit approach taken by J.R Pierce in his seminal work 'Travelling-wave tubes' [1] (also serialised in the Bell System Technical Journal). As this is a 246 page book, only an overview is presented here, which also borrows material from later interpretations of Pierce's work by Sims and Stephenson [2] and Gilmour [3]. Large signal analysis has been carried out by several authors including [4], although it is not considered here.

The fundamental travelling wave interaction can be described as follows. An electromagnetic wave is travelling in the same direction as an electron beam but slightly slower. The field from the electromagnetic wave exerts a force on the electrons within the beam, causing some electrons to accelerate and some to decelerate. As a result, bunches form because the bunches consist of charged particles (electrons), an electric field is generated between the regions of high and low electron density. This electric field is shifted in phase by 90° from the initial waveform, which causes the total electric field of the travelling wave (i.e. the sum of the electric field from the space charge wave and the original wave) to slowly shift in phase. As it does so, the bunches eventually overtake the travelling wave, causing the travelling wave to decelerate the bunches and thus extract energy from the beam. The result is a rapid increase the power in the travelling wave within the slow wave structure [3].

2.1.2 Pierce theory

The basis of the Pierce's theory [1] (although the version presented here uses the symbols from [2] and graphs from [3]) is to consider a travelling wave tube as a transmission line, made of lumped elements, with an additional current added to each inductor to represent the electron beam. Figure 2.1 shows three periods of such a transmission line with the per-unit-length inductance L_u, capacitance C_u and beam current i_z labelled.
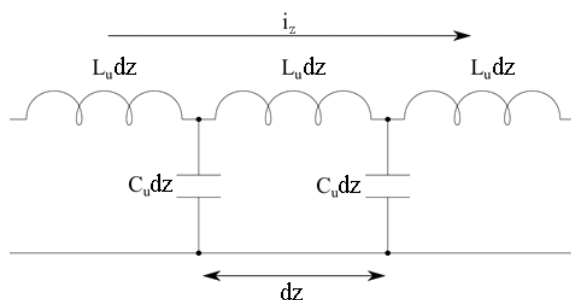
Figure 2.1 – Three periods of a transmission line with an induced current representing the beam-wave interaction.

In the absence of the beam ($i_z = 0$), Figure 2.1 represents a simple passive LC transmission line, therefore the per unit length quantities can be eliminated by considering the circuit in terms of its propagation constant (β_c) and impedance (κ). Accordingly:

$$\beta_c^2 = \omega^2 L_u C_u \tag{2.1}$$

$$\kappa = \sqrt{\frac{L_u}{C_u}} \tag{2.2}$$

It can then be shown (see [1]) that the voltage (V_z) on the circuit that is acting on the electron beam can be written in terms of the circuit parameters as:

$$V_z = \frac{-\Gamma^2 \Gamma_c \kappa}{\Gamma^2 - \Gamma_c^2} i_z \tag{2.3}$$

Where $\Gamma = \alpha + j\beta$ is the complex propagation constant of the wave travelling along both the slow wave structure and electron beam and Γ_C is the propagation constant of the circuit. In addition, from an analysis of the effect of space charge on electron bunching, the current induced on the beam by the circuit voltage V_z can be found as [1]:

$$i_z = \frac{j\beta_e I_0 \Gamma}{2V_0(j\beta_e - \Gamma)^2} V_z \qquad (2.4)$$

Where β_e is the propagation constant of the electron beam. Equations 2.3 and 2.4 can be combined to give a single equation for β:

$$\frac{j\beta_e}{(j\beta_e - \Gamma)^2} \frac{\Gamma^2 \Gamma_c}{\Gamma_c^2 - \Gamma^2} 2C^3 + 1 = 0 \qquad (2.5)$$

Where:

$$C^3 = \frac{\kappa}{4V_0/I_0} \qquad (2.6)$$

C is defined by Pierce as the gain parameter. The impedance of the circuit, κ, is usually called the interaction impedance (κ is used here although some authors use Z_0 or K). It should be noted that there are three propagating waves here, a circuit wave (Γ_c), the electron beam(β_e) and a wave that is defined over both the circuit and the beam (Γ).

Since Equation (2.5) is a fourth order equation, there are four solutions to Γ with each representing a different propagating mode in the combined beam and circuit.

2.1.2.1 Synchronous operation

In order to remain consistent with Pierce's original work this section uses the physics wave descriptions, rather than the more sensible engineering ones, such that $\Gamma = \alpha + j\beta$ and that -z is considered the forward direction of the wave.

The simplest solution to (2.5) is the case where the electron beam has the same propagation constant as the circuit, so that $\Gamma_c = j\beta_e$ (which Pierce refers to as the synchronous case). From Pierce[1]:

$$\Gamma_1 = j\beta_e \left(1 + \frac{C}{2}\right) - \frac{\sqrt{3}}{2}\beta_e C \qquad (2.7)$$

$$\Gamma_2 = j\beta_e \left(1 + \frac{C}{2}\right) + \frac{\sqrt{3}}{2}\beta_e C \qquad (2.8)$$

$$\Gamma_3 = j\beta_e(1 - C) \qquad (2.9)$$

$$\Gamma_4 = -j\beta_e \left(1 - \frac{C^3}{4}\right) \qquad (2.10)$$

The first three solutions all contain the propagation constant of the beam, β_e and a small additional term. This implies that each wave is travelling in the same direction as the electron beam, and consequently is a forward wave. The fourth solution is dominated by $-\beta_e$, indicating that it is travelling in the opposite direction to the electron beam and is a backward wave. In Γ_1 and Γ_2 there is a term containing $+\frac{\beta_e C}{2}$, which implies that the wave travels at a lower velocity than the electron beam. However, in Γ_3 the term $-\beta_e C$ is present, showing that the wave travels faster than the electron beam. Finally the imaginary term in Γ_1 is positive, thus a growing wave, and negative in Γ_2 indicating a decaying wave. Figure 2.2 shows sketches of the variation of amplitude with distance for these four waves.
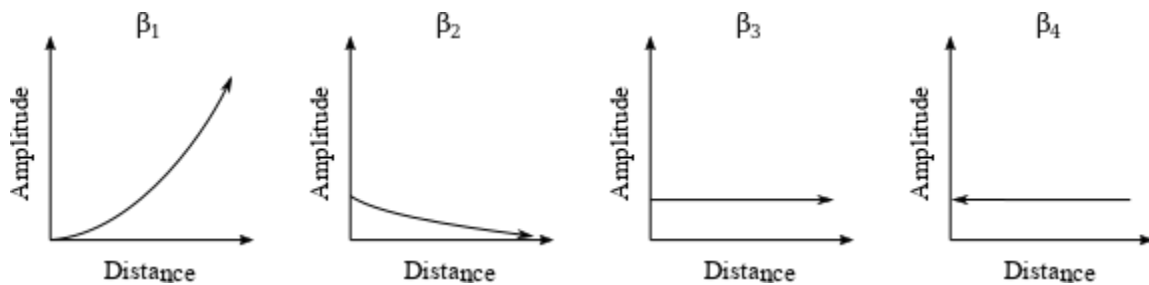
As shown from the analysis of the wave equation for the beam/circuit interaction, any power applied to the beam will be split between the different propagating waves, one of which will increase over the length of the tube. Therefore the gain of the tube, assuming that the growing wave is significantly larger than the others at the end (usually the tube is designed with either a sever or additional loss to remove the other three waves) can be represented by a fixed loss term and a gain term proportional to the length of the tube (assuming small signal operation) which is given by Pierce as:

$$G = A + BCN \tag{2.11}$$

Here A is the loss caused by the incident power being split between three travelling waves, and can be simply expressed in dB as:

$$A = 10 \log_{10} \left(\frac{1}{3}\right)^2 = -9.54 dB \tag{2.12}$$

The gain term, which is the propagation constant calculated from the beam/wave equation multiplied by the length of the structure, has been split into three parts for easier understanding. B represents the synchronisation between the beam and the undisturbed circuit wave, for the synchronous case.

$$B = 10 \log_{10} \left(e^{\sqrt{3}\pi}\right)^2 = 47.3 dB \tag{2.13}$$

The next term, C, is the gain parameter defined earlier and N is the length of the structure given in integer periods. Accordingly, the small signal gain equation when the electron beam and undisturbed circuit wave are propagating at the same phase velocity is:

$$G = -9.54 + 47.3CN \tag{2.14}$$

This result is well known to be surprisingly accurate providing $CN > 0.2$ and the tube is not driven into saturation.

2.1.2.2 Non-synchronous operation

Unfortunately, when the electron beam has a different phase velocity to the undisturbed circuit, Equation 2.5 can only be solved numerically. Therefore Pierce introduces a parameter, *b*, which represents the normalised difference between the phase velocity of the circuit and the beam, and is given as:

$$b = \frac{u_0 - v_p}{C v_p} \tag{2.15}$$

Where v_p is the phase velocity of the circuit, namely:

$$v_p = \sqrt{\frac{1}{L_u C_u}} \tag{2.16}$$

Note that (2.15) can be rewritten to define the electron beam velocity u_0 in terms of b, v_p and C, as:

$$u_0 = (1 + Cb)v_p \tag{2.17}$$

Pierce then solves the characteristic equation (2.5), assuming that:

$$\Gamma_c = j\beta_e + j\beta_e Cb \tag{2.18}$$

When $b = 0$ the above clearly collapses to the synchronous case. Conversely, if $b < 0$ the electrons are slower than the undisturbed circuit wave and vice versa when > 0. Figure 2.3 shows a plot (of the propagation constant, given in real and imaginary components x_i and y_i against b for the case where there is neither loss nor space charge.
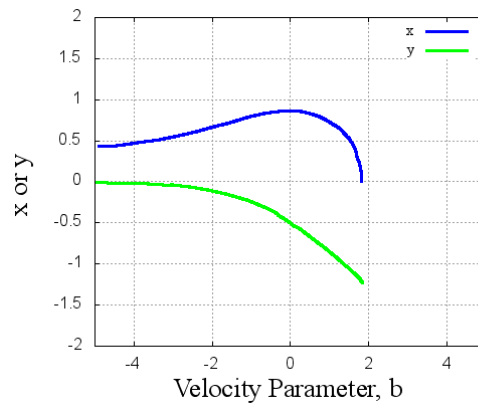
Figure 2.3 – Real and imaginary parts of B for non-synchronous operation (i.e $b \neq 0$). Adapted from Gilmour [3], who in turn adapted it from Pierce [1].

In addition, the gain equation for the general case can be rewritten in the form:

$$B = \log_{10}(e^{2\pi x_i})^2 \qquad\qquad (2.19)$$

Therefore x_i has a large effect on the gain of the circuit. From Figure 2.3, the wave is always growing, with the maximum gain at $b = 0$ (beam and undisturbed circuit wave of equal velocity). Since y_i is always negative, the growing wave is travelling slower than the electron beam, even when the circuit wave is faster than the electron beam.

Finally Pierce observed that for tubes with large gains (i.e operating away from the corner caused by the A term) that changes in b beyond ± 1 have a substantial effect on the gain. Therefore, considering Equation 2.17, the allowable difference between the electron beam and undisturbed circuit velocity for normal operation is of the order of C, as will be shown in more detail later in the design example.

2.1.2.3 Effect of Loss

Pierce approaches the effect of loss within the circuit in the same way by introducing an additional parameter d and then solving the characteristic equation assuming:

$$\Gamma_c = j\beta_e + j\beta_e Cb + \beta_e Cd \qquad\qquad (2.20)$$

Figure 2.4 shows the effect of increasing values of d on B. As expected, increasing amounts of loss result in lower gain. However, interestingly, the optimal value of b stays close to zero. Therefore, provided the loss per unit length is small, the tube can be designed assuming lossless elements with the attenuation being considered towards the end of the design process.
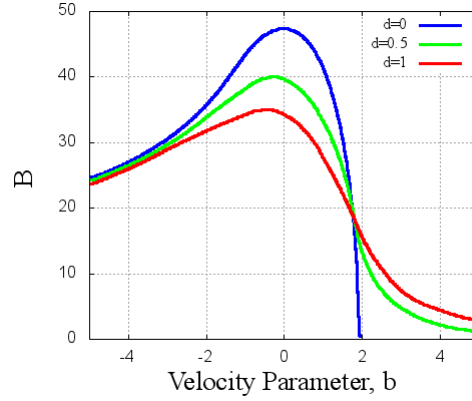
Figure 2.4 – Graph of B (gain parameter) against the velocity parameter b for increasing values of d. Adapted from Gilmour [3], who in turn adapted it from Pierce [1].

2.1.2.4 Effect of Space Charge

The effect of space charge on the four travelling waves on the beam can be considered by adding a space charge term into the electric field in Equation 2.4 and solving the wave equation once again. When this is done, an additional term that represents the effect of space charge appears, which is defined as follows:

$$4QC = \left(\frac{\beta_q}{C\beta_e}\right)^2 \tag{2.21}$$

Pierce defines Q as the space charge parameter, although its meaning is not immediately clear. However, remembering that $\omega_e \equiv \omega$, we can write:

$$\frac{\beta_q}{\beta_e} = \frac{\omega_q}{\omega} \tag{2.22}$$

Therefore:

$$4QC = \frac{(\omega_q/\omega)^2}{C^2} \tag{2.23}$$

The above equation is most easily understood as the ratio of the debunching forces, represented by the ω_q/ω term (the ratio of the plasma frequency of the beam to the frequency of the wave) to the C^3 term (which represents the strength of the interaction between the electron beam and the slow wave). Therefore Equation 2.23 can be thought of as the ratio of the strength of the debunching forces to the bunching forces and is a good measure of the scale of space charge effects within a travelling wave tube.

Figure 2.5 shows the variation of the propagation constant with *b* for different values of QC. From the figure it is clear that as the space charge density increases the maximum gain decreases, and the electron beam velocity must be increased to keep the tube operating at the point of maximum gain.
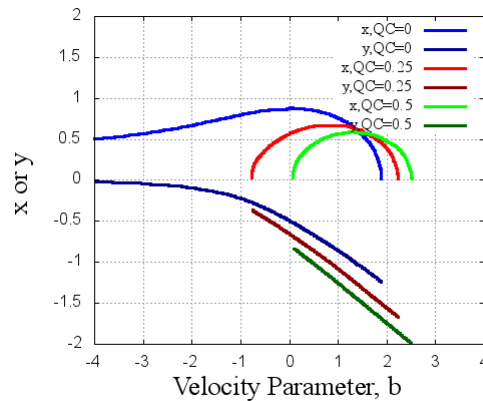
Figure 2.5 - Real and imaginary parts of B for increasing values of QC. Adapted from Gilmour [3], who in turn adapted it from Pierce [1].

2.1.3   Interim Conclusions

Several conclusions can be drawn from Pierce's theory for designing travelling wave tubes. The first is that there is no fundamental physical limit to high frequency operation – whether a tube has net gain simply depends on whether the gain in the propagation constant of the beam wave interaction is sufficiently larger than the loss within the slow wave structure.

Also important is that the travelling wave interaction slows the electron beam (since the beam must lose kinetic energy as energy is transferred to the travelling wave). Consequently, there is a maximum number of periods that can be chained before the gain saturates, as the electron bunches have 'rolled over' and are now removing energy from the wave. One way to increase the gain from a tube is to match the decrease in electron gun velocity to the period length of the slow wave structure. This principle is known as velocity tapering and has been studied extensively [5][6].

Next, the gain is dominated by the interaction impedance, which is determined by the physical geometry of the slow wave structure and is heavily linked to the strength of the electric field seen by the electron beam. One way to improve on the current structure used for high frequency operation would be to increase its interaction impedance, if this can be done without affecting manufacturability

44

The gain is also linked to the beam current, with higher currents giving higher gains. However the maximum current density is limited by both the maximum collimating magnetic field and by the reduction in gain caused by increasing space charge density. A structure that allows a larger beam tunnel, without compromising the interaction impedance, will therefore allow higher gain and higher frequency operation.

As shown by the analysis, whilst the optimal beam velocity will be lower than the synchronous case it is close enough that the initial design can assume synchronous operation. Furthermore, as the circuit parameters define the optimal beam velocity we can say that there will be an optimal beam velocity given an arbitrary set of circuit parameters.

Finally, whilst the space charge density and thus the beam current has an optimal value (increasing the beam current increases the interaction impedance but also reduces x_1 through space charge effects) it is independent of the other slow wave structure parameters.

The initial analytical design can therefore assume no space charge and synchronous operation, but these factors can then be taken into account and adjusted for in more detailed simulation. Due to experimental limitations, only tubes with low space charge density will be considered here. In this case there is little possibility of exceeding the point where increasing the beam current results in lower gain, and saturation effects beyond the maximum length of the tube do not need to be considered here.

2.2   Serpentine Slow Wave Structures

The general Pierce theory can now be used to calculate the parameters for a serpentine slow wave structure and its accompanying electron beam. Several authors [7][9][10] have studied this topic and the work presented below is a synthesis of their results.

Figure 2.6 shows the geometry of one period of a serpentine slow wave structure. Here the electron beam follows the straight path and the EM wave the serpentine path, and the waveguide path length (L), height (b), length (s), beam tunnel diameter (d_b) and period length (p) have been labelled. The waveguide width (a) is not shown on the diagram as it is normal to the page. The operating frequency range of the structure is restricted such that only a TE10 mode is excited within the waveguide. As discussed earlier, the two main terms that describe the operation of a TWT that are specific to the slow wave structure are the phase velocity along the beam tunnel and the interaction impedance.
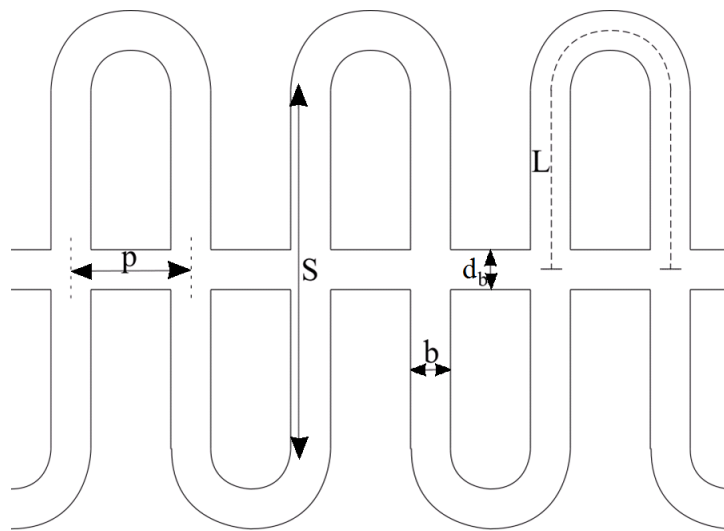
Figure 2.6 – Labelled diagram of three sections of a serpentine slow wave structure.

2.2.1 Spatial Harmonics

A serpentine slow wave structure only has discrete points where the beam and wave can interact. Therefore, from the perspective of the beam there are an infinite set of spatial harmonics that exist along the beam tunnel. An intuitive explanation for spatial harmonics is as follows. Each beam/wave crossing can be represented by a phasor that is offset from its neighbours by the coupling angle. Accordingly, the phase velocity can be calculated knowing the distance between beam crossings and the time it takes between a point of constant phase appearing on one phasor to the next. Figure 2.7 shows three phasors separated by a distance d with a coupling angle of θ. The wave travels right to left and the time evolution of the phasors is along the y axis.
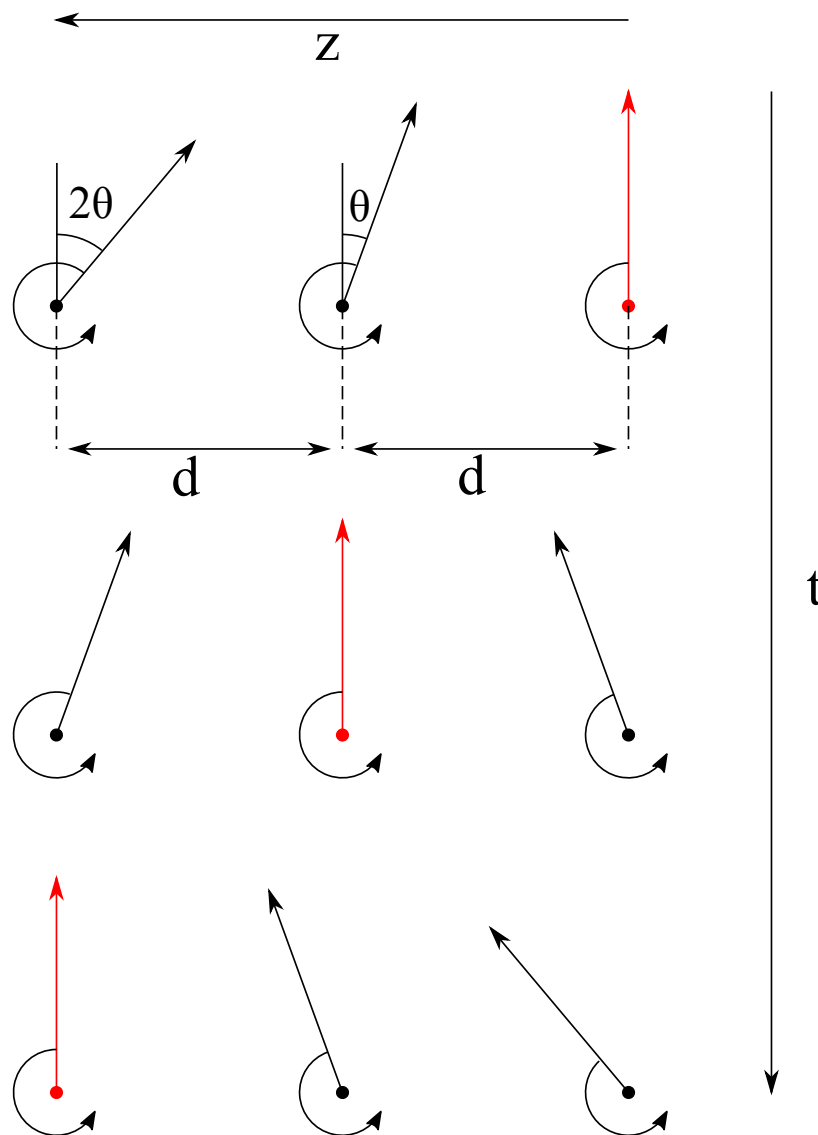
Figure 2.7 – Phasors at discrete points of time and space.

47

After a sufficient delay the point of constant phase will also appear on the previous phasor, representing a backward wave. Slower spatial harmonics (forward and backward waves) are also possible as the point of constant phase can clearly 'skip' rotations of the phasors, representing an additional $2\pi n$ term.

A final important effect of spatial harmonics is that whether the fundamental is a forward or backward wave is set by the coupling angle which determines whether the point of constant phase first appears on the forward or backward phasor.

2.2.2 Phase velocity

Assuming the structure is smooth walled with no significant discontinuities then the phase shift between beam crossings (ϕ_T) is given by [7]:

$$\phi_T = \beta_w . L + \pi + 2\pi n \tag{2.24}$$

Where β_w is the propagation constant along the waveguide (not the beam tunnel). The first term is simply the propagation constant of the waveguide multiplied by the path length, the π term is because of the phase inversion caused by the 180° waveguide bend and the final $2\pi n$ term is due to the periodic nature of the structure (and is what gives rise to the spatial harmonics). As the propagation constant of the TE10 box waveguide mode is given by [8]:

$$\beta_w = \sqrt{\left(\frac{\omega^2}{c^2} - \frac{\pi^2}{a^2}\right)} \tag{2.25}$$

And the phase velocity along the beam tunnel is given by:

$$v_T = \frac{\omega p}{\phi_T} \tag{2.26}$$

Equations (2.24), (2.25) and (2.26) can be combined to give:

$$v_T = \frac{\omega p}{L\sqrt{\left(\frac{\omega^2}{c^2} - \frac{\pi^2}{a^2}\right)} + \pi + 2\pi n} \tag{2.27}$$

By inspection, Equation 2.27 shows that the phase velocity is defined by L, a and p, which are all independent of each other. As Maxwell's equations are length-invariant for passive structures containing only linear dielectrics and metal, the lengths L and p could be given in terms of a (i.e. $L_a . a$ and $p_a . a$) such that the shape of the phase velocity curve would remain constant as a is scaled. However, this needlessly complicates the equations, so it is normally left out (although it is a useful property that allows the dimensions of a working tube to be scaled to a new design frequency). Therefore, the independent parameters of interest to the designer are L and p although, as the bend radius is determined by p, L can be broken down into a straight section (s), which is fully independent, and an 180° bend which can be given in terms of p as:

$$L = s + \frac{\pi p}{2} \tag{2.28}$$

There are clearly limits on the ranges of p and s so that the geometry is realisable and the initial assumptions hold. Firstly, p has a lower bound of $2b + k_{wall}$, where b is the height of the waveguide and k_{wall} is the minimum machinable wall thickness. In addition, as b increases the radius of the waveguide bend must decrease, which will increase its reflection coefficient. Beyond a certain point, the reflection from the bend will introduce a stopband, which will prevent the slow wave structure from operating correctly. However, it should be noted that the reflection can be reduced by adjusting the height of the waveguide through the bend [9]. Whilst there is no physical upper limit, increasing p beyond the minimum length possible is of no benefit for normal operation – it simply makes the structure larger and reduces the slow wave factor, necessitating a faster beam or operation on a higher order space harmonic.

The lower bound for L is recommended to be slightly larger than the beam tunnel diameter so that the beam tunnel is separate from the 180° bend. Additional length beyond 2π does not have any effect on the phase shift between cavities due to the $2\pi n$ term in Equation 2.27 any only further increases transmission losses.

2.2.3   Interaction Impedance

For the specific case of a beam travelling through a gap, the coupling impedance is given by [10]:

$$\kappa = Z_w \left(\frac{2\sin\left(\frac{\beta_T b}{2}\right)}{\beta_T^2 pb} \right)^2 \tag{2.29}$$

Where Z_w is the impedance of the waveguide and β_T is the propagation constant of the circuit with respect to the beam tunnel (analogous to the β_c term used by Pierce but renamed here to avoid confusion with the use of c subscript within usual waveguide equations that involve free space).

As the impedance of the waveguide is given as [8]:

$$Z_w = 377 \frac{2b}{a} \sqrt{1 - \frac{\lambda^2}{\lambda_c^2}} \tag{2.30}$$

Substituting Equation 2.30 into 2.29 and then collating constants gives:

$$\kappa = kb \left(\frac{2\sin\left(\frac{\beta_T b}{2}\right)}{\beta_T b} \right)^2 \tag{2.31}$$

Which has a maximum at:

$$\beta_T b = 2.3311 \tag{2.32}$$

Therefore, the optimum waveguide height, b, is determined by the propagation constant of the slow wave structure along the beam tunnel.

2.2.4   Beam Tunnel

The beam tunnel does not have an easily calculable optimal diameter like the waveguide height, because it is affected by multiple factors [11]. As the beam tunnel increases in diameter beyond the waveguide height it causes an increasingly significant reflection, which, as with any periodic reflection, causes pass and stop bands. A stop band at the intersection of the dispersion curves for m = 0 and m = 1 is desirable as it allows the beam line to pass through without generating a significant oscillation [9]. However, more severe discontinuities may cause instability or prevent normal operation of the slow wave structure [12].

In addition, the electric field within the beam tunnel becomes concentrated around the edge of the tunnel. Unfortunately, the electron beam cannot fill the entire beam tunnel - imperfections in alignment, magnetic field uniformity and scalloping of the beam require the beam diameter to be smaller (typically 50-80% [13]) than the tunnel to prevent the electron beam from colliding with the slow wave structure. The combination of these two effects causes the interaction impedance to be lower than expected for large beam tunnels.

For example, Figure 2.8 and Figure 2.9 show two different plots of the spatial variation of mod(E) calculated using the commercial multiphysics finite element software CST Microwave Studio, demonstrating that the electric field concentrates around the edge of the beam tunnel as its diameter increases. Here it has been assumed that a = 18 mm and b = 1.9 mm. The figures show a cross section of half a period of the slow wave structure, with the beam tunnel passing from top to bottom and the waveguide passing into the page.

Another disadvantage of a larger beam tunnel is that the electric field penetrates further into the beam tunnel, requiring the length of tunnel between sections to be increased (thus increasing the period) to prevent undesirable coupling of the electric field along the beam tunnel. If the period is not increased then significant coupling can occur, as shown by the strength of the field at the boundary in Figure 2.9.
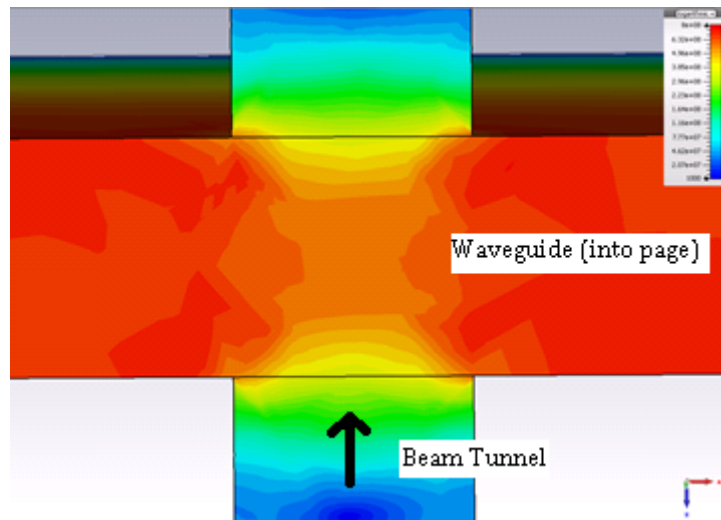
Figure 2.8 – Electric field magnitude inside a beam tunnel with a diameter equal to the waveguide height.
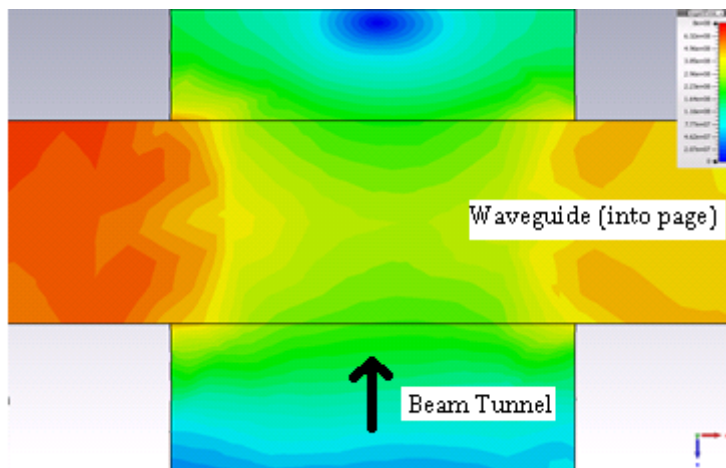
Figure 2.9 - Electric field magnitude inside a beam tunnel with a diameter twice the waveguide height.

In general, the smallest possible beam tunnel that can accommodate the design beam current is recommended, taking into account the fill factor required to avoid significant collision between the beam and the structure. However, for high frequency designs the beam current is often a limiting factor (as increasing the current is the easiest way to increase the gain). If the beam current is limited by the beam current density that the focussing magnet can keep collimated then increasing the size of the beam tunnel allows an increased beam current and correspondingly higher gain.

The usual design process is to simulate the structure (simulation techniques are discussed later) with a beam tunnel of equal diameter to the waveguide height and then to simultaneously increase the beam

tunnel diameter and the beam current (maintaining a constant beam current density) to find the tunnel diameter that gives maximum gain.

2.2.5   Initial conclusions

In summary, there are only three independent parameters that are under the control of the designer, although it is worth noting that the other dependent parameters have certain constraints, which are then imposed on the independent parameters. These are:

s, the straight length - cannot be smaller than the beam tunnel diameter and should not be so large as to introduce a phase shift of more than π between periods.

p, the period length - cannot be so small that the optimum waveguide height, b, is constrained by the minimum machinable wall thickness.

v_{beam}, the electron beam velocity - the only constraint is that the beam must be non-relativistic.

Considering just these three parameters, there will clearly be certain combinations that are optimum for different design goals. For high frequency operation the main design aim is to maximise gain per unit length over a specified bandwidth.

The bandwidth of the device can be determined from the dispersion diagram [14]. Figure 2.10 shows the frequency plotted against the propagation constant for a serpentine structure with a typical set of parameters (from a later design example) with the beam line and n = 1 and n = 0 harmonics plotted. The diagram shows that each harmonic has forward and backward waves, which intersect with each other and with the beam line. The operating bandwidth is limited to the region where the electron beam velocity is similar to the phase velocity along the beam tunnel (i.e the point of intersection between the curves). As the difference between the two lines increases, the gain reduces until it falls to zero.
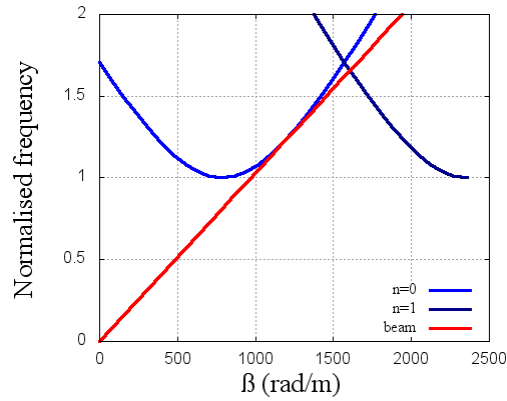
Figure 2.10 – Dispersion diagram of a serpentine slow wave structure (zeroth and first spatial harmonics plotted) and an electron beam.

Figure 2.11 shows an alternative way of presenting the same data, which is to plot the phase velocity against frequency. The advantage of the dispersion diagram is that it clearly shows the additional spatial harmonics, which are a major source of instability. The advantages of the phase velocity plot are that it is easy to tune the beam velocity and to add the group velocity to the plot. Both approaches are found in the literature and the choice appears to be due to the author's personal preferences.
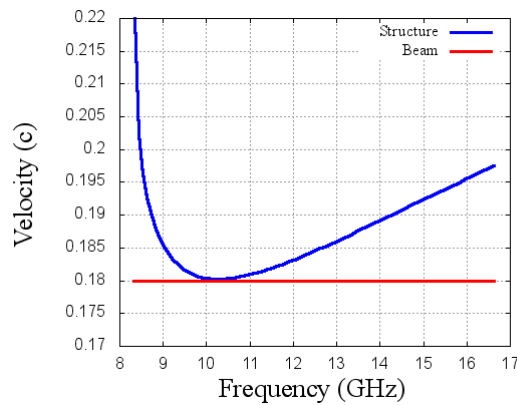
Figure 2.11 – Plot of the phase velocity of a slow wave structure and an electron beam.

The gain is inversely proportional to the difference between the two curves, and the maximum gain (determined by other factors such as the beam current and interaction impedance) is reached when the phase velocity of the slow wave structure is very slightly larger than that of the electron beam.

A more sharply-varying dispersion curve will have lower bandwidth but a higher gain, while a shallower curve will have more bandwidth but less gain. Figure 2.12 to Figure 2.14 show a set of phase velocity

curves with different parameter sets showing how *s* and *p* affect the shape of the curve and the size of the operating region. As shown by Figure 2.12, *p* has a strong effect on the required electron beam velocity but does not significantly change the shape of the phase velocity curve. Figure 2.13 shows that s has a noticeable effect on the shape and minimum value of the phase velocity curve. The decrease in the required electron beam velocity caused by increasing *s* can be compensated for by increasing *p*, as shown in Figure 2.14, which causes the frequency of the operating point to increase and the curve to flatten.
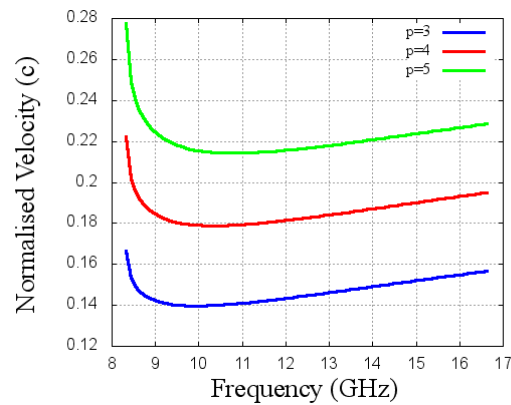
Figure 2.12 – The effect of sweeping p between 3 mm and 5 mm (assuming s = 7 mm, a = 18 mm).
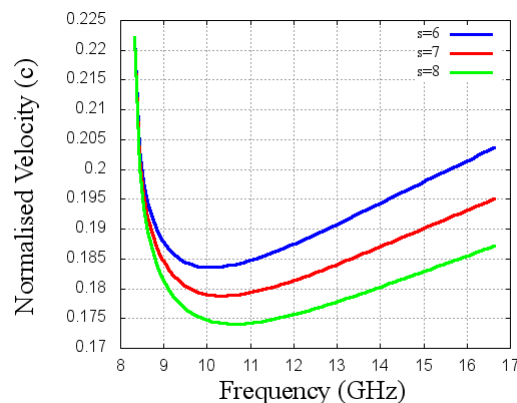
Figure 2.13 – The effect of sweeping s from 6 mm to 8 mm (assuming p = 4 mm, a = 18 mm).
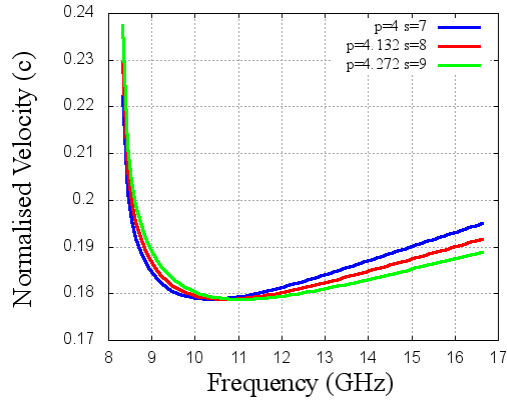
Figure 2.14 – Effect of increasing s and simultaneously tuning p to keep the required beam velocity constant (assuming a = 18 mm).

As explained earlier there is a point of maximum gain, which is usually referred to as the operating point, and generally given in terms of the cutoff frequency of the waveguide, e.g. as $f_{max} = 1.5f_c$. The choice of the operating point has a significant effect on both the gain and the bandwidth. The gain is linked to the interaction impedance which, in a serpentine slow wave structure, sharply decreases as the operating frequency is increased from the cut off frequency [11] (it is related to the waveguide impedance, which is strongly dependant on frequency) but the bandwidth is determined by the dispersion which also decreases with frequency (as the structure is a phase delay based structure). Therefore, the choice of operating point must maintain a balance between these two factors, a low operating frequency (relative to the cutoff frequency of the waveguide) gives higher gain but a lower bandwidth and a high operating frequency the reverse. Typical values found in the literature for the operating point are around $f_{max} = 1.25f_c$ [14][10].

From the Pierce theory introduced earlier, we know that the gain of a travelling wave tube is given by (2.14). Consequently, for an electron beam of a fixed power, a low voltage/high current electron beam is desirable for high gain operation. However as shown above, the beam velocity limits the range of values possible for *p*. As *p* is linked to the interaction impedance, it can be shown that beyond a certain limit, the reduction in gain due to a decrease in interaction impedance is larger than the increase in gain from the increase in beam current. It is also worth noting that there is a limit to the maximum beam current density so a design that maximises *b* (and thus d_b) is again desirable for high gain operation.

56

Given that the optimum value for b is fixed by the ratio $\beta_T b = 2.3311$ then an increase in the propagation constant along the beam tunnel (i.e. a reduction in the electron beam velocity) will decrease the optimum size of b, limiting the maximum beam current and simultaneously lowering the interaction impedance due to the due to the $\frac{1}{\beta_T p}$ term in (2.29). In the literature, electron beam velocities are typically around 0.3c [7][9][10] for serpentine structures with operation as low as around 0.2c reported [15].

2.3   Design Example

In this section, a design example is presented where the techniques introduced above are combined to design a serpentine slow wave structure for a travelling wave tube. The specification for the structure is quite general; the only goal is to produce a design that could realistically be manufactured in house, – which translates to a beam voltage of below 10 kV, a minimum slot size of 2 mm and an aspect ratio below 10:1. A high bandwidth design is desirable, as it should loosen machining tolerances. High gain is again desirable as it should help to compensate for the additional loss from using sub-optimal parts and materials, although extremely high gains should be avoided due to the risk of instability. Accordingly, the first step is to use analysis to calculate an initial set of parameters before initial tuning/verification in the eigenmode solver and finally verification of the design in the Particle in Cell solver (PIC) solver.

2.3.1   Simulation overview

The recommended method of simulating a travelling wave tube is with a PIC solver [16]. A PIC solver works by meshing the structure into small cells, as with most EM simulation tools, then the solver calculates the effect of the field on the particles and then vice versa within each cell. Provided the timestep is small enough in relation to the mesh size the simulation is stable [17]. It should be noted that if a PIC solver is run without any charged particles it is broadly similar to a normal transient microwave solver. Unfortunately simulating an entire travelling wave tube using a PIC solver requires significant time and computational resources, so a quicker (if less accurate) simulation method is highly desirable for the initial design.

The method used here is to simulate a single period of the structure, using an eigenmode solver with periodic boundaries as shown in Figure 2.15 and then to calculate the effect of the slow wave structure on the electron beam in post processing [18]. Simulation of purely the electromagnetic performance of the slow wave structure allows the effects of discontinuities (such as waveguide bend types, beam tunnel width and waveguide widths) on the dispersion characteristics of the slow wave structure to be studied in more detail than the simple analysis presented earlier.

Whilst dramatically faster, this technique does have significant disadvantages, as it only simulates the first mode of a periodic structure correctly (though the equations used in post processing could be extended to higher modes if desired) and as the structure is infinite, it does not include the effects of any mismatches from the mode transducers. Despite these limitations, it is a useful technique that allows the electromagnetic portion of the design to be iterated quicker than using a PIC solver. Both simulation techniques are now used in the design example shown below.
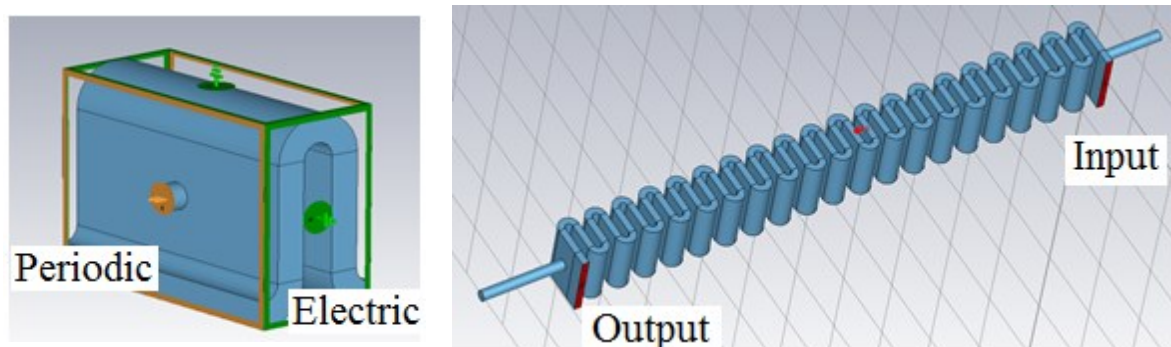
Figure 2.15 – Single period with boundary conditions used in the eigenmode solver (electric on sides, periodic in the direction of propagation) and a short section of slow wave structure used in the PIC solver.

2.3.2   Analytical design

As the groove in existing serpentine structures has an aspect ratio of around 10 : 1 [19] and needs to be over 1.5 mm wide for machinability (milling bits are commonly found down to around 1 mm and the minimum slot size must be larger than the tool diameter so the faces can be cut separately) a reasonable starting point for the waveguide width (*a*) is around 20 mm. An exact value for *a* can be calculated by

choosing an operating frequency. Around 10 GHz was chosen, due to the local availability of X-band waveguide hardware. As mentioned earlier:

$$f_{op} = 1.25 f_c \qquad (2.33)$$

The waveguide cutoff frequency can be expressed in terms of the width as [8]:

$$f_c = \frac{c}{2a} \qquad (2.34)$$

Combining and re-arranging the above two equations gives:

$$a = \frac{5c}{8 f_{op}} \qquad (2.35)$$

Using 10 GHz as the operating frequency then gives:

$$a = 18.7 \; mm \qquad (2.36)$$

Round numbers are highly desirable for manufacturability so it is worth adjusting the operating point slightly, therefore a is chosen to be 18 mm, giving an operating frequency of 10.5 GHz.

The equation that relates electron beam velocity to voltage is [3]:

$$v_{beam} = \sqrt{\frac{2eV}{m_e}} \qquad (2.37)$$

Therefore, the maximum beam velocity possible with a 10 kV accelerating voltage is:

$$v_{beam} = 0.2c \qquad (2.38)$$

However, it is worth keeping some margin in hand so the system will be designed for $v_{beam} = 0.18\, c$. As stated earlier, v_T is given by:

$$v_T = \frac{\omega p}{\phi_T} \qquad (2.39)$$

And as $\pi < \phi_T < 2\pi$ for a forward wave, where n = 0 (the first spatial harmonic):

$$\frac{\pi v_T}{\omega} < p < \frac{2\pi v_T}{\omega} \qquad (2.40)$$

Targeting an operating frequency of 10.5 GHz with a phase velocity of 0.18c then gives:

$$2.57 \ mm < p < 5.14 \ mm \tag{2.41}$$

A good starting value is a round number at the centre of this range, therefore $p = 4 \ mm$.

As the phase velocity along the beam tunnel will be approximately equal to the electron beam at the operating point, the width of the waveguide can be calculated and subtracted from p to calculate the wall thickness. Since the phase velocity is:

$$v_p = \frac{\omega}{\beta} \tag{2.42}$$

Substituting 2.42) into (2.26) gives:

$$b = \frac{2.311 v_p}{2\pi f} \tag{2.43}$$

Substituting $f_{op} = 10.5$ GHz and $v_{beam} = 0.18c$ into Equation (2.43) gives $b = 1.89$ mm, leaving a wall thickness of 2.1 mm (remember p is a single U-bend), which is acceptable for in-house machining. It is worth noting that if this design was not constrained by the accelerating voltage then these equations could be reversed to calculate the accelerating voltage needed for a given wall thickness and waveguide height (b).

An initial value for s can be calculated by substituting Equation 2.28, $v_p = 0.18c, \omega = 2\pi \times 10.5$ GHz, $a = 18$ mm, $p = 4$ mm and $n = 0$ into Equation 2.27, giving:

$$v_T = \frac{\omega p}{\left(s + \frac{\pi p}{2}\right)\sqrt{\left(\frac{\omega^2}{c^2} - \frac{\pi^2}{a^2}\right)} + \pi + 2\pi n} \tag{2.44}$$

$$0.18 \times 3E8 = \frac{2\pi \times 10.5E9 \times 4E - 3}{\left(s + \frac{\pi 4E - 3}{2}\right)\sqrt{\left(\frac{2\pi \times 10.5E9^2}{3E8^2} - \frac{\pi^2}{18E - 3^2}\right)} + \pi} \tag{2.45}$$

Solving the above equation gives $s = 6.7$ mm, which (as it is an initial value) can be rounded to 7mm. The slow wave structure is now fully defined, and Table 2.1 summarises the results.

Table 2.1 – Summary of slow wave structure parameters from analytical design

Parameter	Symbol	Value	Unit
Electron beam velocity	v_{beam}	0.18c	
Straight length	s	7	mm
Period length	p	4	mm
Waveguide width	a	18	mm
Waveguide height	b	1.89	mm
Beam tunnel diameter	d_b	1.89	mm

Figure 2.16 shows the dispersion diagram for a serpentine slow wave structure with the parameters from Table 2.1. The diagram shows that the beam is synchronised with the zeroth spatial harmonic (in the forward wave region) at the operating point and crosses the backward wave from the first spatial harmonic well away from the point where the zeroth and first harmonics intersect (a source of instability)
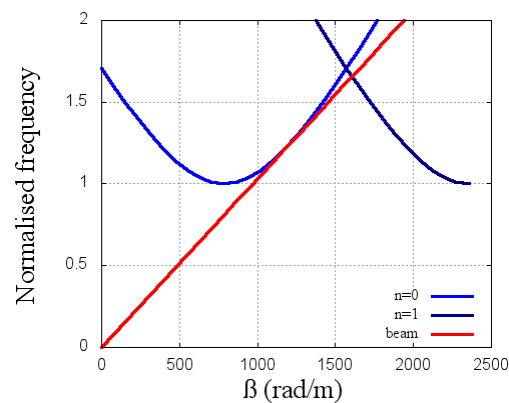
Figure 2.16 – Dispersion diagram for the slow wave structure from Table 2.1, showing the electron beam, zeroth and first spatial harmonics.

2.3.3   Eigenmode solver

The structure shown in Table 2.1 is now simulated using the eigenmode solver. This will give an approximation to the interaction impedance and a more accurate phase velocity as the effect of the discontinuities in both the beam and the bend will be taken into account. Figure 2.17 shows the

dispersion curve of the zeroth spatial harmonic (forward wave only) and the electron beam, thus demonstrating that there is good synchronisation between the beam and wave at the operating point as intended. Figure 2.18 confirms that the phase, group and beam velocities all intersect at the operating point. Figure 2.19 shows the variation of the interaction impedance with frequency. Note that the electric field values used to calculate the interaction impedance are taken along the centre of the beam tunnel, so this calculation will slightly underestimate the coupling impedance (as the electric field strength is greater at the outer edge of the beam tunnel).
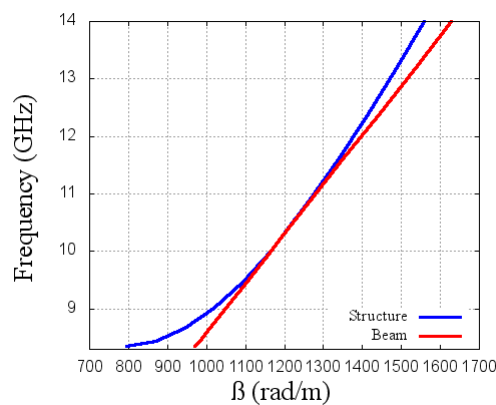
Figure 2.17 – Dispersion diagram showing the forward wave portion of the zeroth spatial harmonic.
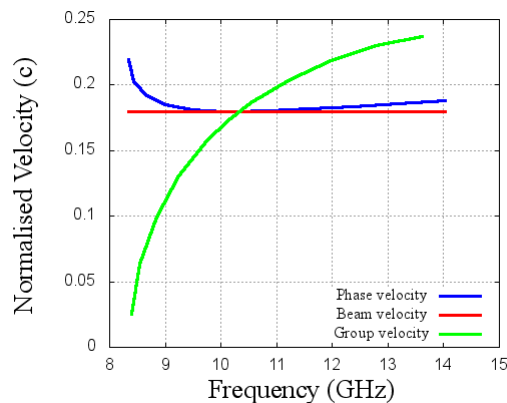
Figure 2.18 – Phase, group and beam velocities of the slow wave structure.
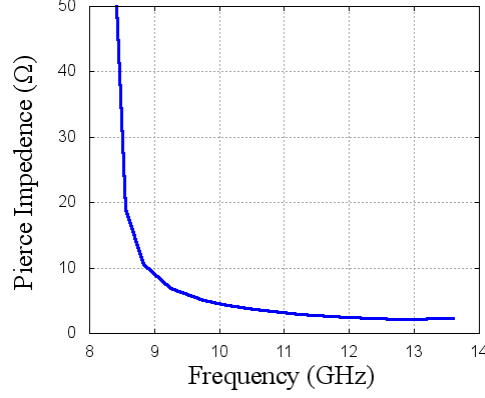
Figure 2.19 – Interaction impedance of slow wave structure.

The Interaction impedance, κ, can be used to calculate the number of periods needed for a set gain and the maximum allowed deviation in the electron beam velocity. Substituting $b = \pm1$ into Equation (2.17) gives the allowable maximum and minimum phase velocities that will give nominal gain when interacting with the beam, as follows:

$$u_0 = (1 \pm C)v_T \tag{2.46}$$

From the simulation, $\kappa = 4\ \Omega, V_0 = 8.3\ \text{kV}, I_0 = 0.1\ \text{A}$ and so:

$$C = \sqrt[3]{\frac{4}{4 \times 8300/0.1}} \tag{2.47}$$

Which gives $C = 0.0229$, therefore as $u_0 = 0.18c$ we can write:

$$u_+ = 1.0229 \times 0.18c \ , \ \ u_- = 0.9771 \times 0.18c \tag{2.48}$$

Therefore:

$$0.176 < v_T < 0.184c \tag{2.49}$$

Consequently, the bandwidth of the tube can be increased by either increasing the beam velocity (such that the lower bound of v_T matches that of the structure) or, as the electron beam is currently at its maximum value, by reducing the phase velocity at the operating point. As only a small change is needed and p cannot be significantly reduced without affecting the machinability of the structure, adjustment

63

of *s* seems most sensible. The new value for *s* can be determined by recalculating Equation 2.44 for the lower limit of v_T rather than the beam velocity, as shown below:

$$0.176 \times 3E8 = \frac{2\pi \times 10.5E9 \times 4E-3}{\left(s + \frac{\pi 4E-3}{2}\right)\sqrt{\left(\frac{2\pi \times 10.5E9^2}{3E8^2} - \frac{\pi^2}{18E-3^2}\right)} + \pi} \tag{2.50}$$

Which gives $s = 7.8\ mm$, However, as the beam voltage is easy to adjust (and will decrease as *s* is increased) we can round this to $s = 8$ mm. Figure 2.20 shows the phase and beam velocities of the new parameter set ($s = 8$ mm, $p = 4$ mm, $a = 18$ mm, $v_{beam} = 0.18c$), showing that there is an even distribution of error above and below the beam line. It should be noted that the minimum value for v_T is below the lower bound from (2.49) so the beam voltage will need to be slightly reduced as expected.
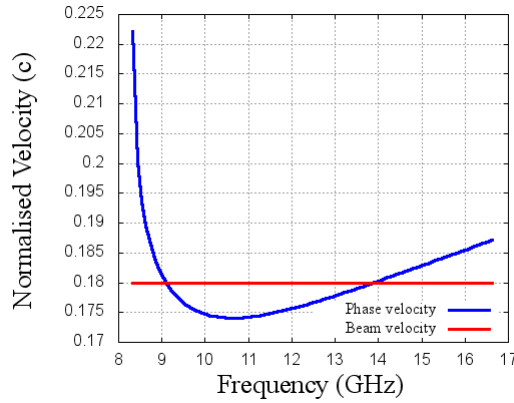
Figure 2.20 – Phase velocity against frequency for s = 8, p = 4 and a = 18 mm.

Pierce small signal theory gives the gain (repeating Equation 2.14) as:

$$G = -9.54 + 47.3CN \tag{2.51}$$

Where N is the number of wavelengths along the beam tunnel. It is more useful to rewrite N in terms of the other parameters, giving:

$$G = -9.54 + 47.3C\frac{pN_p}{\lambda_T} \tag{2.52}$$

Where N_p is the integer number of periods and λ_T is the wavelength of the wave along the beam tunnel. As $v_T = 0.18c$ and $f_{op} = 10.5$ GHz, we then obtain:

$$\lambda_T = \frac{0.18 \times 3 \times 10^8}{10.5 \times 10^9} \tag{2.53}$$

This yields $\lambda_T = 5.1 \ mm$ (λ_T being the wavelength along the beam tunnel). Assuming a desired gain of 20 dB, this result can be substituted into (2.52) to give:

$$N_p = \frac{(20 + 9.54) \times 5.1 \times 10^{-3}}{47.3 \times 0.0229 \times 4 \times 10^{-3}} \tag{2.54}$$

The final result is $N_p = 34$. However, as this value represents an absolute minimum, some rounding is sensible, leading to the final value $N_p = 40$. N.b. there are two periods per section so the design will have 20 sections.

2.3.4 PIC solver

The final stage of the design is to verify the analytical design with the CST Studio PIC solver [20]. Table 2.2 summarises the design, including the changes made from analysis of the eigenmode solver output. Figure 2.21 NO, 20 shows the result of a PIC solver run with the parameters from Table 2.2 showing the voltage at the ports against time. As seen in the figure the input signal (blue) starts at $t = 0$ and ramps to 0.3 V by $t = 1$. The output from port 2 remains at zero until $t = 3$ (due to the time taken for the electron beam to traverse the slow wave structure) and then ramps up to 0.85 V showing that the tube has a gain of 9 dB. Throughout the simulation there is no appreciable output from the input port (red) demonstrating that the interaction with the backward wave is minimal and consequently that the tube should be stable.

Table 2.2 – Parameter set used for initial PIC simulations.

Parameter	Symbol	Value	Unit
Electron beam velocity	v_{beam}	0.18c	
Electron beam current	I_0	0.1	A
Straight length	s	8	mm

Period length	p	4	mm
Waveguide width	a	18	mm
Waveguide height	b	1.89	mm
Beam tunnel diameter	d_b	1.89	mm
Periods	N_p	40	
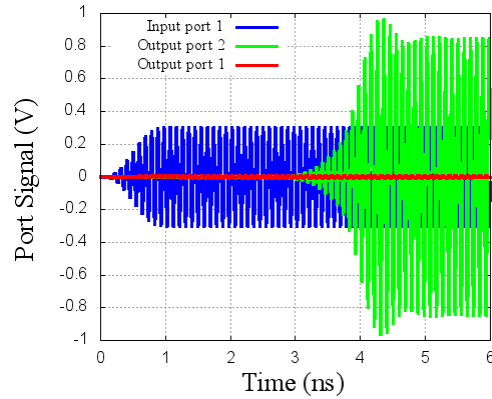
Figure 2.21 – Port signals for parameter set in Table 2.2.

The structure therefore appears to be working well, although with a lower gain than predicted (9 dB rather than 20 dB). Consequently, it is worth investigating the bandwidth of the device, as a wideband tube should allow looser manufacturing tolerances.

There are two ways of plotting the bandwidth of a tube using the PIC solver. The usual way is to simply conduct a parameter sweep of the excitation frequency; however, whilst accurate, this requires a large number of simulations and a correspondingly large computation time. An alternative technique is to conduct one simulation run where the excitation signal is a constant amplitude sine sweep (i.e. a chirp) and then take a Fourier transform of the output signal.

Figure 2.22 shows the result using this technique, giving several curves of gain against frequency for different beam velocities. As can be seen in the figure with $v_{beam} = 0.18\,c$ there is a good balance between bandwidth and peak gain. As expected, if the beam velocity is increased the frequency of maximum gain decreases whilst the gain at this point increases, resulting in a higher gain but lower bandwidth device. When the beam velocity is lowered the gain becomes lower but flatter, thus

demonstrating that the design beam velocity is close to the optimal value (changes in the beam velocity by ± 3 % both cause substantial decreases in gain at the target frequency of 10.5 GHz).
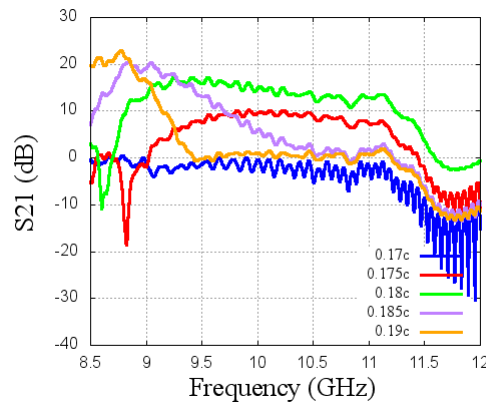
Figure 2.22 – Gain against frequency for different beam velocities.

It appears that the beam velocity is close to optimal for the current set of parameters, however as mentioned earlier the beam velocity, v_{beam}, needs to be simultaneously tuned with the waveguide height, *b*, (which has a strong effect on the gain) and consequently the optimiser should be used to investigate whether the value of b is suboptimal.

It is worth noting that the optimiser should be used carefully with only a single frequency point. Lower frequencies have higher gains, so the optimiser will effectively reduce the operating point of the tube to one that, whilst having higher gain, is not particularly useful. Consequently, it is recommended to use a single frequency point with a fixed value for a (which fixes the operating point) and prudent to only optimise v_{beam}, and *b* together (with fixed *s* and *p*) or vice versa.

Figure 2.23 shows the port signals for the optimised tube, again the input signal (blue) is at 0.3 V however the output (green) has been increased to 1 V giving a gain of 10.5 dB showing an improvement of 1.5 dB and without changing the electron beam or the number of periods.

A comparison of the initial and optimised parameters is shown in Table 2.3 and shows that only *b* has changed significantly (from 1.89mm to 2mm), with v_{beam}, *s* and *p* remaining unchanged, which

suggests that the analytical design process presented here gives a reasonably optimal set of parameters although it overestimates the gain per period of the structure.
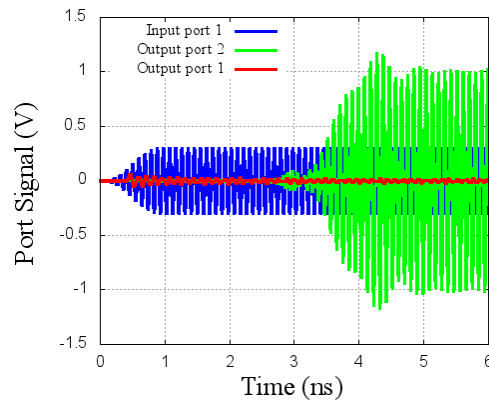
Figure 2.23 – Port signals obtained using the optimised parameter set.

Table 2.3 – Comparison of analytical and optimised parameters.

Parameter	Symbol	Initial	Optimised	Unit
Electron beam velocity	v_{beam}	0.18	0.1797	c
Electron beam current	I_0	0.1	-	A
Straight length	s	8	8.001	mm
Period length	p	4	4.0172	mm
Waveguide width	a	18	-	mm
Waveguide height	b	1.89	2.01	mm
Beam tunnel diameter	d_b	1.89	2.01	mm
Periods	N_p	40	-	

The final step is to simulate the tube with a sever, which is required for stability as it prevents the backward wave from reaching the input. Figure 2.24 shows a screenshot from CST studio of a complete tube which has a small initial section, a sever and then a 20-section slow wave structure where the majority of the beam-wave interaction happens. The beam and microwave power flow from right to left and the ports either side of the sever are terminated with matched loads, although waveguide ports are used in simulation as they are perfectly matched and significantly less intensive to simulate than a waveguide load.
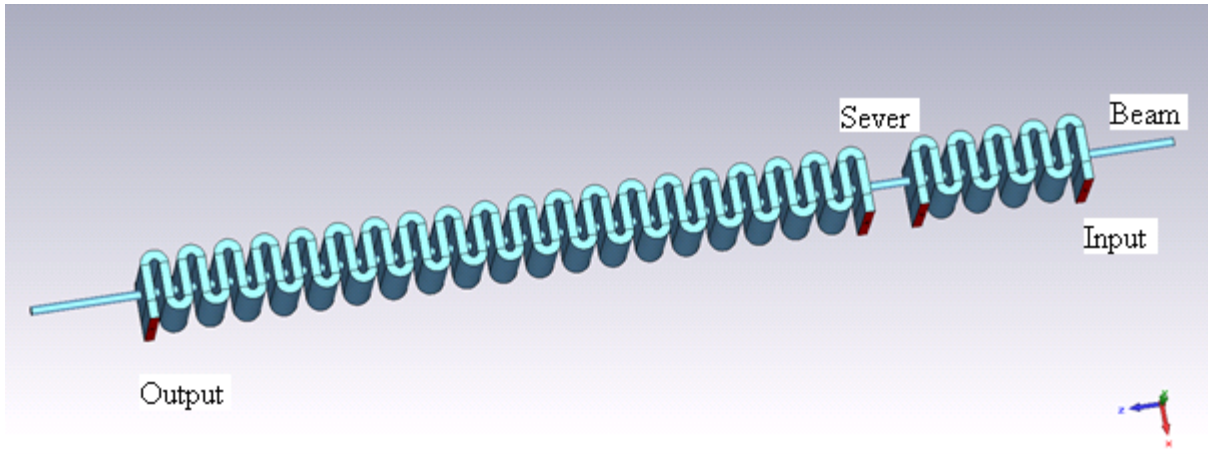
Figure 2.24 – Screenshot of structure with sever.

Figure 2.25 shows the port signals of the tube when excited with a continuous 10.5 GHz signal of 0.3 V amplitude (blue) at port 1. The output at port 4 (purple) is from the exciter section, showing a small amount of gain, which would normally be absorbed by a waveguide load. The main output (green) shows an output slightly below 1 V giving an expected 10 dB of gain. Again, both input ports (1 and 3) show a minimal amount of power indicating that there is a minimal interaction between the beam and the backward wave, so the tube is likely to be stable. Overall the port signals show that the introduction of the sever has not affected the operation of the tube as its performance is similar to the results presented earlier.
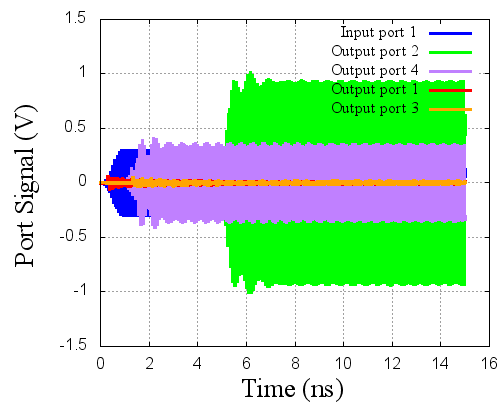
Figure 2.25- Port signals for tube with sever.

Figure 2.26 shows the electron beam velocity against position along the tube, demonstrating that the slow wave structure is causing bunches to form in the electron beam. In addition, the average beam velocity decreases along the length of the slow wave structure, indicating that there is a net energy transfer from the electron beam to the wave as expected.
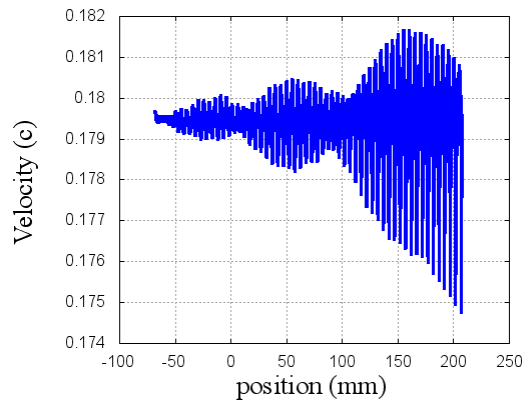
Figure 2.26 – Electron beam velocity against distance from the start of the electron beam.

2.4   Conclusions

The small signal theory of travelling wave tubes has been introduced and used to analyse a serpentine slow wave structure. The analysis has then been used to create a set of design equations that were applied to the design of a 10 GHz serpentine travelling wave tube. The serpentine structure was then simulated using an eigenmode solver with additional post processing that is significantly quicker than full PIC simulations. The eigenmode simulations were then analysed and used for further optimisation of the design. Finally, the design and eigenmode simulation techniques were then verified by simulating the structure using a PIC solver with the results from the solver showing that the parameters calculated in the analysis produced a working travelling wave tube that exhibits gain and a net energy transfer from the electron beam to the guided electromagnetic wave.

References

[1]   J. R. Pierce, *Traveling-wave Tubes*. Van Nostrand, 1950.

[2]   G. D. Sims and I. M. Stephenson, *Microwave tubes and semiconductor devices*. Interscience Publishers, 1963.

[3]   A. S. Gilmour, *Principles of Traveling Wave Tubes*. Artech House, 1994.

[4]   J. Rowe, "A large-signal analysis of the traveling-wave amplifier: theory and general results," *IRE Transactions on Electron Devices,* vol. 3, no. 1, pp. 39-56, 1956.

[5]   J. G. Meeker and J. Rowe, "Phase focusing in linear-beam devices," *IRE Transactions on Electron Devices,* vol. 9, no. 3, pp. 257-266, 1962.

[6]   J. D. Wilson, H. C. Limburg, J. A. Davis, I. Tammaru, and J. P. Vaszari, "A high-efficiency ferruleless coupled-cavity traveling-wave tube with phase-adjusted taper," *IEEE Transactions on Electron Devices*, vol. 37, no. 12, pp. 2638-2643, 1990.

[7]   J. H. Booske *et al.*, "Accurate parametric modeling of folded waveguide circuits for millimeter-wave traveling wave tubes," *IEEE Transactions on Electron Devices,* vol. 52, no. 5, pp. 685-694, 2005.

[8]   N. Marcuvitz, *Waveguide Handbook*. McGraw-Hill, 1951.

[9]   K. T. Nguyen *et al.*, "Design methodology and experimental verification of serpentine/folded-waveguide TWTs," *IEEE Transactions on Electron Devices,* vol. 61, no. 6, pp. 1679-1686, 2014.

[10]   G. Dohler, D. Gagne, D. Gallagher, and R. Moats, "Serpentine waveguide TWT," in *Electron Devices Meeting, 1987 International*, 1987, pp. 485-488: IEEE.

[11]   R. Zheng and X. Chen, "Parametric simulation and optimization of cold-test properties for a 220 GHz broadband folded waveguide traveling-wave tube," *Journal of Infrared, Millimeter, and Terahertz Waves,* vol. 30, no. 9, pp. 945-958, 2009.

[12]   S. Liu, "Study of propagating characteristics for folded waveguide TWT in millimeter wave," *International Journal of Infrared and Millimeter Waves,* vol. 21, no. 4, pp. 655-660, 2000.

[13]   H.-J. Ha, S.-S. Jung, and G.-S. Park, "Theoretical study for folded waveguide traveling wave tube," *International Journal of Infrared and Millimeter Waves,* vol. 19, no. 9, pp. 1229-1245, 1998.

[14]   Y. H. Na, S. W. Chung, and J. J. Choi, "Analysis of a broadband Q band folded waveguide traveling-wave tube," *IEEE Transactions on Plasma Science,* vol. 30, no. 3, pp. 1017-1023, 2002.

[15]   S.-T. Han *et al.*, "Low-voltage operation of Ka-band folded waveguide traveling-wave tube," *IEEE Transactions on Plasma Science,* vol. 32, no. 1, pp. 60-66, 2004.

[16]   *TWT analysis using the CST modules*. Available: https://www.cst.com/Content/Events/UGM2009/6-3-2-Traveling-Wave-Tube-TWT-analysis-using-CST-STUDIO-SUITE-2009.pdf

[17]   *Traveling Wave Tube Design with Simulation*. Available: https://www.cst.com/solutions/article/traveling-wave-tube-design-with-simulation

[18]   *Simulation of Cold-Test Parameters for Slow-Wave Structure using Eigenmode Solver*. Available: https://www.cst.com/solutions/article/simulation-of-cold-test-parameters-of-a-helical-slow-wave-structure-for-traveling-wave-tube-application-using-eigenmode-solver

[19]   M. F. B. A. Malek, "The analytical design of a folded waveguide traveling wave tube and small signal gain analysis using Madey's theorem," *Progress In Electromagnetics Research,* vol. 98, pp. 137-162, 2009.

[20]   *Microfabricated folded waveguide for broadband traveling wave tube application*. Available: https://www.cst.com/solutions/article/microfabricated-folded-waveguide-for-broadband-traveling-wave-tube-application

3   New Slow Wave Structures

The aim of this Chapter is to investigate new designs for slow wave structures that could improve on the serpentine type that is currently used in millimetre-wave travelling wave tubes [1]. The overall goal is to try to identify a structure that can operate at higher frequencies.

3.1   Introduction

We begin by reviewing the main characteristics of the most common existing designs. Figure 3.1a shows the helical wire slow wave structure, originally developed by Lindenblad and Kompfner [2][3] in the early 1940s for use with a travelling wave tube. This consists of a coil of wire with the electron beam passing through the centre. The coil supports a TM mode that propagates in the direction of the beam. As the major field component of the mode is aligned with the direction of travel of the beam there can be significant coupling between them. It offers extremely large bandwidth and a relatively large beam tunnel area (which impacts on performance) and can easily be constructed using relatively conventional workshop manufacturing techniques [4].

However, as the frequency increases, the pitch of the helix must reduce, necessitating the use of thinner wire to maintain the spacing between the turns. Unfortunately, as the diameter of the wire reduces, resistive losses increase due to a reduction in surface area. This effect is compounded by a decrease in the skin depth due to the increasing frequency. Increased resistive heating in conjunction with the reduction in thermal cooling capacity (as radiation losses are linked to the surface area and conduction to the thickness of the wire) causes a rapid increase of thermal related issues with frequency [5]. The main problem with an increase in the operating temperature of the wire is that it exacerbates the lack of mechanical strength possessed by thin wire, which is required as the coil needs to be self-supporting. In the end, thermal and mechanical problems combine with difficulties in manufacturing to force a change to a different type of structure, the serpentine waveguide [7].

Figure 3.1b shows a serpentine waveguide, first described by Dohler [8], which uses hollow rectangular waveguide that follows a meander layout to form the slow wave structure. The electromagnetic wave now interacts with the electron beam only at discrete points. Furthermore, the discontinuities arising

from any abrupt waveguide transitions (such as bends or the beam tunnel) can give rise to reflections that in the end may lead to oscillation [6].
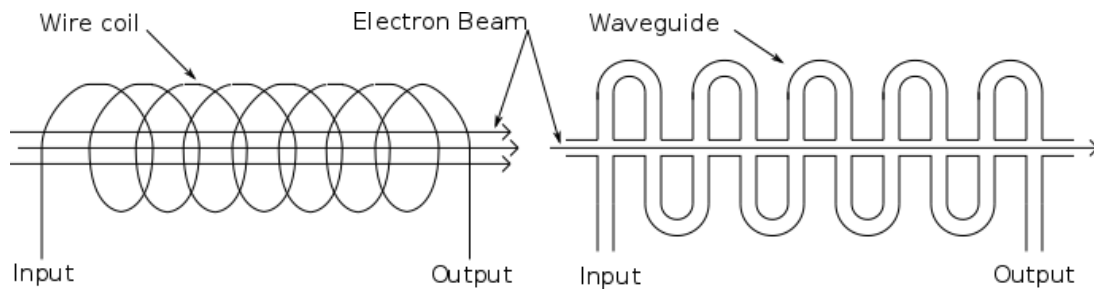
Figure 3.1 a) Coiled wire TWT; b) Serpentine waveguide TWT.

Despite this, the necessary slow wave structure can easily be formed as a hollow rectangular waveguide fabricated by using two machined solid blocks (in the conventional split-block technique). The increased mass of metal conveys rigidity, allows greater heat dissipation and consequently much better power handling, and despite the fact that a groove is required to form the waveguide, can be significantly easier to manufacture than a wound coil. In the limit, extremely small structures of this kind can easily be made by microfabrication techniques such as patterning and deep reactive ion etching of silicon [7]. Figure 3.2 shows an example of one half of a serpentine slow wave structure manufactured using conventional split block techniques. However, once again the performance of a meander layout decreases as its frequency rises. Therefore, it is important to understand how the scaling laws affect the structure so that possible improvements and avenues of research can be identified.
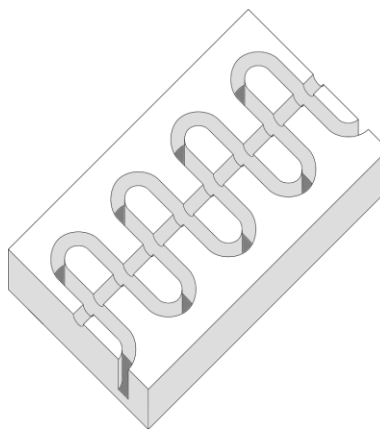
Figure 3.2 - Example of half a split block.

3.2   Effects of Scaling on Serpentine Slow Wave Structure

The aim of this section is to understand the effect of frequency scaling on the serpentine based travelling wave tube so that potential areas of research can be identified. First the effects of higher frequencies on the microwave part of the tube, the slow wave structure, will be explored before linking these changes in geometry back to the effect on the beam. Finally, the beam will be reintroduced to the slow wave structure so that the overall effects of scaling a serpentine TWT to a higher frequency can be described.

As discussed in Chapter 2, the travelling wave interaction can be described in terms of an induced current on an LC transmission line. Therefore, it is useful to consider the microwave performance of the slow wave structure separately from that of the electron beam before linking them in terms of the induced current. This is the approach taken here, with the effects of scaling on the microwave structure discussed, then the effects of this scaling on the electron beam before linking them by looking at the effect of the scaled beam current on the scaled slow wave structure.

In the absence of an electron beam, the slow wave structure's operating frequency can be increased by shrinking its dimensions. However, there is no guarantee that this will be both a linear relationship and that the scaling will be the same for every part of the geometry. Normal complicating factors include frequency dependant dielectrics, frequency dependant loss (normally skin depth related) and the aspect ratio of discontinuities becoming awkward.

However, waveguide structures that only consist of air and metal can normally be scaled successfully, as the only frequency sensitive parameter is the skin depth. Because loss is usually a broadband effect, the structure can normally be split into two components, a frequency dependant attenuator and a lossless network. In this way the structure is considered be made solely from vacuum and perfect electrical conductor (PEC) and thus will be scale invariant, meaning that if all the dimensions are scaled by the same factor - for example all the lengths are doubled - the shape of its frequency response will stay the same but will be shifted to a different frequency. For a rectangular waveguide operating in a TE10 mode, the variable that affects its frequency of operation, by defining the cut off frequency, is the waveguide's width (a). Therefore, it is useful to rewrite the other parameters that define the overall geometry in terms

of the width, for example as b = 1.2*a. The advantage of this method is that there is now a clear link to the operating frequency for all the lengths of the structure.

Consequently, we can say that as the operating frequency is increased, whilst the dispersion characteristics will stay the same, the ohmic losses within the device will increase. In addition, as the beam is contained within the structure then the space available for the electron beam must reduce.

With this in mind, Figure 3.3 shows a more detailed diagram of one period of the structure, with the waveguide path length (L), height (b), length (s), beam tunnel diameter (d_b) and period length (p) labelled. The width (a) is normal to the page. As discussed in Chapter 2, the parameters that have the main effect on gain are related to the interaction cavity, in particular the beam tunnel diameter and the waveguide height as these specify the cylinder of the beam inside the waveguide. These effects of these two parameters on the structures performance will be discussed in more detail below.
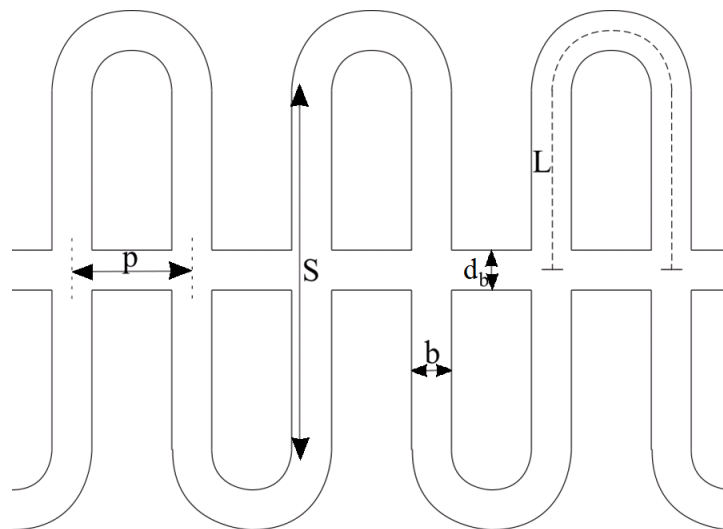
Figure 3.3- Labelled diagram of serpentine slow wave structure.

As stated by [9], the waveguide height (b) sets the impedance of the waveguide, which here means the ratio of stored energy between the electric and magnetic fields. Broadly, a higher impedance means that more of the energy is stored in the electric field, causing a stronger interaction with the beam. The beam tunnel diameter (d_b), as expected, determines the size of the aperture in the waveguide that the beam passes through, which governs two key areas of performance. Firstly, it determines the beam current

and secondly it presents a discontinuity to the waveguide, the effects and limits of these will now be discussed.

The beam current passing through the tunnel provides the energy that is used in the travelling wave interaction, therefore a higher current is often needed to reach key specifications such as gain or maximum power output. A larger beam tunnel area allows more current to pass through the tube whilst maintaining the same current density. This is desirable as the current density is limited by the strength of the magnetic confinement field.

However, the required aperture in the waveguide presents a discontinuity, which causes a reflection in proportion to the tunnel's size. Beyond a certain point, the reflection will overwhelm the structure and it will cease to operate correctly. The effect of the discontinuity is also in proportion to the height of the waveguide [9]. Therefore, these two requirements are in conflict with each other: a larger beam tunnel will allow higher currents, but beyond a limit will prevent operation. As this limit is related to the height of the waveguide it is generally given as a multiple of the height (b). As given in [6] the maximum diameter of the beam tunnel is approximately $1.2b$; although as stated by [10] simple analytical equations are only accurate for beam tunnel diameters equal or less than b.

The height of the waveguide (b) sets a limit on the maximum beam current that can pass through the device and that this limit reduces with frequency. As the ohmic loss per cm of the waveguide will also increase with frequency we can say that the net terminal gain of the device will sharply reduce with frequency, reaching no net terminal gain at a limit. In order to extend the operating frequency of the travelling wave tube a new style of slow wave structure is required that either increases the available gain or decreases the losses within the slow wave structure.

3.3   Design Improvements

Based on the concepts of the preceding section, several possible methods of raising the 0dB point can be identified. As the crossing point is caused by the intersection curves representing the variation of loss with frequency and possible gain with frequency, either could be improved. As the loss is due to

fundamental physics (loss of surface conduction caused by the skin effect) it is unlikely that much progress can be made in attempting to reduce it. However, it should be possible to increase the gain by enlarging the beam tunnel thus allowing a higher beam current without increasing the beam current density. This is the approach taken here and is discussed in more detail below.

Inspection of the serpentine style structure suggests that there are several avenues for increasing the cross-sectional beam area. The first observation is that, as discussed earlier, the beam tunnel is proportional to the waveguide height (b), which is also proportional to the waveguide's width (a). Therefore, by increasing the width of the waveguide whilst keeping the frequency constant will allow for the beam tunnel to be increased, introducing additional higher frequency modes (e.g. TM10, TE30 etc.) which can be coupled to the beam, as shown in [11][12].

Higher order modes can be exploited in two ways. The usual approach is to introduce additional lossy elements to suppress the lower modes [13]. Alternatively, mode filters can be used to reduce the amount of coupling into them. Designing a structure to reduce inter mode coupling is difficult and was therefore generally avoided in the past. However, with the introduction of modern CAD methods and computational solvers it appears that more complicated structures can be designed relatively easily, as shown by [14][15][16].

The next observation is that while increasing the width of the waveguide (a) allows a proportional increase in its height (b), the inverse is not strictly true, i.e. the waveguide height has a certain independence. As stated earlier, the beam tunnel diameter is proportionate to the height of the waveguide (b) so a design that maximises the waveguide height will also maximise the beam tunnel cross sectional area, a point which does not appear to have been specifically noted in the literature.

Another observation is that these restrictions on the beam tunnel are caused by the need for the beam not to cause sizeable waveguide discontinuities. Once the diameter of the beam tunnel goes over a certain size (generally defined as 1.2 units of the waveguide height) the magnitude of its reflection is then large enough that the slow wave structure ceases to operate as a transmission line. However the

discontinuity from the beam tunnel could be compensated for, allowing a larger beam tunnel or better microwave performance, and has been studied by [20].

Alternatively, a beam tunnel of the same area but a different shape could have a lower reflection coefficient of particular interest is a slot style beam tunnel. Figure 3.4 shows an example of a slot beam tunnel, labelling the two key dimensions of the slot: its width (X) and length (Y). As stated in [9], the reflection is much more dependent on the width of the slot than its length. The independence of the slot length and width on the discontinuity can be easily explained with an understanding of the field structure within a rectangular waveguide supporting a TE10 mode.
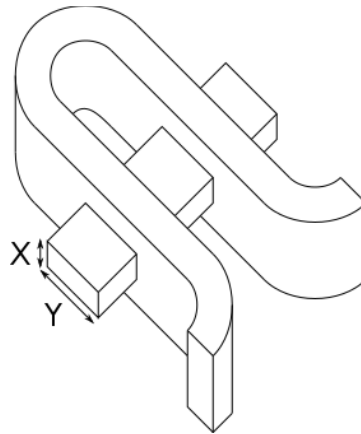
Figure 3.4 - Slot beam slow wave structure.

For the TE10 mode the centre of the waveguide is the line of electric field symmetry, meaning that there is no surface current along the metal at this point. As there is no current within the metal here, there is no need for this part of the structure to be conductive, and the guide could be split into two if desired. A relevant example of this effect is the traditional VSWR measurement technique that uses a slotted line in order to insert a probe into the waveguide to allow direct measurement of the electric field strength.

Attempts using this approach have previously been made [21][22][23]. The difficulty with this design is the relative instability of a sheet electron beam compared to a circular beam, as stated in [24]. It should be noted that the logical extension of the slot beam to a waveguide spiral has been studied extensively [25].

79

It is also be possible to increase the gain by increasing the coupling impedance. However most approaches involve adding a component (ferrule, dielectric blob, slot etc) inside the waveguide, which has a severe effect on the minimum feature size and the complexity of manufacture and probably explains why there only seem to be simulation studies available in the literature [17][18][19].

In summary several possible approaches to improving the operating frequency of the device by increasing the maximum theoretical gain of the slow wave structure have been identified. They are, using higher modes, increasing the height of the waveguide, matching the beam tunnel discontinuity, increasing the length of the slot, and increasing the coupling impedance. There has been substantial work conducted on most of the approaches; however, no work appears to have been done on increasing the height of the waveguide used within the serpentine slow wave structure. In fact, all tubes use similar aspect ratios, generally between 5:1 and 10:1 As the beam/gap coupling equation is fairly complicated, it may be possible to find an alternative to the operating point $\beta b = 2.331$ proposed by Dohler [8]. Consequently, this seems a worthwhile topic to explore.

3.4   Increasing Waveguide Height

Dohler [8] gives the interaction impedance of a beam and a gap as:

$$\kappa = Z_w \left(\frac{1}{\beta p} \frac{2\sin\left(\frac{\beta_T b}{2}\right)}{\beta_T b} \right)^2 \tag{3.1}$$

Where Z_w is the impedance of the waveguide, given by:

$$Z_w = 377 \frac{2b}{a} \frac{1}{\sqrt{1 - \frac{\lambda^2}{\lambda_c^2}}} \tag{3.2}$$

Now, β_T is the propagation constant of the slow wave structure along the tunnel. As it is desirable for the point of maximum interaction impedance to be at the operating frequency, we can write:

$$\beta_T = \frac{\omega_{op}}{v_T} \tag{3.3}$$

Collating constants then gives:

$$\kappa = Kb \left(\frac{2\sin\left(\frac{\beta_T b}{2}\right)}{\beta_T b} \right)^2 \tag{3.4}$$

Equation 3.4 can then be solved to find a maximum at $b\beta_T = 2.331$. However as the function is cyclic, there should be additional local maxima and minima at values above 2.331, although these will result in a lower coupling impedance. Setting $K = 1$ (as it will have no effect on the turning points) and differentiating 3.4 with respect to b gives:

$$\frac{2\cos\beta_T b + 2\beta_T b \sin\beta_T b - 2}{\beta_T^2 b^2} = 0 \tag{3.5}$$

Making the substitution $\beta_T = \frac{d}{b}$ then gives:

$$\frac{2\cos d + 2d\sin d - 2}{d^2} = 0 \tag{3.6}$$

Figure 3.5 shows a plot of Equation (3.4), the first peak at $\beta_T b = 2.331$ is the value used by Dohler [8]; however, there are an infinite series of higher peaks that can be used.
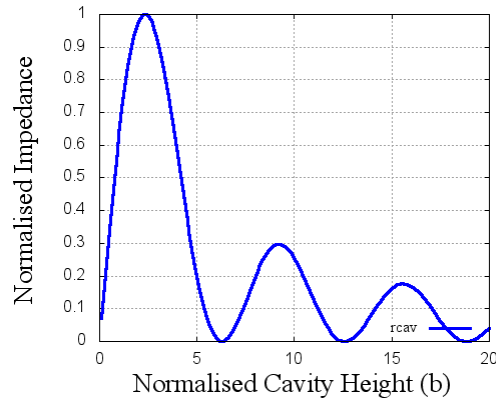
Figure 3.5 – Plot of Equation (3.4) normalised to 1 at the first peak.

As discussed at the start of the chapter increasing b (waveguide height) should allow for higher beam current and a reduced aspect ratio, however the as shown by the previous analysis the strength of the beam coupling will be reduced so further analysis is needed.

3.4.1   Beam Coupling/Current

The effect of increasing b to the second maximum on the beam coupling and current is now evaluated. We first recall Equation 2.4 [26], namely:

$$C^3 = \frac{\kappa}{4V_0/I_0} \tag{3.7}$$

Based on the previous analysis, increasing d to 9.208 will decrease κ (as the peak at 9.208 is lower than at 2.311) but allow an increase I_0 which is restricted by the diameter of the beam tunnel (which in turn is linked to b). We begin by first evaluating the decrease in κ by substituting $b = \frac{d}{\beta_T}$ into Equation 3.4, giving:

$$\kappa = k \frac{d}{\beta_T} \left(\frac{2\sin\left(\frac{d}{2}\right)}{d} \right)^2 \tag{3.8}$$

Consequently, we can write:

$$\frac{\kappa_{old}}{\kappa_{new}} = \frac{d_1 \left(\frac{2\sin\left(\frac{d_1}{2}\right)}{d_1} \right)^2}{d_2 \left(\frac{2\sin\left(\frac{d_2}{2}\right)}{d_2} \right)^2} \tag{3.9}$$

Therefore by substituting $d_1 = 2.331$ and $d_2 = 9.208$ into Equation 3.9 gives:

$$\kappa_{new} = \frac{1}{3.376} \kappa_{old} \tag{3.10}$$

Assuming a constant current density and a circular beam tunnel of the same width as the waveguide height used in Chapter 2, then:

$$I_0 \propto b^2 \tag{3.11}$$

Therefore by increasing b by a factor of $\frac{9.208}{2.331}$ gives

$$I_{new} = 15.604 \, I_{old} \tag{3.12}$$

Inserting Equation 3.10 into Equation 3.7 then gives the value for C^3 in terms of the original parameters, assuming that b is increased to the next maxima and the beam remains at the same current density, as:

$$C_{new}^3 = 4.622 \, \frac{\kappa}{4V_0/I_0} \tag{3.13}$$

Initially, this appears to be a significant improvement on the initial structure, since the gain per unit length will be substantially increased, the aspect ratio reduced and the beam current increased without

83

increasing the space charge density, all of which have advantages for high frequency operation. However, in order for this technique to be used, other changes need to be made to the parameter set as, for example b must be less than p. The impact of increasing b on the other parameters must therefore be evaluated.

3.4.2   Aspect Ratio

The other effect on the tube of high b operation should be a reduction in the aspect ratio of the tube, which will now be evaluated. It can be shown that the aspect ratio is defined by the chosen beam velocity. Given that:

$$f_{op} = \frac{1.25c}{2a}, \beta_T b = d\,, \beta_T = \frac{\omega}{v_{beam}c} \tag{3.14}$$

We can write:

$$\frac{d}{b} = \frac{1.25\pi c}{a v_{beam} c} \tag{3.15}$$

Rearrange and cancelling terms:

$$\frac{a}{b} = \frac{1.25\pi}{d a v_{beam}} \tag{3.16}$$

Letting the aspect ratio $\frac{a}{b} = K_{ab}$ and $d = 2.311$ then:

$$v_{beam} = \frac{1.69}{K_{ab}} \tag{3.17}$$

However if d is increased to 9.208 then:

$$v_{beam} = \frac{0.43}{K_{ab}} \tag{3.18}$$

This result shows that for typical beam velocities ($0.1c \sim 0.3c$) and with the normal operating conditions ($\beta_T b = 2.331, f_{op} = 1.25f_c$), aspect ratios of 16.9~5.6 are possible (matching the range seen in the literature), however with the new operating condition ($\beta_T b = 9.208$) aspect ratios of 1.43~4.3 are now achievable. This result represents a significant improvement that should considerably reduce manufacturing difficulties.

3.5   High-b Tube Analysis

The previous analysis shows that by increasing $\beta_T b$ the beam current can be increased whilst decreasing the aspect ratio, which are both promising improvements to the current design. However before a new tube can be designed to verify the analysis, the effect of high b operation on the other parameters needs to be evaluated. From the previous section:

$$\beta_T b = 9.208 \tag{3.19}$$

Defining b in terms of p and a dimensionless constant K_{bp}, we can write:

$$b = \frac{p}{K_{bp}} \tag{3.20}$$

A lower bound is defined for K_{bp} as $p > b$ in order for the geometry to be realisable. There is not a fixed limit for the upper bound, however it is reasonable to limit it to the value used by the conventional tube designed in Chapter 2 giving a range of $1 < K_{bp} < 2$. Within this range, K_{bp} is strongly linked to the strength of electric field coupling through the beam tunnel (which is a function of both the beam tunnel diameter and the difference between p and b). Consequently, the beam tunnel diameter might be restricted by low values of K_{bp}.

Substituting Equation 3.20 into 3.19 gives

$$\frac{\beta_T p}{K_{bp}} = 9.208 \tag{3.21}$$

As (from Chapter 2):

$$\beta_T = \frac{\phi_T}{p} \tag{3.22}$$

Then:

$$\phi_T = 9.208 \, K_{bp} \tag{3.23}$$

Because $K_{bp} > 1$, the phase shift per period must be greater than 2π. Consequently, this result implies that high-b operation is only possible using higher spatial harmonics . Therefore, before a high-b tube can be designed, further analysis of higher spatial harmonic operation must be conducted.

3.5.1 Higher harmonic operation

Figure 3.6 shows the dispersion diagram from Chapter 2 with the two higher spatial harmonics plotted. Considering the diagram, there are two changes that will allow higher harmonic operation: either the electron beam velocity can be reduced until the beam line intersects the second (or higher) harmonic, or the period length can be increased (which will shrink the dispersion curves until the desired higher harmonic intersects the unchanged beam line).
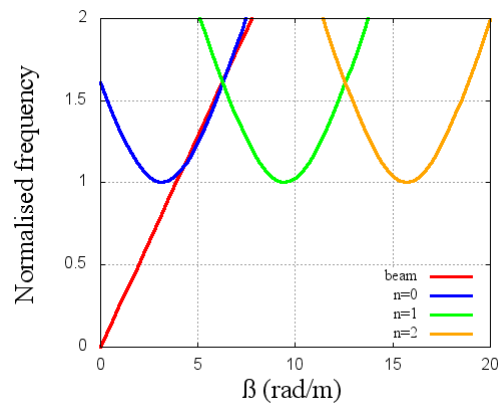
Figure 3.6 – Dispersion diagram showing the first three spatial harmonics and electron beam (s = 8, p = 4, v_{beam} = 0.18c).

Figure 3.7 shows the dispersion diagram for the tube from chapter 2 with additional spatial harmonics and a lower velocity electron beam. Here the electron beam interacts with the forward wave of the second spatial harmonic. However it also crosses a large number of other spatial harmonics. Each crossing with a backward wave could be a source of instability, implying that simply reducing the electron beam velocity of a conventional design is unlikely to work. It should also be noted that reducing the electron beam velocity increases the aspect ratio (see previous section), removing the advantage of high-b operation.
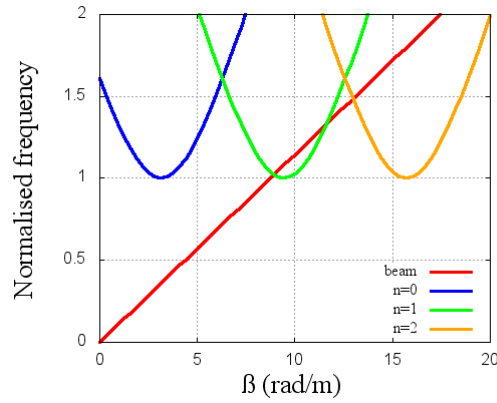
Figure 3.7 - Dispersion diagram showing the first three spatial harmonics and electron beam (s = 8, p = 4, v_{beam} = 0.08c).

Figure 3.8 shows the dispersion diagram for a tube with the same electron beam but an increased value of p. The beam now intersects with the second spatial harmonic and the number of beam crossings is reduced. However, the point of intersection between the forward and backward wave has been reduced, although the shape and intersections of the dispersion curve are now similar to the conventional tube. The intersection between forward and backward waves is determined by the ratio of p to L, as L has a significant contribution from the bend that as p is increased (obviously whilst holding the cutoff frequency the same) then the crossing point will reduce, even if s is reduced to zero.
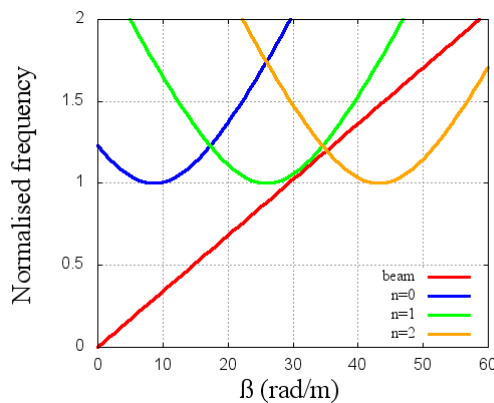
Figure 3.8- Dispersion diagram for slow wave structure with an increased value of p (s = 8, p = 10, v_{beam} = 0.18c).

It is worth briefly considering why the conventional design is stable, despite the backward wave crossing, as the same conditions could then be applied to a high-b design. Nguygen [20] states that in

order to avoid oscillation the beam line must cross the backward wave slightly below the point where the forward and backward waves intersect.

Additionally (not considered in the literature) the interaction impedance has a null caused by the sin term in Equation 3.4. Considering the earlier Figure 3.6, the frequency of the intersection between the beam and the backward wave is at $1.6f_c$. The value of b has been chosen such that the first peak aligns with the operating point ($1.25f_c$) which means that the first null (the point of no interaction between the beam and the slow wave structure) falls at around $3f_c$.

Whilst the null is not aligned due to the sharp roll off of Equation (3.4), the interaction of the beam with the backward wave will still be substantially less than the interaction with the forward wave at the operating point. Consequently, we can say that as the conventional tube is stable, provided the tube fulfils the condition set out by [20] and the interaction impedance in the high-b tube has the same ratio between the operating point and the backward wave crossing then the tube is also likely to be stable.

Accordingly, the ratio between operating frequency and backward wave interaction is 1:1.28 (1.25:1.6) for the conventional tube, with the ratio of peak to null of 1:2.6 (2.311:6.08), for the high-b tube in Figure 3.8 the ratio of operating point to backward wave crossing is 1:1.09 (1.1:1.2) and the ratio of peak to null is 1.32 (9.208:12.2). Therefore, whilst the operating point is closer to the point of intersection (because the ratio between the peak and the null has been reduced) the interaction impedance at the point where the beam crosses the backward wave should be lower in the high-b design. Consequently, as the new design can fulfil both conditions then stability is expected.

3.5.1.1 Effect of Harmonic Operation on Operating Point

Previously the parameters s and p were chosen so that the point of inflexion of the phase velocity curve was at the operating frequency and synchronised to the beam velocity, giving maximum bandwidth. However further analysis is required to see whether this condition can be fulfilled for all combinations of operating points and harmonics.

The phase velocity of the tube is given by:

$$v_p = \frac{\omega p}{L\sqrt{\left(\frac{\omega}{c}\right)^2 - \left(\frac{\pi}{a}\right)^2} + \pi + 2\pi n}$$

(3.24)

Equation (3.24) can be normalised using the following substitutions, which rewrite the frequency in terms of the cut-off frequency and the lengths in terms of a. The point of inflexion can then be found by differentiation. Defining the normalised frequency in terms of the cut-off frequency gives:

$$f = f_n \frac{c}{2a}$$

(3.25)

Similarly, defining s and L in terms of a gives:

$$p = p_n a \, , \ L = L_n a$$

(3.26)

Substituting 3.25 and 3.26 into 3.24 gives:

$$v_p = \frac{\frac{\pi f_{nc}}{a} p_n a}{L_n a \sqrt{\left(\frac{\pi f_n}{a}\right)^2 - \left(\frac{\pi}{a}\right)^2} + \pi + 2\pi n}$$

(3.27)

Cancelling terms then gives:

$$v_p = \frac{f_n c p_n}{L_n \sqrt{f_n^2 - 1} + 1 + 2n}$$

(3.28)

Collating terms then gives:

$$v_p = \frac{k_1 f_n}{\sqrt{f_n^2 - 1} + k_2}$$

(3.29)

Where we have defined:

$$k_1 = \frac{c p_n}{L_n} , k_2 = \frac{1 + 2n}{L_n}$$

(3.30)

89

Differentiating 3.29 now gives:

$$v_p' = k_1 \frac{k_2\sqrt{f_n^2 - 1} - 1}{\sqrt{f_n^2 - 1}\left(k_2\sqrt{f_n^2 - 1}\right)^2} \tag{3.31}$$

Finally, setting $v_p' = 0$ and solving yields:

$$\sqrt{f_n^2 - 1} = \frac{L_n}{1 + 2n} \tag{3.32}$$

This key result indicates that higher harmonics require either a substantial increase in the path length or a reduction in the operating point. As the path length must be restricted so that the intersection between the forward and backward waves is sufficiently higher than the operating point (to avoid instability) then the only option is to reduce the operating frequency.

3.6 High-b Tube Design

A new tube design that uses the high-b operating condition can now be designed, in order to verify the analysis presented above. From the discussion of the link between the aspect ratio and the electron beam we know that the beam previously used for the Chapter 2 design could be reused here, giving an expected aspect ratio of 2.5:1 for the same operating point.

Due to the anticipated stability issues with a third harmonic design, it makes sense to first test the theory on a second harmonic (n = 1) tube. Because the range of ϕ_T is defined by the choice of harmonic ($3\pi < \phi_T < 4\pi$ when $n = 1$), the expected range of K_{pb} can be calculated as:

$$1.02 < K_{pb} < 1.36 \tag{3.33}$$

This result is within the bounds defined earlier ($1 < K_{pb} < 2$). Consequently, a tube running on these conditions is likely to be realisable, although the maximum beam tunnel could be restricted by the low value of K_{pb}. It is also advantageous (from a manufacturing perspective) to keep the width of the waveguide the same, leaving only the period (p) and straight (s) lengths to be defined.

The operating point was previously aligned with the turning point in the phase velocity curve in order to maximise bandwidth. However, previous analysis shows that the length s required would cause the

intersection of the backward and forward waves to be too close to the operating point. Therefore *s* is set to the minimum value that will allow the increased waveguide height to be evaluated and the operating point is chosen to equalise the phase and beam velocities.

Assuming *s* = 5, *p* can be chosen so that the phase velocity curve intersects the beam line at the desired operating point. Whilst calculations could be devised for *p*, as it is an independent parameter it is easier to manually tune it to intersect the beam line. Figure 3.9 shows a parameter sweep of *p* showing the effect on the phase velocity and demonstrating that a choice of $p = 10$ provides good alignment ($s = 5, a = 19$ and $v_{beam} = 0.18c$).
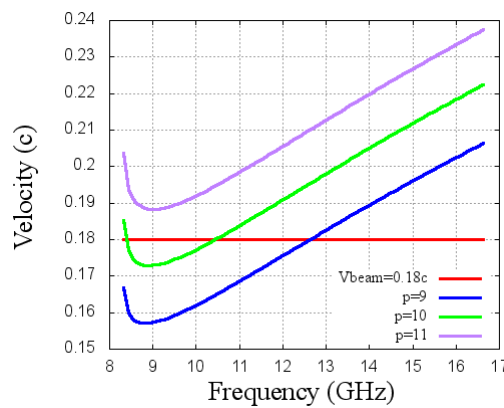
Figure 3.9 – Phase velocity of slow wave structure with a sweep of p (a = 18, s = 5, v_{beam} = 0.18c)

The final step before simulation is to calculate a value for *b*. We continue to use the same operating point as the design in chapter 2, although here the bandwidth should be reduced as the point of inflexion in the phase velocity curve has been lowered. Remembering that:

$$\beta_T = \frac{\omega_{op}}{v_{beam}}$$

(3.34)

And using the new operating condition:

$$\beta_T b = 9.208$$

(3.35)

We can obtain $b = 7.5\ mm$, which is less than the required value of 10 mm for the tube to be realisable. It should be noted that reducing the operating point will cause b to increase, thus reducing the ratio between *p* and *b* (K_{pb}) further, which is likely to cause problems with electric field coupling through

the beam tunnel. The final parameter set is given in Table 3.1. The dispersion plot for the final parameter set is given by Figure 3.10 and shows that the condition for stability given earlier [20] is met and the structure shows good synchronisation with the beam.

Table 3.1 – Parameters from analytical design for high-b tube.

Parameter	Value
Period (p)	10
Straight (s)	5
Waveguide width(a)	18
Waveguide height (b)	7.5
Beam velocity (v_{beam})	0.18c
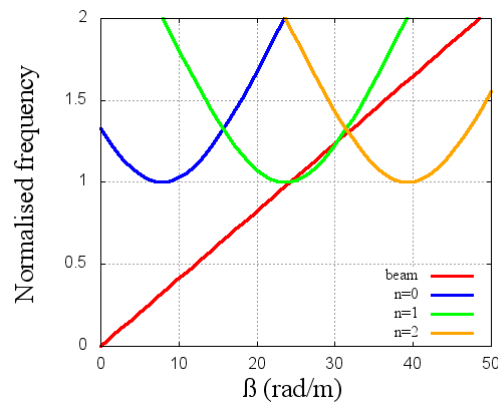
Figure 3.10 – Dispersion diagram for final parameter set.

3.6.1   Simulation results

We now present a full simulation for the final design. Figure 3.11 shows the port signals of a PIC solver run using the parameters in Table 3.1, with a small beam tunnel ($d_b = 2$ mm). As can be seen, there is noticeable gain between the terminals, suggesting that the final parameter set yields a full system that works as expected.
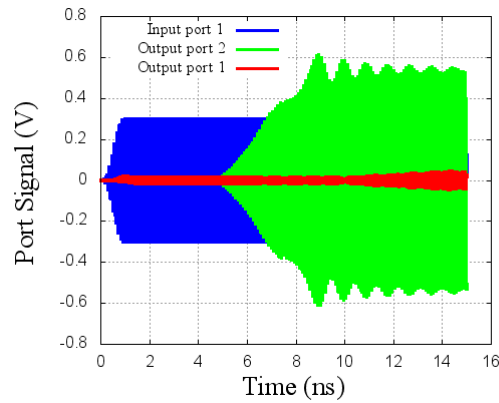
Figure 3.11 – Port signals from high-b tube.

Figure 3.12 shows the results of a parameter sweep of b against gain, whilst the beam tunnel and current are kept constant ($d_b = 2\ mm$, $I_0 = 0.3\ A$, $N_p = 40$). A high current was used to allow a lower number of periods thus reducing the simulation domain and the time required for the computation. As expected from the theory, as *b* is increased there is an initial peak followed by a null and then a smaller secondary peak. Due to the simulation settings (and some instability in in certain points on the sweep) the gain should only be considered to give an indication of the behaviour.
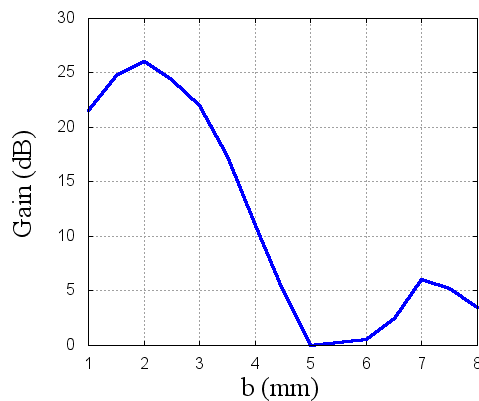
Figure 3.12 – Gain versus frequency for a sweep of the waveguide height (b).

The beam tunnel was then increased in size until the tube stopped operating, with a maximum diameter found at 5 mm (increased from 2mm). Therefore, assuming a constant current density this increase in beam tunnel diameter will allow the current to be increased by 6.25. To evaluate whether high-b operation was worthwhile, a comparison to the tube designed in Chapter 2 was made, although to avoid saturation effects the current in latter was reduced by 6.25. Figure 3.14 and Figure 3.13 shows a

comparison between the conventional geometry and the new high-b geometry. Figure 3.16 and Figure 3.15 show the port signals for the high-b design and Chapter 2 design respectively. From the figures we can see that the high-b design has a slightly reduced gain despite running at a higher current and a substantially reduced aspect ratio.
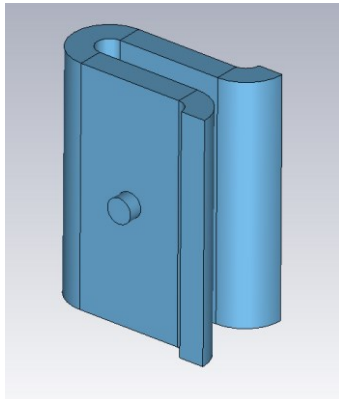
Figure 3.13 - Unit cell of serpentine using parameters from Chapter 2
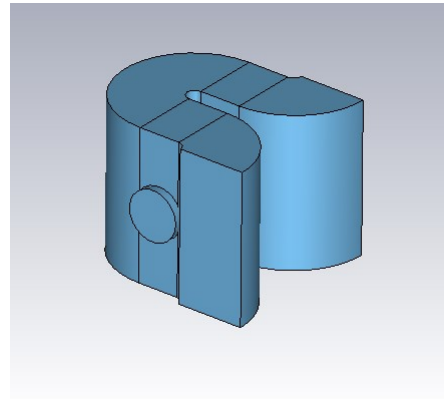
Figure 3.14 – Unit cell of serpentine using high-b parameter set calculated above
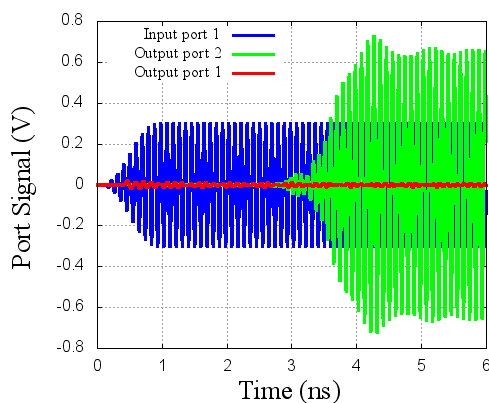
Figure 3.15 – Port signals for the tube designed in chapter 2 with a scaled current.
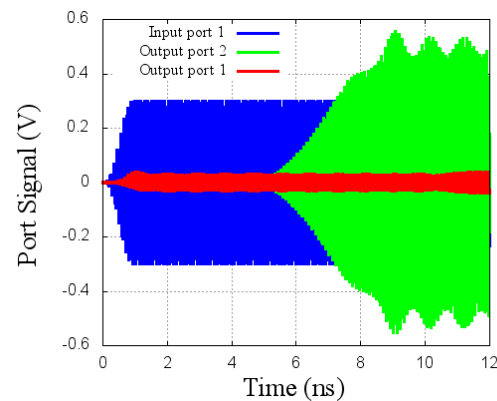
Figure 3.16 – Port signals for high-b tube with larger beam tunnel.

From the simulation results we can see that the tube is not operating as expected from the analysis as the reduction in gain is greater than expected, and the tube appears to be only partially stable and cannot operate with as large a beam tunnel as predicted. However the aspect ratio has been reduced and the beam tunnel diameter increased, which would allow higher frequency operation than the design in chapter 2 for a given electron beam width. Finally, it should be possible to increase the beam tunnel further in a new design that increased the ratio between *p* and *b* or compensated for the tunnel discontinuity.

3.7   Conclusions

The new tube has a lower aspect ratio and a significantly larger beam tunnel, thus allowing higher beam currents at the same density, although the actual beam coupling impedance is lower due to the use of the second transit angle maxima. Alternatively, a high-b design allows higher frequency operation than the conventional design for a given electron beam radius. Finally, increasing the waveguide height will also reduce the ohmic losses within the system as the attenuation constant of waveguide is proportional to its height [27] and input and output tapers are no longer needed.

The design has some problems with stability due to the reduced ratio between the operating point and the first intersection between the backward wave. It also suffers from a low ratio between b and p, which causes issues with electric field coupling through the beam tunnel, consequently limiting the maximum size of the beam tunnel. Finally it is an inherently narrowband design, as the operating frequency cannot be aligned with the point of inflexion of the phase velocity curve. However, all of these issues would not be present if this design were to be used as a backward wave oscillator, as the *b/p* ratio would be improved by the increase in operating frequency (the operating point would be moved to the first crossing of the backward wave) and an oscillator is by definition a narrowband design.

References

[1] S. Bhattacharjee, J. H. Booske, C. L. Kory, D. W. van der Weide, S. Limbach, S. Gallagher, J. D. Welter, M. R. Lopez, R. M. Gilgenbach, R. L. Ives, M. E. Read, R. Divan, and D. C. Mancini, "Folded waveguide traveling-wave tube sources for terahertz radiation" *IEEE Transactions on Plasma Science*, vol. 32, no. 3, pp. 1002-1014, June 2004.

[2] N. E. Lindenblad, "Electron discharge device system," U.S. Patent 2300052, 1942.

[3] R. Kompfner, "The traveling-wave tube as amplifier of microwaves," *Proc. IRE*, Vol.35, No. 2, pp. 124–127, Feb. 1947

[4] R. Luis, *A comprehensive review of travelling wave tube technology*, Defence Research Establishment Ottawa, Nov. 1979.

[5] C. K. Chong and W. L. Menninger, "Latest advancements in high-power millimeter-wave helix TWTs," *IEEE Transactions on Plasma Science*, vol. 38, no. 6, pp. 1227-1238, June 2010.

[6] H. J. Ha, S. S. Jung, and G. S. Park, "Theoretical study for folded waveguide traveling wave tube," *Int. J. Infrared Millim. Waves*, vol. 19, no. 9, pp. 1229–1245, Sep. 1998.

[7] R. L. Ives, "Microfabrication of high-frequency vacuum electron devices," *IEEE Trans. Plasma Sci.*, vol. 32, pt. 1, no. 3, pp. 1277–1291, Jun. 2004.

[8] G. Dohler, D. Gagne, D. Gallagher, and R. Moats, "Serpentine waveguide TWT*," IEDM Tech. Dig.*, pp. 485–488, Dec. 1987.

[9] G. L. Matthaei, L. Young, and E. M. T. Jones, *Microwave Filters, Impedance Matching Networks and Coupling Structures*. Norwood, MA: Artech House, 1980

[10] J. H. Bookse, M. C. Converse, C. Kory, C. T. Chevalier, D. A. Gallagher, K. E. Kreischer, V. O. Heinen, and S. Bhattacharjee, "Accurate parametric modeling of folded waveguide circuits for millimeter-wave traveling wave tubes*," IEEE Trans. Electron Devices*, vol. 52, no. 5, pp. 685–694, May 2005.

[11] Y. B. Gong, H. R. Yin, L. N. Yue, Z. G. Lu, Y. Y. Wei, J. J. Feng, Z. Y. Duan, and X. Xu, "A 140-GHz two-beam overmoded folded-waveguide traveling-wave tube," *IEEE Transactions on Plasma Science*, vol. 39, no. 3, pp. 847–851, Mar. 2011.

[12] Y. ShengMei, S. Wei, X. Ao and W. YaJun, "Analysis of higher order mode multi-beam folded waveguide TWT," *2015 IEEE International Vacuum Electronics Conference (IVEC)*, Beijing, 2015

[13] Kowalski, E.J., Shapiro, M.A., and Temkin, R.J., "An overmoded W-band coupled-cavity TWT," *IEEE Transactions on Electron Devices*, vol. 62, no.5, pp.1609-1616, May 2015.

[14] U. Rosenberg and M. Schneider, "High-performance transitions for overmoded operation of elliptical waveguides," *IEEE Transactions on Microwave Theory and Techniques*, vol. 48, no. 10, pp. 1749-1755, Oct 2000.

[15] M. K. Thumm and W. Kasparek, "Passive high-power microwave components," *IEEE Transactions on Plasma Science*, vol. 30, no. 3, pp. 755-786, Jun 2002.

[16] C. L. Kory, M. E. Read, R. L. Ives, J. H. Booske and P. Borchard, "Design of overmoded interaction circuit for 1-kW 95-GHz TWT*," IEEE Transactions on Electron Devices*, vol. 56, no. 5, pp. 713-720, May 2009.

[17] J. He, Y. Wei, Z. Lu, Y. Gong and W. Wang, "Investigation of a ridge-loaded folded-waveguide slow-wave system for the millimeter-wave traveling-wave tube," *IEEE Transactions on Plasma Science*, vol. 38, no. 7, pp. 1556-1562, July 2010.

[18] Y. Hou, Y. Gong, J. Xu, S. Wang, Y. Wei, L. Yue and J. Feng, "A novel ridge-vane-loaded folded-waveguide slow-wave structure for 0.22-THz traveling-wave tube," *IEEE Transactions on Electron Devices*, vol. 60, no. 3, pp. 1228-1235, March 2013.

[19] M. Liao, Y. Wei, Y. Gong, J. He, W. Wang and G. S. Park, "A rectangular groove-loaded folded waveguide for millimeter-wave traveling-wave tubes," *IEEE Transactions on Plasma Science*, vol. 38, no. 7, July 2010

[20]   K. T. Nguyen *et al.*, "Design methodology and experimental verification of serpentine/folded-waveguide TWTs," *IEEE Transactions on Electron Devices,* vol. 61, no. 6, pp. 1679-1686, 2014.

[21] M.H. Zhang , Y.Y. Wei , G. Guo , L.N. Yue , Y. Hou , S.M. Wang , J. Xu , Y.B. Gong and W.X. Wang "A novel 140-GHz sheet-beam folded-waveguide traveling-wave tube" *Journal of Electromagnetic Waves and Application*, Vol. 26 , Iss. 17-18, 2012

[22] M. A. Basten, J. H. Booske, J. R. Anderson, J. E. Scharer, "Formation and transport of sheet-electron beams and multibeam configurations for high-power microwave devices", *Proc. SPIE* 2557, pp. 262, Sep. 1995.

[23] D. E. Pershing et al., "Demonstration of a wideband 10-kW Ka-band sheet beam TWT amplifier", *IEEE Trans. Electron Devices*, vol. 61, no. 6, pp. 1637-1642, Jun. 2014.

[24] J. H. Booske, B. D. McVey, T. M. Antonsen, "Stability and confinement of nonrelativistic sheet electron beams with periodic cusped magnetic focusing", *J. Appl. Phys.*, vol. 73, no. 9, pp. 4140-4155, 1993.

[25] C. Liss, R. Harper, and M. P. Puri "Helical Waveguide Millimeter Wave TWT" *Technical Digest., International Electron Devices Meeting*, San Francisco, CA, USA, 1988, pp. 374-377.

[26] J. R. Pierce, *Traveling Wave Tubes*. New York, Van Nostrand, 1950

[27] N. Marcuvitz, *Waveguide Handbook*. McGraw-Hill, 1951.

4 Photonic Crystal Travelling Wave Tubes

4.1 Introduction

A photonic crystal (PC) is a structure with a periodic change in the material properties in 1, 2 or 3 dimensions. The utility in this form of construction is that the structure determines the propagation characteristics of waves within it. Therefore, through careful design, a variety of different properties can be found, which are not available in 'natural' dielectric materials. A property of particular interest is the existence of a bandgap within certain crystals, as waveguides, filters and other such circuits can then be formed within it by introducing defects in the periodic structure at specific points.

Whilst periodic dielectric structures have been investigated for some time, Lord Rayleigh described what is now commonly known as a Bragg mirror in 1887 [1] (again in more detail in 1917 [2] and Brillouin published a book on the subject in 1943 [3]). However, the term 'photonic crystal' was coined by Yablonovitch in 1987 [4]. Early work was conducted at microwave frequencies [5], before advances in micromachining allowed optical devices to be created [6]. A comprehensive review of current techniques and capabilities is given in [7].

As a photonic crystal allows control over propagation characteristics it can clearly be used for a slow wave structure. The major advantage of an all dielectric photonic crystal over a conventional structure is the elimination of metal losses, which become more significant at higher frequencies. The interest of photonic crystals for application in travelling wave tubes appears to have begun with Jasper in 1999 [8] where a photonic crystal was used to improve an existing TWT based on a printed circuit slow wave structure (developed as part of a US Army research program in the 1970s, which aimed to reduce the cost of TWTs using 'new' PCB technology). Only slightly later in 2002 Chen, Shapiro, Sirigiri and Temkin [9] describe a travelling wave tube using a fibre based photonic crystal as the slow wave structure. Figure 4.1 shows a photo of a prototype and a field plot from their patent application demonstrating the fibre photonic crystal style of slow wave structure. The same technique was further developed by Bailey et al. in 2006 [10], where the fibre structure and its inverse (holes within a dielectric block) are considered. Unfortunately, judging from comments in [11] in 2008 and [12] in 2016 it has

not yet been possible to fabricate the proposed design at the scale required for millimetre operation, the extreme aspect ratio required making the device particularly challenging. Other groups appear to have taken an interest in an all metal version [13] [14] [15] [16][17].
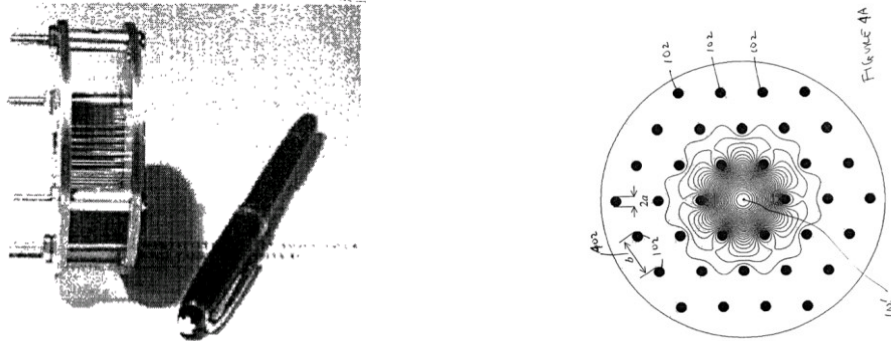
Figure 4.1 - Picture of Chen's device and field plot [9].

Work on 2D photonic crystals appears to have begun with [18] in 2002, although the subject is not referred to as a photonic crystal by the authors - it appears to be a slow wave structure formed from a metal rod array. A similar design is shown in significantly more detail by [19]. A rod based PC was also mentioned by Han [20] in 2005, with Vela [21] making a more detailed proposal in 2006. Figure 4.3 shows the structures proposed in [20] and [21].
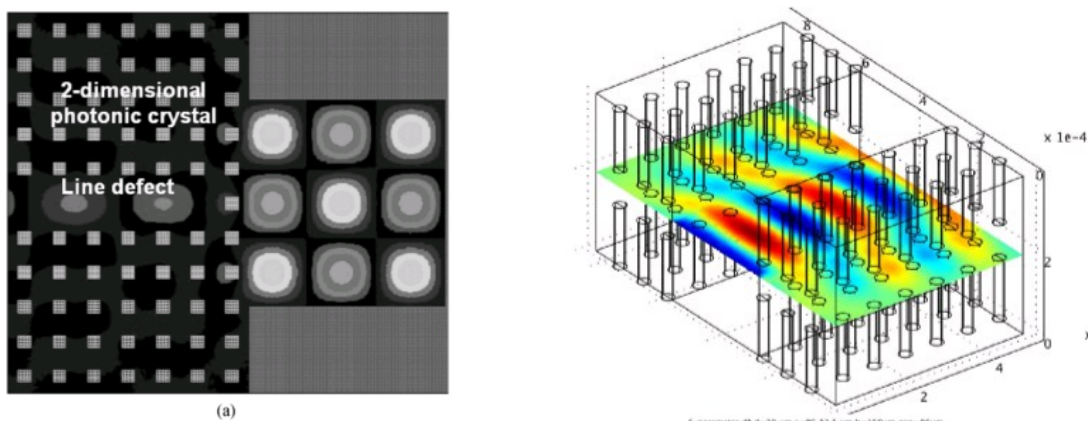
Figure 4.2 - Pictures from references Han and Vela [20][21]].

More recent approaches have often mixed 2D photonic crystals with an existing structure, producing a variety of interesting designs [22] [23] [24] [25]. Letizia[26] provides a short summary of the current state of the field and a more promising design, combining a 2D photonic crystal with a proven

corrugated waveguide slow wave structure. An alternative approach to a fibre TWT, shown in Figure 4.3, is to use what is sometimes referred to as 'Omniguide' [11] which was proposed as a slow wave structure by Smirnova in 2008 with positive experimental results following in 2012 [27]. A small review, covering both Omniguide and 2D lattices, was published in 2016 [28].
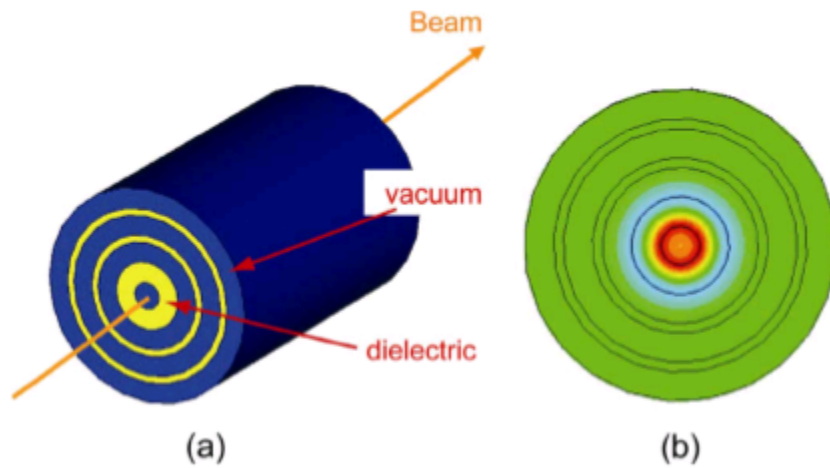
Figure 4.3 - Picture of Omniguide [11] showing a side view (a) and cross-sectional view of the longitudinal electric field (b).

4.2 Photonic Crystals

A rod-based structure introduces additional complexities due to its need for additional mechanical support. However, hole-based crystals are self-supporting. Consequently, only hole-based crystals are considered here. There are two main types of lattices, square and triangular. The latter was chosen for detailed consideration, as there was experience of this type of photonic crystal within the group [29]. The parameters for the crystal, such as hole size, lattice spacing and thickness were taken from this work, as similar crystals have previously been manufactured using Departmental facilities.

A well-established approach was taken to verify the parameter set for the photonic crystal [30]. First, an individual period with no defects was simulated using the eigenmode solver to see if a bandgap existed. Then (providing these initial results appeared promising) a complete crystal containing multiple periods was simulated using the frequency domain solver, both with and without a line defect, which acts to form a waveguide. If the parameters are suitably defined, waves should not propagate, leading to a very high reflection coefficient for the complete crystal. When the line defect is introduced, the reflection coefficient should drop, with a corresponding increase in the transmission coefficient, and the electric field should be confined inside the defect [7].

Figure 4.4 shows the physical arrangement for simulation, showing one period of the crystal with the boundary conditions displayed. A periodic boundary with a specific phase offset is used to study propagating modes and combined electric and magnetic field boundaries are used to suppress box modes within the overall simulation domain, as recommended by the solver instruction manual [30] . Table 4.1 shows the results of simulating the structure giving the mode frequencies of the photonic crystal for different phase offsets between the periodic boundaries calculated by the eigenmode solver. As the results from the solver indicate that there is a photonic bandgap a full crystal (both with and without a line defect) was simulated using the frequency solver in the normal way [31].
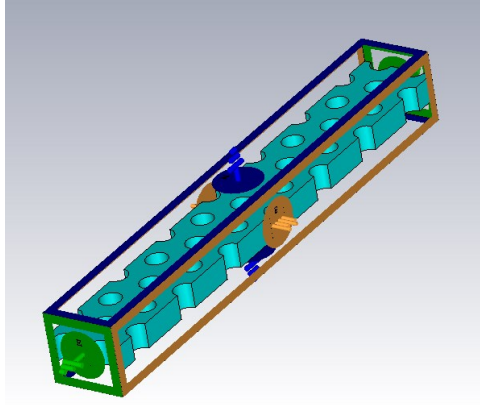
Figure 4.4 – One period of a photonic crystal showing the boundary conditions.

Table 4.1 – Mode frequencies for a single section of photonic crystal simulated using the eigenmode solver with periodic boundaries, with three phase shifts (0º, 90º, 180º) between the boundaries.

	0º	90º	180º
Mode 1	85.00 GHz	91.09 GHz	86.10 GHz
Mode 2	85.12 GHz	91.51 GHz	86.11 GHz
Mode 3	85.13 GHz	108.50 GHz	86.85 GHz
Mode 4	85.26 GHz	110.47 GHz	86.86 GHz
Mode 5	85.26 GHz	113.23 GHz	111.16 GHz
Mode 6	85.34 GHz	115.00 GHz	111.17 GHz
Mode 7	85.35 GHz	115.65 GHz	113.11 GHz
Mode 8	85.35 GHz	116.44 GHz	113.13 GHz
Mode 9	107.60 GHz	116.5 GHz	115.86 GHz
Mode 10	109.55 GHz	117.43 GHz	115.88 GHz

Figure 4.5 shows the layout of the crystal simulated. Normal waveguide ports are used to couple power into the structure, although additional metal has been added to reduce coupling between the ports from box modes within the cavity .The line defect is formed simply by filling the holes between the input and output ports, as shown in Figure 4.5b [32].
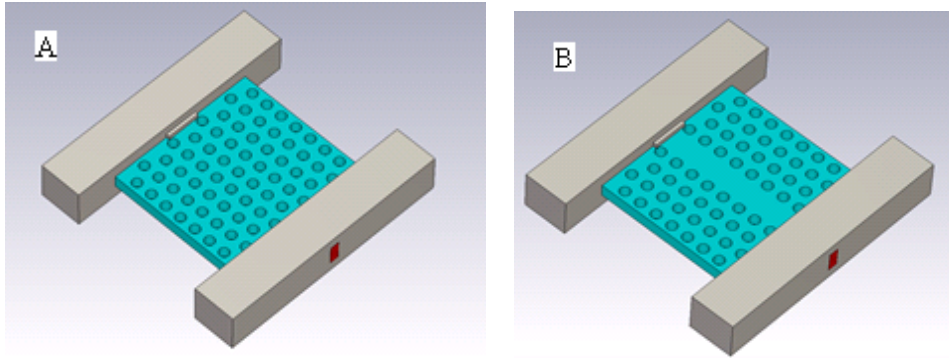
Figure 4.5 – Photonic crystal, a) with and b) without a line defect waveguide.

Figure 4.6 shows the frequency dependence of the S-parameters of the complete crystal, demonstrating that the crystal is reflecting all power over the frequency range indicated by the eigenmode solver. The reduction in return loss at 99.75 GHz is caused by the mode transducer leaking into the boundary, not a propagating mode (as the reduction is not matched by an equivalent increase in S21). This conclusion is strongly supported by Figure 4.7, which shows the magnitude of electric field on a log scale within the crystal at 99.75 GHz. Here a mode can be seen propagating along the edge of the crystal terminating in the simulation boundaries.
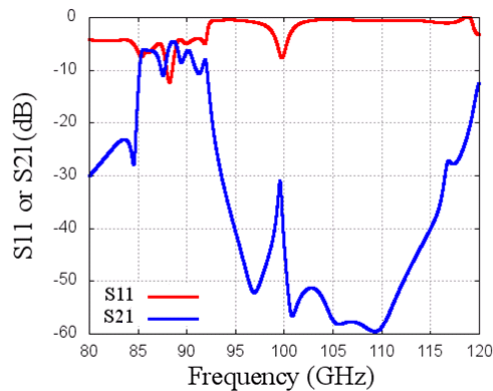
Figure 4.6 - Frequency dependence of S-parameters for a complete crystal.
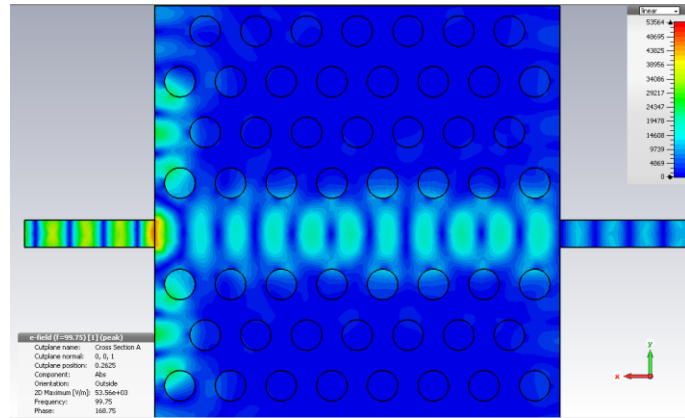
Figure 4.7 – Electric field magnitude of photonic crystal with line defect. Note that there is a significant amount of power propagating along the boundary due to a poor mode transducer.

Figure 4.8 shows the frequency dependence of S-parameters of the defected crystal. As shown by the plot, there is now no longer a bandgap although there are multiple pass and stop bands within the crystal due to the mismatch between the crystal and the mode transducers. These results demonstrate that the parameters produce a working photonic crystal into which defects can be added to change its propagation characteristics.

By introducing defects into the crystal many different types of waveguide can be made. However, in order for a photonic crystal to be used as a slow wave structure in a TWT, the electric field in the waveguide must be aligned with the electron beam.
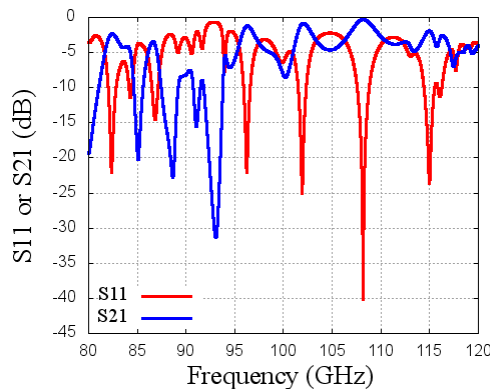
Figure 4.8 –Frequency dependence of S parameters for a crystal with a waveguide defect.

The first mode within a line defected waveguide is TE, and while it could certainly be possible to excite a higher TM mode, this approach would risk the usual problems with excessive losses from unintentional mode conversion. However, the periodic nature of the crystal lends itself well to a coupled

cavity structure, which could be operated at a higher harmonic, as discussed in the previous Chapter. A coupled cavity slow wave structure is a chain of cavities each containing a hole aligned to the electric field (so the electron beam can couple to the electric field within the cavity) and coupled to each other by a network with a phase shift that is not a whole number of multiples of π (so that forward and backward waves remain distinct). Within the field of photonic crystals this type of structure is usually referred to as a coupled-resonator optical waveguide (CROW)[33] and it has been studied extensively [34], including a significant amount of interest in its slow wave properties [35][36]. However, it appears that no one has investigated its suitability for use in a TWT.

A typical design flow is to first design a cavity with an electric field shape that couples well to the electron beam and then to consider the coupling network. However, with a photonic crystal, a separate coupling structure is unlikely to either be possible or needed. Unlike a metallic resonant cavity a photonic crystal cavity does not have well defined boundaries, so the cavity-cavity coupling is determined by the distance and orientation of the cavities to each other. However, whilst the cavity and coupling structure cannot be designed separately, it is worth studying isolated cavities first in order to understand the electric field patterns of their resonant modes.

4.3   Cavity Design

4.3.1 Point Cavity

All photonic crystal cavities are formed by introducing 'defects' into the crystal. The simplest affects only one element in the crystal and is known as a point cavity [38]. The typical approach in a hole-based photonic crystal is to change the radius of one of the holes, by enlarging, reducing or removing it completely. The best approach involves complete removal, as the other two styles of defect concentrate the field to an area that cannot contain any current. Figure 4.9 shows an example of a photonic crystal cavity formed from a point defect in this way.
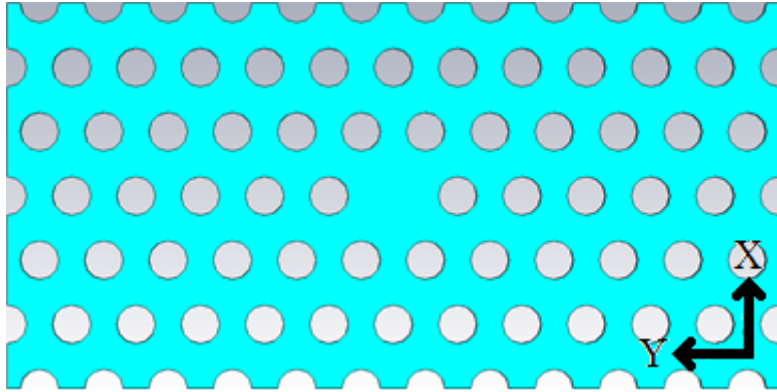
Figure 4.9 – Section of photonic crystal containing a point cavity.

In order to determine the suitability of such a defect for use in a coupled cavity slow wave structure the electromagnetic fields from the cavity were simulated using CST Microwave Studio, in the usual way [37]. Figure 4.10 shows a screenshot of the simulated electric field for the first cavity resonant mode and Figure 4.11 shows the second mode.
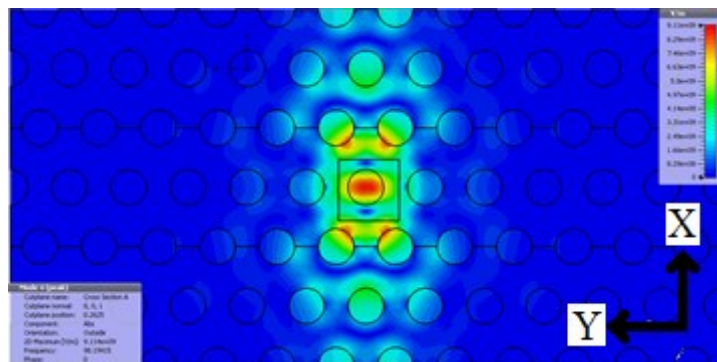
Figure 4.10 – Electric field magnitude, first mode point cavity.
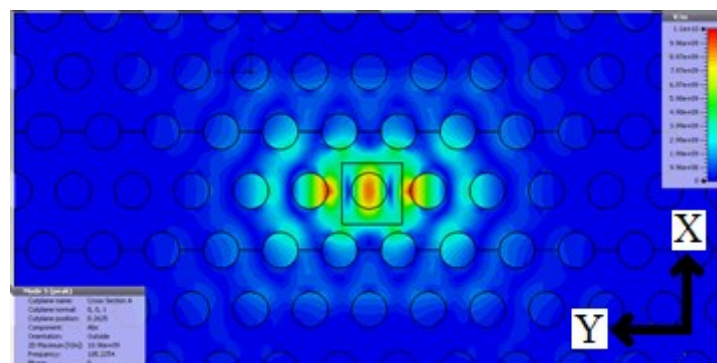
Figure 4.11 - Electric field magnitude, second mode point cavity.

Figure 4.12 and Figure 4.13 show the electric field strength of the X and Y components of the first mode, respectively. The components of the second mode are not shown, as it is simply a rotation of the first mode. The simulation results suggest that the point cavity has a suitable electric field for use in a coupled cavity TWT, as the major component of the electric field is parallel to the plane of the crystal. It should therefore be possible to arrange either a beam or drift current to propagate in the same direction, allowing a beam/wave interaction.
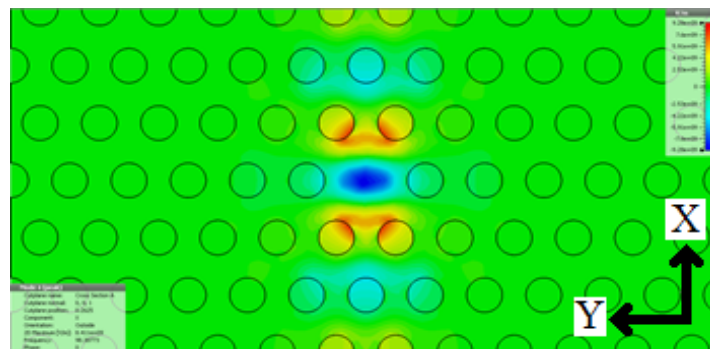
Figure 4.12 - X component of the electric field, point cavity first mode.
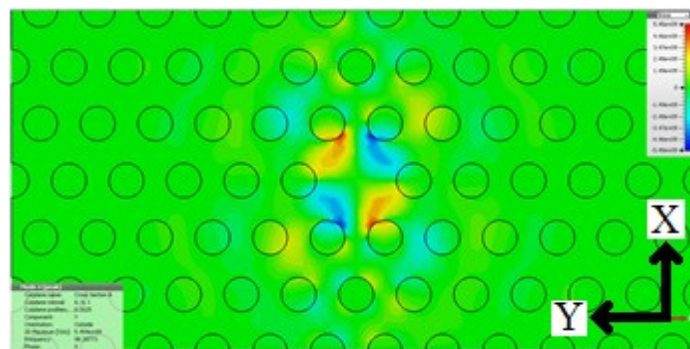
Figure 4.13- Y component of the electric field, point cavity first mode.

Whilst the cavity does have two modes, their electric fields are orthogonal to each other and their resonant frequencies are reasonably spaced. It could therefore be used to construct a single moded coupled cavity structure, but additional simulation work is needed as combining several cavities together is likely to change the resonant modes significantly. In addition, as shown in previous chapters, the gain is strongly linked to the strength of the beam coupling, which is in turn linked to the size of the interaction region. Therefore, if the size of the cavity could be increased further, the structure would have a stronger interaction with the beam, and a larger net terminal gain.

However, the properties of a perfect photonic crystal derive from an infinite lattice. Since such a lattice clearly cannot be simulated directly, it is important to determine whether the finite size of the simulated crystal is affecting the results. Further simulations were therefore carried out on a larger crystal to investigate the effect of size on the cavity resonant frequency. Arguably, this should remain unaltered, provided the electric field has decayed sufficiently at the crystal boundaries.

Figure 4.14 and Figure 4.15 show the magnitude of the electric field for the first and second modes of the same point cavity within a crystal containing an additional three periods. The mode frequencies have not changed and the electric field patterns look identical (despite the crystal increasing in size), so it is unlikely that the boundaries are affecting the simulation results. The technique of adaptively increasing the size of the crystal until the mode frequencies stabilised was used for all subsequent designs, although intermediate results will not be shown from now on.
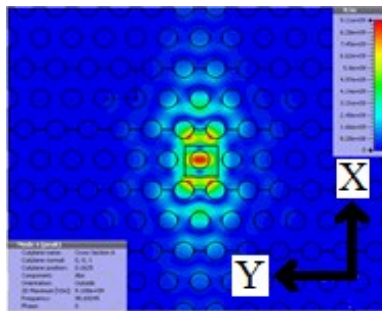
Figure 4.14 - Electric field magnitude, first mode, point cavity (larger crystal inside boundaries).
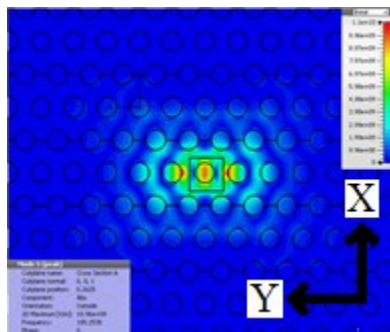
Figure 4.15 - Electric field magnitude, first mode, point cavity (larger crystal inside boundaries).

4.3.2 Line Cavity

We have previously presented arguments for a larger region of high electric field. Alternative cavity designs will therefore now be discussed. The line cavity is an obvious extension of the point cavity [39], with several adjacent sites within the lattice being defected instead of only one. As the crystal is a triangular lattice, there are three orientations for the line defect (although they are all identical electromagnetically, due to the rotational symmetry). Figure 4.16 shows a line cavity of length 3.
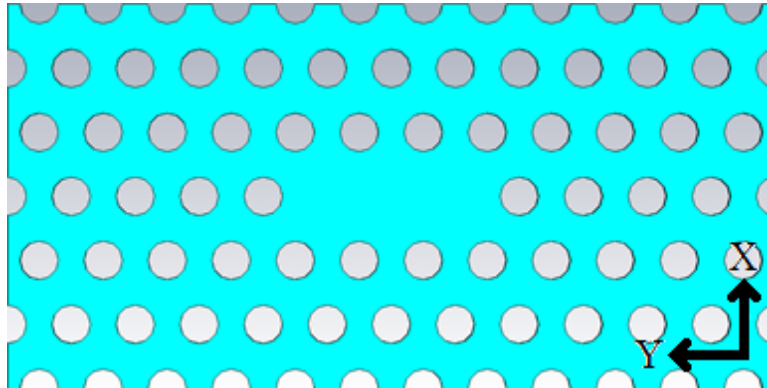
Figure 4.16 – Line cavity (length 3) within photonic crystal.

Figure 4.17 shows the electric fields of those resonant modes of the cavity that fall inside the frequency range of the crystal's bandgap (there are of course an infinite number of higher frequency modes). Only modes 2 and 5 have a strong electric field component in the Y plane direction; the others are either in the X direction (mode 1) or mixed (3 and 4). Whilst modes 2 and 5 could be used, the mode frequencies are unfortunately very close together. Multimode operation is therefore probably unavoidable; even if the mode transducer were sufficiently selective, mode conversion would almost certainly occur within the structure. Power coupling from the operating mode into any of the higher order modes is highly undesirable, as any power that cannot couple with the beam (if the system is designed for a beam in the Y direction then fields orthogonal to Y cannot interact) will appear as a significant loss component, negating the advantage of a low loss all-dielectric structure. Consequently it is unlikely that a line cavity could be used to make a single-moded coupled cavity structure.
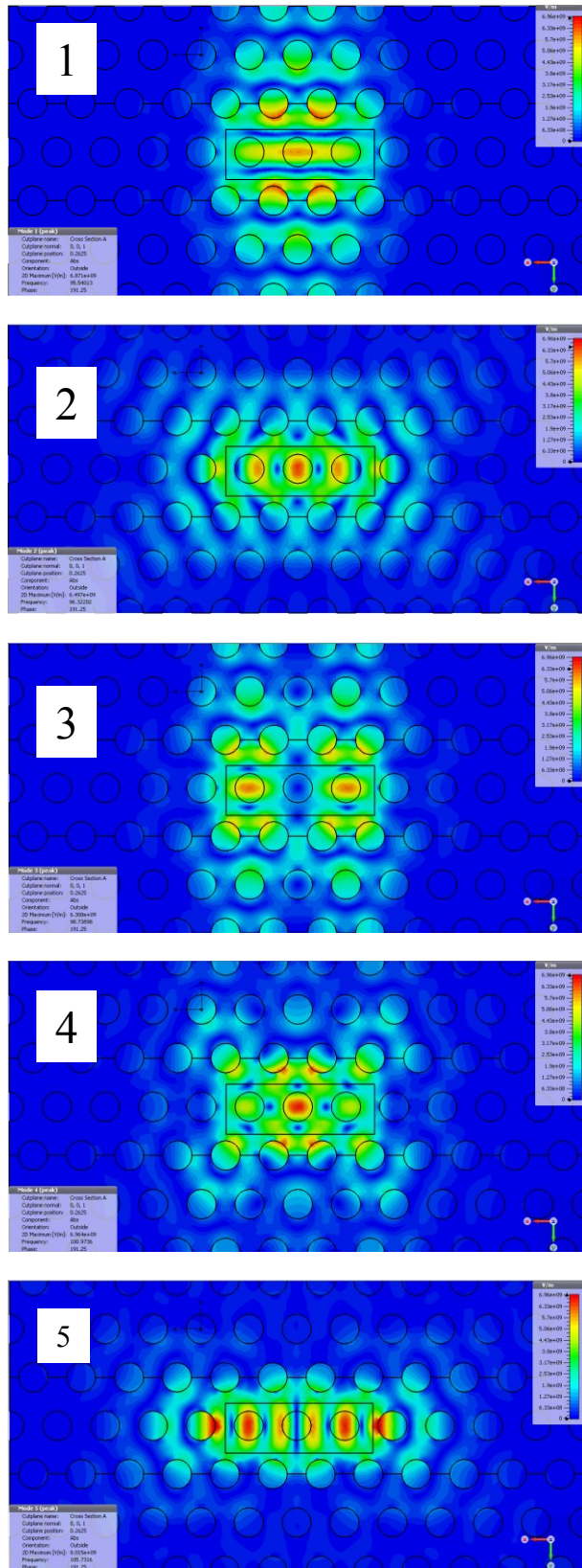
Figure 4.17 - Electric field magnitude of cavity modes within the photonic bandgap.

111

4.3.3 Chevron Cavity

Figure 4.18 shows the analogy of the line cavity along the other orientation within the crystal, which is called a chevron cavity here (although it is referred to by different names in the literature). Again the cavity can exist in multiple orientations, which are equivalent due to rotational symmetry.
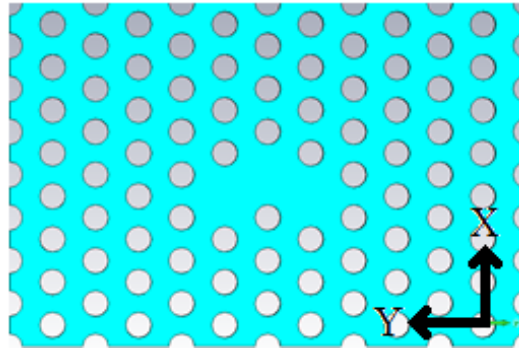
Figure 4.18 – Chevron cavity within a photonic crystal.

Figure 4.19 shows the resonant modes of the cavity that are within the frequency range of the bandgap. The chevron cavity's first mode is a significantly lower frequency (92.2 GHz) than the second mode (100.5 GHz) when compared to the line cavity (whose first and second modes are at 95.5 GHz and 96.3 GHz respectively). Therefore, it should be possible to minimise the likelihood of mode conversion or multimode operation. The first mode also has an ideal electric field for coupling to an electron beam (if the cavities are placed broadside in a line) as the field has a strong X component and is spread over a larger area than the point cavity, these attributes should maximise beam coupling. The second mode is unsuitable as its main field component is Y (perpendicular to the direction of propagation) so it will not couple to the beam. The higher modes present (3-6) are also unsuitable as they have a strong mix of X and Y components within the modes and so are likely to have lower interaction impedance. In addition, their mode frequencies are also quite close (all are within the range 100-103 GHz), so multimode operation is likely to occur.
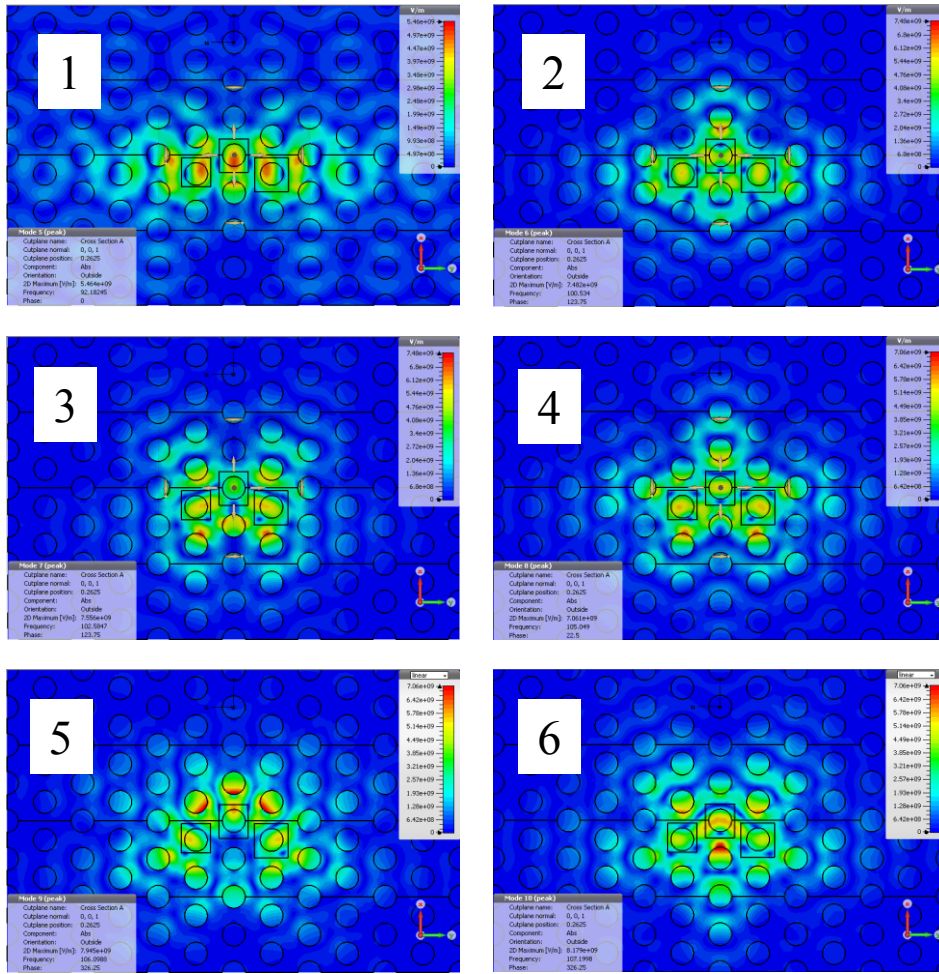
Figure 4.19 - Electric field magnitude of mode patterns for a chevron cavity within the photonic bandgap.(note holes enclosed by a box are filled)

4.3.4 Interim Conclusions

In conclusion, the lower of the two-point cavity modes appears to be more suitable than the second mode, as its resonant frequency is in the centre of the bandgap (unlike the second mode, which is at a higher frequency and thus towards the edge). The line cavity is probably not suitable for use in a coupled cavity slow wave structure as it has a large number of closely spaced modes, including a propagating TE mode. Finally, the chevron cavity shows some promise; while it supports many modes, the first mode has a suitable electric field and a significantly lower frequency than the higher order modes, so it should be possible to avoid multimode operation within a real structure. We shall now consider analogous properties of coupled cavity systems.

4.4   Coupled Photonic Crystal Cavities

Figure 4.20 shows an enlarged image of the X component of the electric field from the first mode of a point cavity. The resonance generates bands of positive and negative electric field which vary in phase and intensity across the crystal. Consequently, the strength and angle of the coupling between cavities will depend on their relative position [7]. It also seems reasonable to suggest that, as the mode pattern extends a significant distance from the defect, the coupling field will be defined across the entire extent of each cavity rather than just at the boundary (as in a traditional metal cavity based structure). Consequently, the coupled cavity behaviour will only be similar to individual cavities if the mode patterns have significant overlap. This implies that the cavities should be placed so that they do not attempt to force a field pattern on each other that is different to the 'natural' resonant mode.
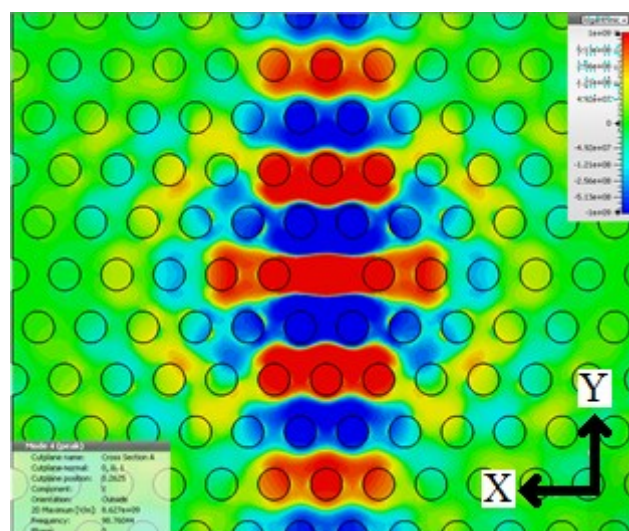
Figure 4.20 – Enlarged view of x component of electric field, point cavity, first mode (note axis rotated).

Several points can be therefore made about cavity positioning. The cavities should be positioned broadside-on, so that the electric field inside each cavity is parallel, either inline or with an offset. The phase shift between cavities will be position dependant, with both fundamental forward and backward wave devices possible. Also, cavities that produce a mode pattern that can tessellate should be preferred, as the coupled cavity structure is more likely to have performance similar to individual cavities. Conversely, if the mode patterns do not tessellate then when multiple cavities are coupled together, then the mode pattern must change. Finally, number of periods spacing between each cavity should be kept

to a minimum. While a larger spacing will lead to more amenable microwave behaviour, it unfortunately reduces the slow wave factor and the strength of the coupling with the electron beam (as there is minimal electric field in the space between cavities). Both are more important in a slow wave structure.

Because adjacent cavities must be close together and their fields must align to obtain strong coupling, the most obvious way to form a periodic arrangement of the cavity types previously discussed is broadside on, and in a straight line, as shown in Figure 4.21. Clearly the point cavity does not have a broadside direction. However, the mode excited in the coupled cavity case will depend on the relative orientation of the cavity line to the crystal axes. Consequently, the definition of 'broadside' should follow from the electric field of resonant modes, not the physical shape of the cavity.
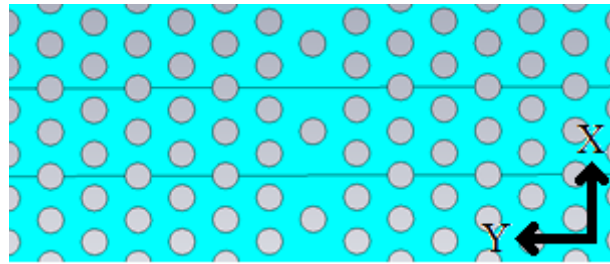
Figure 4.21 – Coupled point cavities forming a slow wave structure.

The most promising geometries and mode patterns identified from the study of isolated cavities (the first modes of the point and chevron cavities) were then simulated in a linear coupled arrangement to determine which ones might be suitable for use as a slow wave structure in a travelling wave tube. The simulation was set up in the way discussed at the start of the chapter, using the eigenmode solver with periodic boundaries to calculate the phase shift through the structure [30]. It should be noted that the solver is best set up with the periodic boundary intersecting the defect itself, rather than one of the spaces between.

4.4.1 Coupled Point Cavities

Figure 4.22 shows the X component of the electric field for the first mode with additional possible cavity locations annotated. From the diagram it appears that (as predicted) the coupling angle will vary drastically depending on the relative position of the cavities, as there is a clear phase inversion between some of the potential sites. In addition, the field strength is larger within an offset cavity site than the inline position, which could mean that an offset position has tighter coupling. However, no locations exist where the field pattern immediately surrounding a potential cavity site matches the field pattern around the defect. Therefore, a coupled cavity structure will have to have additional modes to those found in an isolated cavity, which could cause problems with multimode operation. Inline and offset cavity sites were therefore both investigated to determine whether a point defect could be used for a coupled cavity structure, with a specific attention paid to the dispersion characteristics and whether the structure was single moded or not.
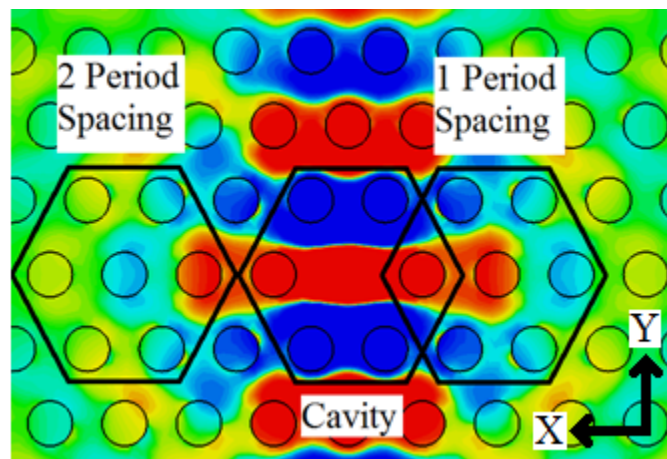
Figure 4.22 - X component of the electric field for the first mode with possible cavity locations labelled. (note axis rotated)

4.4.1.1 Single-period Spacing

The point cavity has two resonant modes that could potentially be used in a coupled system; the first mode is most suitable as the second mode frequency is close to the upper edge of the bandgap. Figure 4.21 (shown earlier) shows several periods of a coupled cavity structure made from point defects; note that only one period is simulated. Figure 4.24 shows the magnitude of the electric field for the first coupled cavity mode over a sweep of the phase from 0° to 150°. The simulation results demonstrate that the coupled system supports similar mode patterns to an isolated cavity; the electric field is concentrated within the defects regardless of the phase between the boundaries, and there is a phase offset between the fields in adjacent cavities as desired. Therefore, it is reasonable to conclude that the structure is behaving as a series of coupled cavities rather than a periodically defected waveguide when the first mode is excited.

Unfortunately, as shown in Figure 4.23, the coupled system has additional modes, including a TE waveguide mode that is a similar frequency to the coupled cavity mode. Consequently, a coupled system constructed from point cavities with a crystal spacing of one period is likely to suffer from multimode effects. However, the effect of the waveguide mode should be reduced if the spacing is increased from one period.
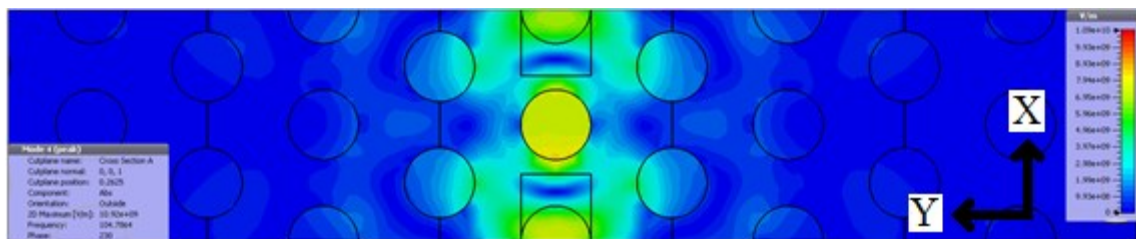
Figure 4.23 – Electric field magnitude, coupled point cavity, waveguide mode.
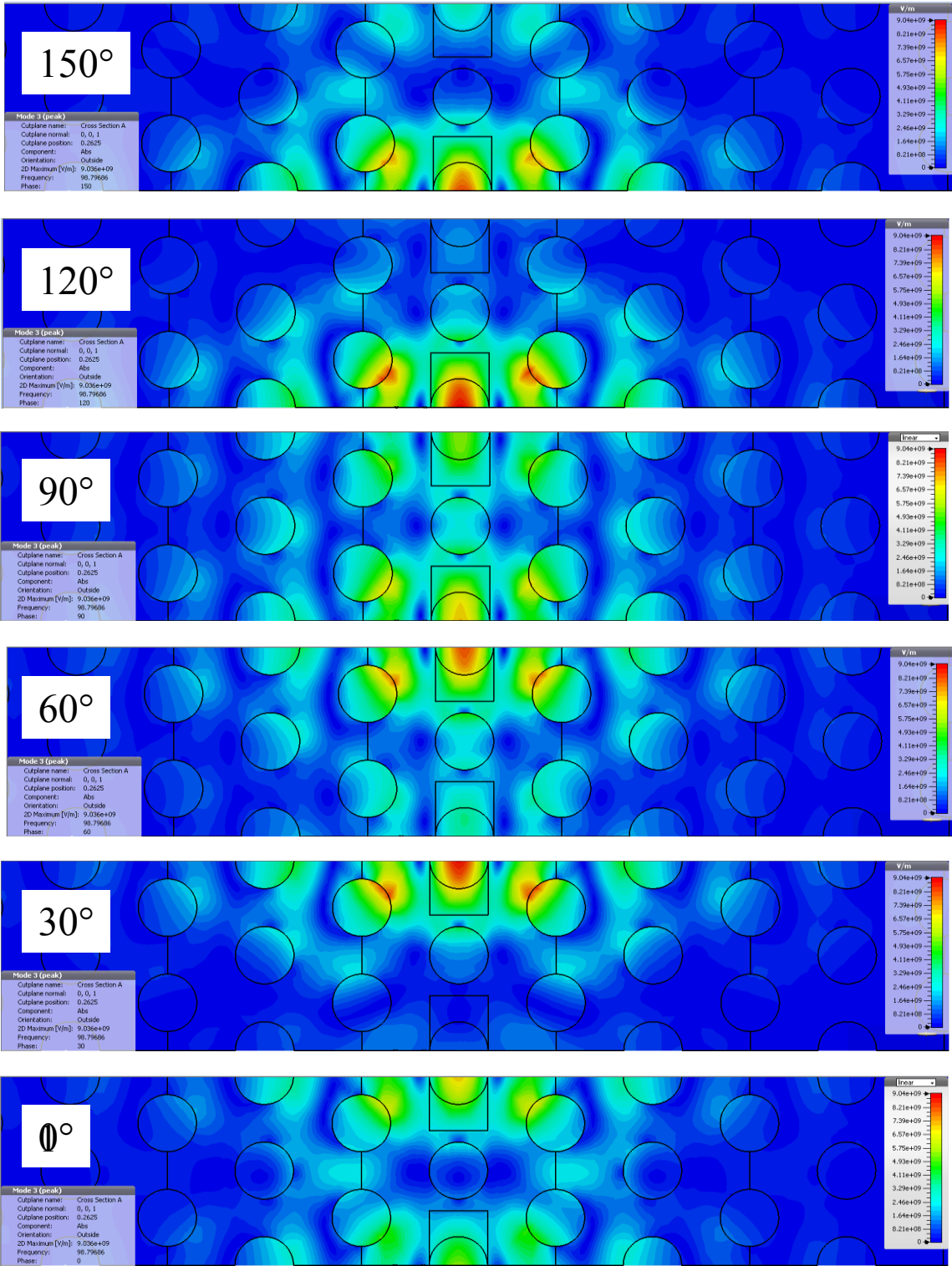
Figure 4.24 – Electric field magnitude from coupled point cavity, first mode, 0º to 150º phase.

4.4.1.2 Double-period Spacing

To overcome the problem highlighted above and to test the earlier speculation on the coupling phase being heavily influenced by position, a structure based on point cavities with a two-period spacing was investigated, as shown by Figure 4.25.
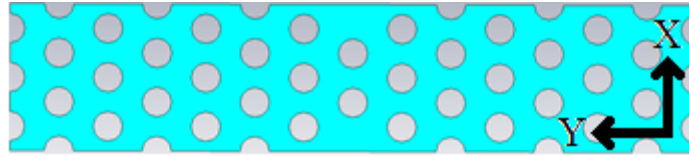
Figure 4.25 – One period of a coupled cavity structure formed of point cavities spaced two crystal periods apart.

Figure 4.27 shows the magnitude of the electric field for the first coupled cavity mode over a similar sweep in phase from 0º to 150º. Again, the mode pattern is similar to that of an isolated cavity and there is a phase shift between cavities. The waveguide mode cannot be shown, as it is either cut off or exists only at a frequency above the bandgap.

As the coupled cavity structure is now single-moded over the bandgap, the dispersion diagram can be plotted. Figure 4.26 shows the dispersion diagram for the first three spatial harmonics. The plot suggests that the structure is working correctly, as the dispersion curve has the typical shape of a fundamental backward wave coupled cavity structure, although the slow wave factor is rather poor (meaning that it would need to be operated on the second or third harmonic) and the operating bandwidth is rather small.
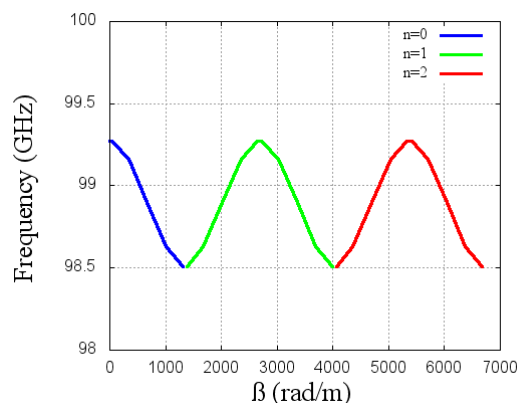
Figure 4.26 – Dispersion diagram for modes n = 0 to n = 2, for coupled point cavities with 2-period spacing.
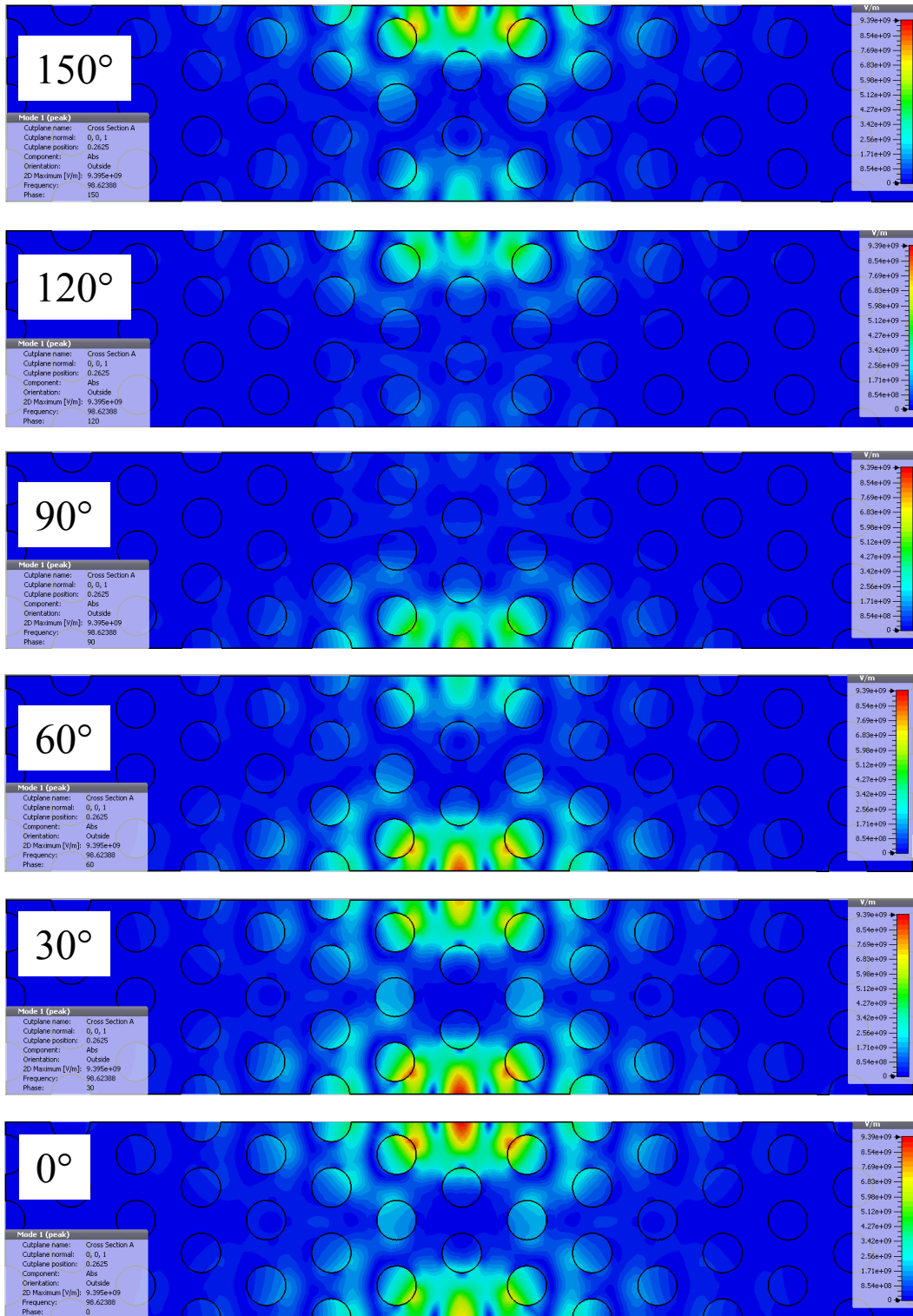
Figure 4.27 - Electric field magnitude from coupled point cavity, first mode, 0º to 150º phase.

4.4.1.3 Offset Cavities

Alternatively, the cavities can be placed with an offset to each other, as shown in Figure 4.28. The advantage of offset coupling is that the cavities are better aligned with the strong electric field emanating from the corners of the cavity [7]. The major disadvantage is that the structure can support multiple propagating modes (similar to odd and even modes) as the inline cavities are still coupled together.

Figure 4.28 – Photonic crystal containing offset point cavities.

Figure 4.29 shows the electric field from an alternating mode, where the offset cavity does not appear to affect the field significantly. Similarly, Figure 4.30 shows the electric field of the intended mode where all cavities are seen by the field. As multimode operation is a highly undesirable behaviour within a slow wave structure (it increases design complexity and has no associated benefit) the inline coupled structure is clearly preferable.

Figure 4.29 - Electric field strength for coupled point cavity, alternating coupled cavities.

Figure 4.30 – Electric field strength for coupled point cavity, all cavities coupled.

4.4.2 Coupled Chevron Cavities

We now consider similar effects coupled chevron cavities. Figure 4.31 shows the X component of the electric field for the first mode of an isolated chevron cavity, with potential additional cavity sites labelled. From the diagram it is clear that inline coupling with either a one or two period spacing is possible, although the angle of the coupling will be substantially different. The mode pattern from the chevron cavity also appears to be more suitable for a coupled cavity structure than the point cavity as the fringing field at the potential cavity sites has the same pattern as in the main cavity. Therefore further simulations were carried out to assess whether the chevron cavity could be used, and to identify the performance differences between the two possible cavity sites.
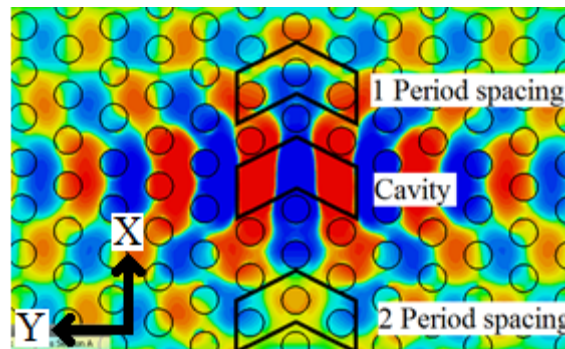
Figure 4.31 – X component of the electric field for the first mode of an isolated chevron cavity with potential coupled cavity sites annotated.

4.4.2.1 Single-period Spacing

Figure 4.32 shows the first mode of the coupled chevron cavity structure with a 90º periodic boundary condition (in the X direction) over a sweep of the displayed phase from 0º to 150º. The simulation results show that the coupled cavity mode has a similar electric field and resonant frequency to the same

mode in an isolated cavity. As expected there are a variety of higher order modes. However, as in the isolated cavity study, their resonant frequencies are sufficiently above the first mode that it should be possible to avoid multimode operation.
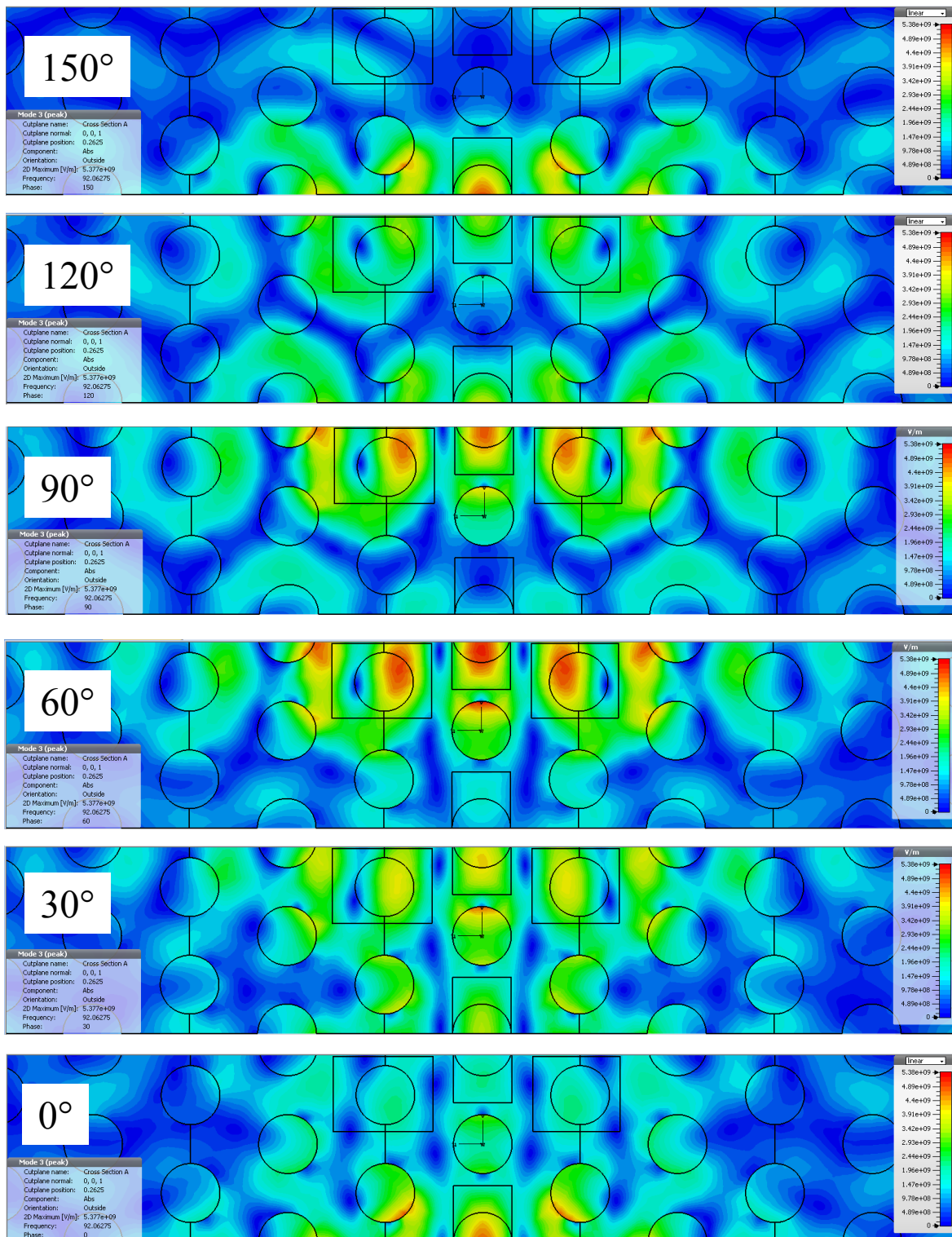
Figure 4.32- Electric field magnitude from coupled chevron cavity, first mode, 0° to 150° phase.

Figure 4.33, Figure 4.34 and Figure 4.35 show the second, third and fourth modes of the coupled chevron cavity structure respectively. The electric field is similar to the isolated chevron cavity in the third and fourth modes but the second mode is a new TE waveguide mode, broadly similar to the one in the case of a point cavity with single-period spacing. It should therefore be possible to suppress this waveguide mode in the same way as before, by increasing the separation distance. However, the frequency difference between the waveguide and coupled cavity modes is sufficiently large that the waveguide mode should be cut off in normal operation.
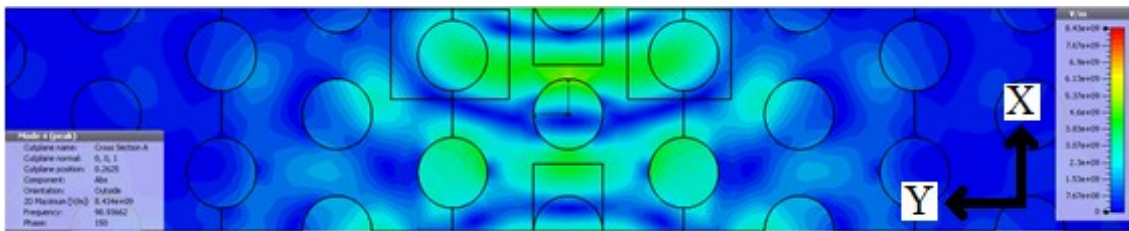
Figure 4.33 - Electric field magnitude from coupled chevron cavity, second (TE waveguide) mode.
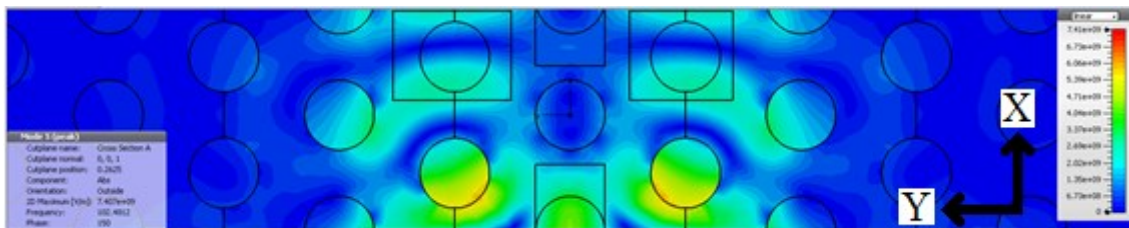
Figure 4.34 – Electric field magnitude from coupled chevron cavity, third mode.
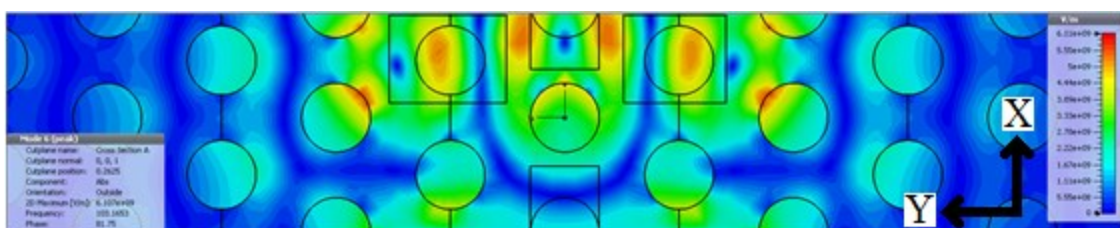
Figure 4.35 - Electric field magnitude from coupled chevron cavity, fourth mode.

Figure 4.36 shows the dispersion plot for the first three spatial harmonics, indicating that the structure is working normally and as a fundamental forward wave device. Compared to the dispersion diagram for the point cavities, the operating bandwidth is significantly larger and the slow wave factor is slightly

improved. Again the fundamental harmonic is superluminal so the device would need to be operated on the second or above harmonic.
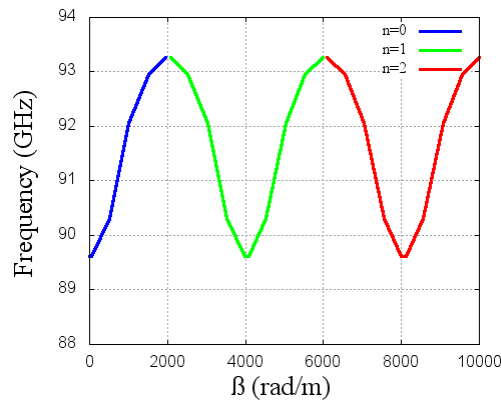
Figure 4.36 – Dispersion diagram for coupled chevron cavities, 1 period spacing (modes n=0 to n=2)

Figure 4.37 shows the mode pattern for the first coupled cavity mode within a significantly larger simulation domain, again with periodic boundaries. From the simulation results it is clear that the expected phase inversion between cavities is present and non πn as a sinusoidal field magnitude is present along the length of the structure, as would be expected within a coupled cavity structure. It should be noted that the mode pattern plotted was chosen to illustrate the point and is not a slow wave (in fact, it is superluminal). However, the spatial harmonics over n = 2 are subluminal, with an increasing slow wave factor.
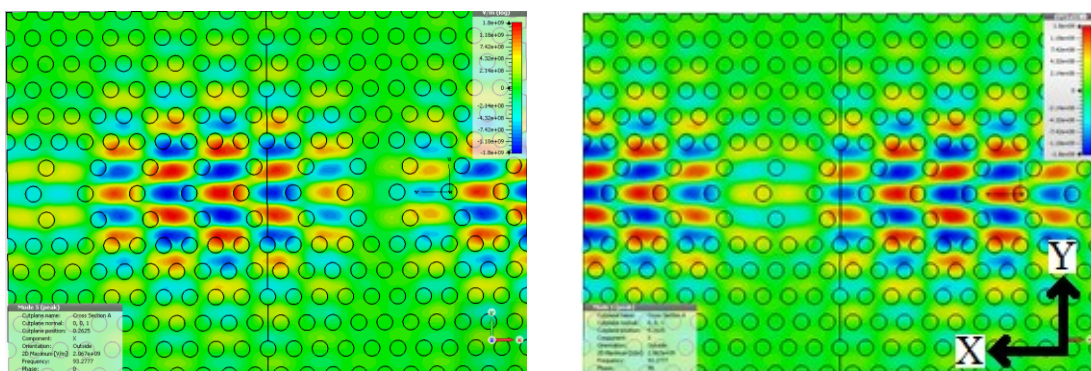
Figure 4.37– X component of the electric field for a coupled cavity mode, long wavelength. Phase 0º (LH) and 90º (RH).

4.4.2.2 Double-period Spacing

As mentioned previously, it is expected that the phase shift between 1- and 2-period spaced cavities will be inverted. Additional simulations were therefore performed on a 2-period spaced chevron cavity. Figure 4.38 shows the X component of the electric field for the coupled cavity mode of a series of coupled chevron cavities with a crystal spacing of 2 periods over a large crystal with a phase shift of 0 and 90 between the boundaries. As predicted, the phase shift between the cavities has been inverted by increasing the spacing to two crystal periods and the structure now has a sinusoidal electric field along the length of the coupled cavities. In addition it should also be noted that the waveguide mode seen with 1-period spacing has been shifted either above or below the simulation frequency range. The mode is definitely propagating because as the phase shift between the boundaries is swept the position of the peak moves.
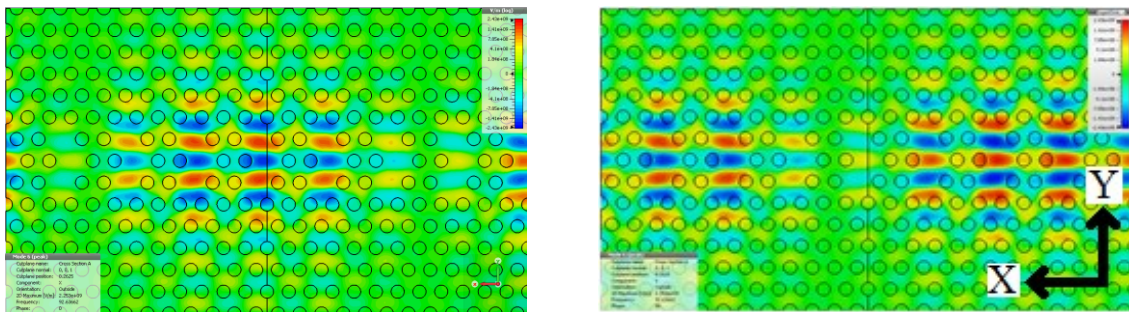
Figure 4.38 – X component electric field, coupled cavity mode, long wavelength. Phase 0º (LH) and 90º (RH)

Figure 4.39 shows the dispersion plot for the first three spatial harmonics and light line showing that the structure is now a fundamental backward wave device (to be expected with a change of 180º per period). Compared to the single period spaced structure the operating bandwidth has been reduced from around 3GHz to 1GHz and the slow wave factor decreased by a third (the latter is to be expected as one period of the structure is now 3 crystal periods rather than 2).
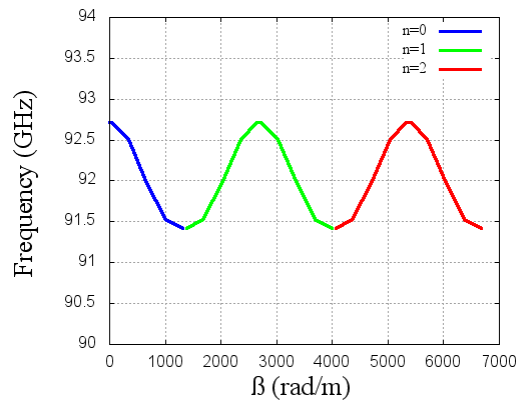
Figure 4.39 - Dispersion diagram for coupled chevron cavities, 2 period spacing (modes n=0 to n=2)

4.5 Beam coupling

Now that a coupled cavity structure with acceptable dispersion characteristics has been found, the next step is to consider whether the electric field it supports can be coupled to an electron beam. As mentioned at the start of the Chapter, a hole-based photonic crystal of a finite height does not (as with any dielectric-based microwave structure) confine the field entirely within the dielectric region.
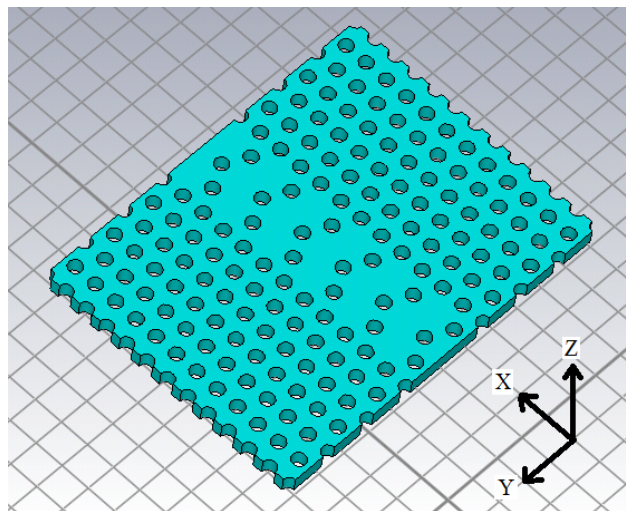
Figure 4.40 – Six period long section of the 1 period spaced chevron cavity crystal.

Figure 4.41 is a cross-section normal to the direction of propagation of the crystal showing the X component of the electric field. Here, as expected, there is a substantial amount of electric field outside of the dielectric region, so it should be possible to place the beam outside the crystal (in a similar way to [18] and [19]). This arrangement offers significant advantages over confinement of the beam inside a tunnel within the structure. In addition to mechanical and microwave advantages, the restriction on

the beam diameter is removed, breaking the link between beam diameter and operating frequency that exists in a serpentine structure. However, the beam must still intersect the electric field for a beam-wave interaction to be possible, with the integral of the electric field over the beam's cross-section determining the strength of the coupling. Close alignment of the beam and the surface is therefore necessary. However, this restriction could be lessened (or beam/wave coupling improved) by increasing the strength and extent of the fringing field.

Figure 4.41 – Cross-section of the slow wave with the electric field X component (normal to the page) displayed. Propagation direction is into the page.

Typically, 2D photonic crystals are designed to minimise the fringing field, so it is expected that with further effort it should be possible to increase the strength of the fringing field further. For example, Figure 42 shows a cross section of the X component of the electric field for a crystal with a notch cut along the direction of propagation. The removal of dielectric has caused the field maximum to shift towards the void causing the range and intensity of the fringing field to increase. A variety of other crystal parameters influence the fringing field, such as the height, dielectric constant, fill factor and period; unfortunately further optimisation of the parameter set could not be carried out due to time restrictions.

Figure 4.42 – Cross-section of a notched slow wave structure with the electric field X component (normal to the page) displayed. Propagation direction is into the page.

4.6 Conclusions

From these simulations we can see that a 2D hole-based photonic crystal with coupled chevron cavities has the two main properties needed for a slow wave structure: acceptable dispersion characteristics and electric field that can be aligned with an electron beam. The structure could also be highly suitable for high frequency operation as it utilises an all-dielectric construction (minimising ohmic losses) that is amenable for miniaturisation as it has a self-supporting structure and low aspect ratio. Similar structures have been demonstrated up to optical frequencies [7]. Finally, the fringing fields allow the electron beam to be placed outside the structure, consequently breaking the link between beam diameter and frequency and allowing sheet beams to be used. However before PIC simulations can be carried to verify that the structure can actually operate within a TWT, additional work is required design mode transducers with sufficient return loss and a well matched absorber that can be used to create a sever without causing a large reflection within the structure.

References

[1]Lord Rayleigh "On the maintenance of vibrations by forces of double frequency, and on the propagation of waves through a medium endowed with a periodic structure" *Philosophical Magazine* vol. 24 pp.145-159, 1887

[2]Lord Rayleigh "On the reflection of light from a regularly stratified medium" *Proc. Royal Society of London* vol. 93 pp. 565-577, 1917

[3] L. Brillouin *Wave Propagation in Periodic Structures,* McGraw–Hill, 1946

[4] E. Yablonovitch, "Inhibited spontaneous emission in solid-state physics and electronics", *Phys. Rev. Lett.*, vol. 58, no. 20, pp. 2059–2062, May 1987

[5] E. Özbay, "Layer-by-layer photonic crystals from microwave to far-infrared frequencies," *J. Opt. Soc. Am. B*, vol. 13, no. 9, 1945-1955, Aug. 1996.

[6]   T. F. Krauss, M. Richard, and S. Brand, "Two-dimensional photonic-bandgap structures operating at near-infrared wavelengths," *Nature,* vol. 383, no. 6602, p. 699, 1996.

[7] J. D. Joannopoulos, S. G. Johnson, J. N. Winn & R. D. Meade, *Photonic Crystals: Molding the Flow of Light,* Princeton University Press, 2nd edition, Princeton, 2008.

[8]   L. J. Jasper, "Traveling-wave tube with a slow-wave circuit on a photonic band gap crystal structures," US6664734, 16th December 2003

[9]   C. Chen, M. Shapiro, J. Sirigiri, and R. Temkin, "Vacuum electron device with a photonic bandgap structure and method of use thereof," US 6801107, 5th October 2004

[10] A. G. Bailey, E. I. Smirnova, L. M. Earley, B. E. Carlsten, and J. L. Maxwell. "Photonic band gap structures for millimeter-wave traveling wave tubes." *Proc. SPIE 6120. Terahertz and Gigahertz Electronics and Photonics,* 2006

[11]   E. I. Smirnova, B. E. Carlsten, and L. M. Earley, "Design, fabrication, and low-power tests of a W-band omniguide traveling-wave tube structure," *IEEE Transactions on Plasma Science*, vol. 36, no. 3, pp. 763-767, 2008.

[12]   E. I. Simakov et al., "Fabrication of ceramic structures for mm-wave traveling wave tubes," in *Vacuum Electronics Conference (IVEC),* 2016 IEEE International, 2016, pp. 1-2: IEEE.

[13]   J. S. Hummelt, S. M. Lewis, M. A. Shapiro, and R. J. Temkin, "Design of a volume mode W-band TWT amplifier," *Infrared, Millimeter, and Terahertz waves (IRMMW-THz),* 2014 39th International Conference on, 2014, pp. 1-2: IEEE.

[14]   G. Rosenzweig, J. S. Hummelt, M. A. Shapiro, and R. J. Temkin, "Designs of W-band TWT amplifiers with large beam tunnels," in *Vacuum Electronics Conference (IVEC), 2016 IEEE International*, 2016, pp. 1-2: IEEE.

[15] A. I. Nashed, S. K. Chaudhuri and S. Safavi-Naeini, "A cylindrical metallic photonic crystal waveguide – design and analysis," *2010 IEEE Antennas and Propagation Society International Symposium*, Toronto, ON, 2010, pp. 1-4.

[16]   A. Nashed, S. Chaudhuri, and S. Safavi-Naeini, "Analysis and design of a novel photonic crystal-based sub-mm/THz backward-wave oscillator," *IEEE Transactions on Terahertz Science and Technology,* vol. 2, no. 6, pp. 642-651, 2012.

[17]   A. I. Nashed, S. K. Chaudhuri, and S. Safavi-Naeini, "A 650-GHz backward wave oscillator based on axial loaded double defected-photonic crystal SWS," *IEEE Transactions on Plasma Science,* vol. 45, no. 3, pp. 372-380, 2017.

[18] L. Ives *et al.*, "Development of backward-wave oscillators for terahertz applications," in *Proceedings of SPIE*, 2003, vol. 5070, pp. 71-82.

[19]   R. Villeneuve, M. Cueille, D. Arnaud-Cormos, J.-F. David, P. Leveque, and A.-J. Durand, "Setup and characterization of a backward wave oscillator delay line scaled down to centimeter-and millimeter-wave ranges," *IEEE Transactions on Terahertz Science and Technology*, vol. 5, no. 6, pp. 1053-1061, 2015.

[20]   S.-T. Han et al., "Experimental investigations on miniaturized high-frequency vacuum electron devices," *IEEE Transactions on Plasma Science*, vol. 33, no. 2, pp. 679-684, 2005.

[21]   G. Vela, M. Miller, R. Grow, and J. Baird, "Terahertz backward-wave oscillators with photonic crystal waveguides," in *Vacuum Electronics Conference, 2006 held Jointly with 2006 IEEE International Vacuum Electron Source*s., IEEE International, 2006, pp. 425-426: IEEE.

[22]   G.-S. Park and J.-K. So, "THz microfabricated vacuum electronic devices using photonic concepts " presented at the *35th International Conference on Infrared, Millimeter, and Terahertz Waves*, Rome, 2010.

[23] Y. Gong et al., "Study of traveling wave tube with folded-waveguide circuit shielded by photonic crystals," *IEEE Transactions on Electron Devices*, vol. 57, no. 5, pp. 1137-1145, 2010.

[24]   E. Tahanian and G. Dadashzadeh, "A novel gap-groove folded-waveguide slow-wave structure for G-band traveling-wave tube," *IEEE Transactions on Electron Devices*, vol. 63, no. 7, pp. 2912-2918, 2016.

[25]   Y. Hai-Rong et al., "A method of designing photonic crystal grating slow-wave circuit for ribbon–beam microwave travelling wave amplifiers," *Chinese Physics*, vol. 16, no. 9, p. 2737, 2007.

[26]   R. Letizia, M. Mineo, and C. Paoloni, "Photonic crystal-structures for THz vacuum electron devices," *IEEE Transactions on Electron Devices*, vol. 62, no. 1, pp. 178-183, 2015.

[27]   D. Y. Shchegolkov, W. B. Haynes, R. M. Renneke, and E. I. Simakov, "Millimeter-wave gain experiments with a wide-band omniguide traveling-wave tube," in *Vacuum Electronics Conference (IVEC),* 2012 IEEE Thirteenth International, 2012, pp. 297-298: IEEE.

[28]   E. N. Odarenko and A. A. Shmat'ko, "Photonic crystal and Bragg waveguides for THz electron devices," in Laser and Fiber-Optical Networks Modeling (LFNM), *2016 IEEE 13th International Conference on*, 2016, pp. 53-55: IEEE.

[29]   W. J. Otter, S. M. Hanham, N. M. Ridler, G. Marino, N. Klein, and S. Lucyszyn, "100 GHz ultra-high Q-factor photonic crystal resonators," *Sensors and Actuators A: Physical,* vol. 217, pp. 151-159, 2014.

[30]   *Nanophotonics and Integrated Optics - Photonic Crystal Cavities*. Available: https://www.cst.com/solutions/article/nanophotonics-and-integrated-optics-photonic-crystal-cavities

[31]   *Photonic Crystal Simulation*. Available: https://www.cst.com/solutions/article/photonic-crystal-simulation

[32]   A. Chutinan and S. Noda, "Waveguides and waveguide bends in two-dimensional photonic crystal slabs," *Physical Review B,* vol. 62, no. 7, p. 4488, 2000.

[33]   A. Yariv, Y. Xu, R. K. Lee, and A. Scherer, "Coupled-resonator optical waveguide:? a proposal and analysis," *Optics Letters,* vol. 24, no. 11, pp. 711-713, 1999.

[34]   H. Altug and J. Vučković, "Two-dimensional coupled photonic crystal resonator arrays," *Applied Physics Letters,* vol. 84, no. 2, pp. 161-163, 2004.

[35]   J. K. Poon, J. Scheuer, Y. Xu, and A. Yariv, "Designing coupled-resonator optical waveguide delay lines," *JOSA B,* vol. 21, no. 9, pp. 1665-1673, 2004.

[36]   J. Scheuer, G. T. Paloczi, J. K. Poon, and A. Yariv, "Coupled resonator optical waveguides: toward the slowing and storage of light," *Optics and Photonics News,* vol. 16, no. 2, pp. 36-40, 2005.

[37]   *Simulation   of   Photonic   Crystal   Cavities*.   Available: https://www.cst.com/solutions/article/simulation-of-photonic-crystal-cavities

[38]   O. Painter, J. Vuckovic, and A. Scherer, "Defect modes of a two-dimensional photonic crystal in an optically thin dielectric slab," *JOSA B* vol. 16, no. 2, pp. 275-285 , 1999

[39]   Y. Akahane, T. Asano, B.-S. Song, and S. Noda, "High-Q photonic nanocavity in a two-dimensional photonic crystal," *Nature,* vol. 425, no. 6961, pp. 944-947, 2003.

5   Electron Gun Design

A travelling wave tube (TWT) consists of two main parts, an electron gun and a slow wave structure. Therefore, in order to experimentally confirm the theoretical study in Chapter 3 an electron beam system must be designed and fabricated in addition to the slow wave structure. Whilst the attempt to build a fully operational travelling wave tube was unsuccessful this chapter details the design and mechanical work conducted.

From earlier analysis in Chapter 2 we know that for a given slow wave structure to operate as desired it requires an electron beam of a certain velocity and current. In addition, the beam must physically fit in the beam tunnel within the slow wave structure. Accordingly, the method of generating a suitable electron beam must be explored and analysed such that its limits are known: there is little point in designing a slow wave structure for a beam that is impossible realise, or that would require an enormous magnetic field to remain collimated.

Figure 5.1 shows a diagram of a travelling wave tube with the electron beam, electron gun, collector and focussing magnet labelled. Within the electron gun, the cathode is the source of electrons, which are produced through thermionic emission. The electrons are then accelerated and focussed by a shaped electrostatic field, which is generated between the cathode and anode using a large bias voltage [1]. The focusing magnet (either a periodic permanent magnet or a solenoid) provides a magnetic field that generates a Lorentz force on the electron beam to counteract the space charge force of the electrons, thus keeping them collimated [2]. Finally, the collector stops the beam and either recycles or dissipates its energy. Typically, in a production system a depressed collector is used, which allows some energy from the beam to be recovered [3]; however, in a lab setup the collector is simply a cooled metal block that intercepts the beam.
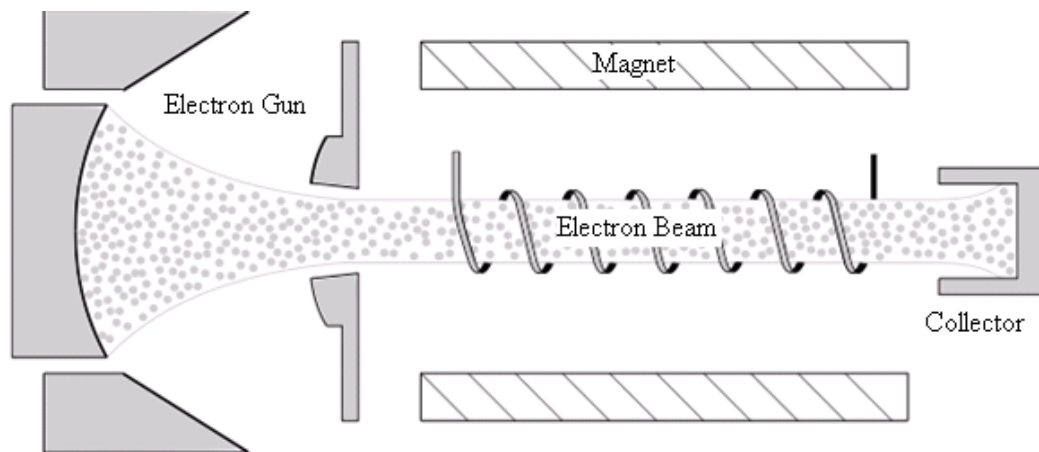
Figure 5.1 - Labelled diagram of a travelling wave tube.

Normally these elements are not considered individually, but in groups based on the design challenges involved. The groups are as follows: the focussing electrodes are combined with the cathode to form an electron gun, although the thermionic emission of the cathode can be considered separately. The magnet is broken into two parts. Firstly, how the beam interacts with the magnetic field whilst it is being focussed - commonly called the magnetic insertion [4] - and secondly how the beam behaves once it is focussed, often called the drift tube. Finally, the collector is considered on its own.

Whilst the grouping of the apparatus is chosen to minimise the amount of interaction (from a design point of view) between groups, some remains, which causes limits on the 'design freedom' of each part. Whilst these restrictions are explained in more detail in their relevant subsections it is useful to list them here, as they are referred to throughout this Chapter. The main aspects are:

- The strength of the magnet determines the maximum beam current density
- The required beam current density is determined by the size of the beam tunnel and required current (from the slow wave structure)
- The accelerating voltage and beam current are determined by the slow wave structure. These factors determine the perveance of the electron gun, but only a certain range of perveance is possible.
- The emissivity of the cathode determines its size and thus the amount of focussing needed within the gun
- The level of space charge limitation on the electron emission of the cathode determines the temperature uniformity required.
- The slow wave structure must fit within the magnet.

135

5.1 Electrodes

5.1.1 Introduction

As mentioned earlier, the electrodes in combination with the cathode form a structure known as an electron gun. Electron guns have several different topologies. The first to generate a rectilinear electron flow, despite the effects of space charge, is known as a Pierce gun after its inventor at Bell Laboratories [5].

Figure 5.2 shows a Pierce gun with the anode, cathode, ground plane, aperture and focal point labelled. From the figure it can be seen that the gun is essentially a pair of shaped electrodes with a large bias voltage applied between the two. This voltage creates a strong electrostatic field whose focusing performance is determined by the geometry of the anode, cathode and inclined ground plane. The cathode is designed such that it emits electrons (ideally perpendicular to its surface) and then the electrostatic field is used to accelerate electrons away from the cathode towards the anode, which contains an opening. Once the electrons pass through this opening they are no longer under the influence of the electrostatic field, and are only affected by the space charge forces within the beam and the collimating magnet (not shown here). Since the collimating magnet can counteract the space charge forces but not provide any additional focussing (the reasons for this will be given in the section on magnets), the beam diameter at this point is maintained throughout the tube.
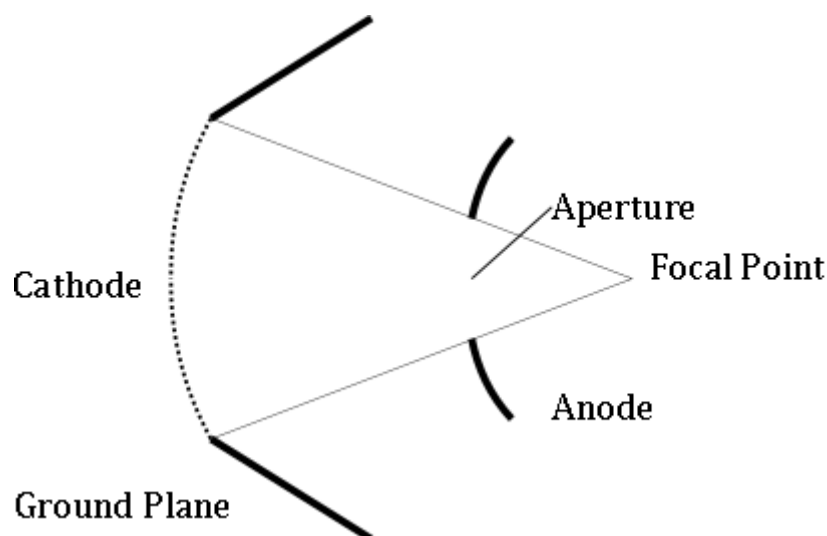
Figure 5.2 - Simplified drawing of a Pierce gun.

136

Of course, it is desired to know the dimensions of the electrodes for a given specification, which is usually for a beam of a given diameter and current. There are two main design challenges: that the electron beam diverges due to space charge forces [6] and that the current density within the beam is greater than the emission density of the cathode. These issues lead to the conclusions that there must be some sort of focusing, as the cathode area must be larger than the beam area, and that the focussing must be much stronger than would be expected from ray tracing optics, as it must overcome the diverging force caused by the space charge. A solution to these problems is provided by Pierce [5] and further expanded by Vaughn [7]. This solution can be rewritten as a simple iterative design process as given by [8] and is used in the next section.

5.1.2   Analysis

The basis for obtaining the parameters for a simple Pierce gun is to use optical ray tracing and then make a correction for the effects of space charge. These two steps form a simple iterative procedure that gives a good starting point for further CAD simulations which allow increased optimisation of the design. Figure 5.3 shows a sketch of the electron gun geometry with the main parameters: cathode radius (R_c), anode radius (R_a), tunnel opening width (b_0), beam minimum (b_m), ground planes, and emitter width (r_c) labelled.
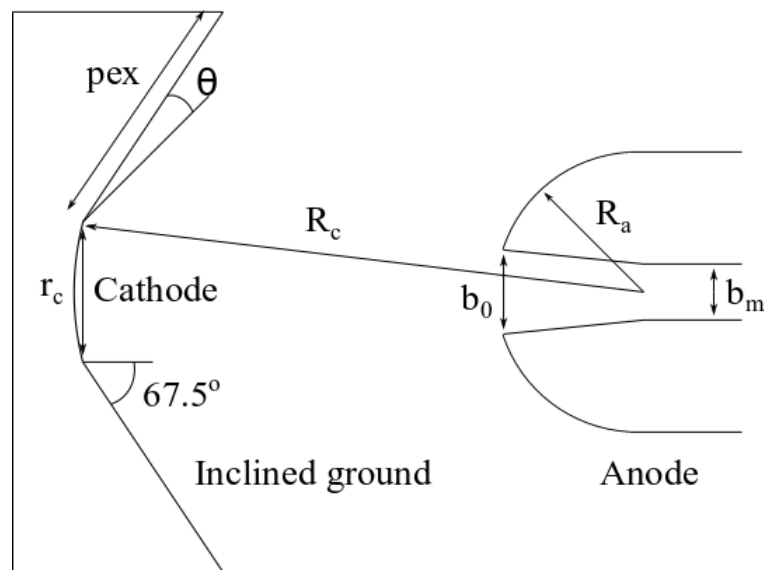
Figure 5.3 – Labelled sketch of the typical geometry of a Pierce gun.

The analysis in [5], [7] and [8] calculates the electrode radii for a given beam waist, accelerating voltage, beam current and cathode emissivity. Therefore, a significant part of electron gun design involves choosing sensible values for these such that the design can be fabricated.

Based on the earlier discussion on system design, a beam waist, current and voltage have been chosen that are believed to be achievable, leaving only the cathode emissivity to be decided. Whilst discussed in greater detail later (see section 5.2.3 on cathode design) emissivities from 0.01 A/cm^2 to 0.1 A/cm^2 were thought to be most practical, with the lower end of the range preferred for the following reasons:

Typical emissivities for commercially available cathodes range from around 0.1 A/cm^2 to 1 A/cm^2 [9]; therefore the low end of the range should be a safe maximum for a prototype device.

It is likely that the tungsten being used in a commercial cathode is of higher purity than used here. The emissivity of tungsten (as with all materials) can be significantly reduced by the presence of certain trace materials [10].

The gun will be operating in the space charge limited emission region (following the Child-Langmuir Law [11][12]) so the cathode's emissivity needs to be equal to or greater than that specified over its entire operating surface. As the emissivity is strongly linked to the operating temperature [13][14][15], variations in temperature across the cathode could prevent normal operation if they are too large. However, as the emissivity is simply required to be greater than the design value, then a lower value will allow larger temperature variations before affecting operation.

The cathode will be operating under space charge limited emission, so the beam current can be increased by increasing the voltage or by adjusting the space between the electrodes (to a point). Therefore, the design value should include some additional tolerance to allow the current to be tuned.

However, it should be noted that as the cathode becomes larger, the assembly's sensitivity to manufacturing tolerances increases because the solid angle occupied by the cathode also increases. Therefore an initial of 0.01 A/cm^2 was chosen for an initial exploratory design, with the maximum safe value (using this cathode material) of around 0.05 A/cm^2.

5.1.3 Simulation

There are a variety of techniques and computer-aided design (CAD) packages that can be used to simulate electron guns, including CST Particle Studio. This CAD tool combines electrostatic, magnetostatic and particle tracking solvers, which allow it to calculate the trajectories of charged particles inside electrostatic and magnetostatic fields generated from arbitrary electrodes and coils. It also supports a variety of particle emission models, including space charge limited emission.

Figure 5.4 shows a typical output of the solver: a 3D electron trajectory. The main parts of the electron gun (the cathode, anode and drift region) are labelled. The collimating magnet is not shown, although the pole plate is labelled. The electron beam originates on the left-hand side (at a defined emission surface) and is focussed by the electrodes. The focussed beam continues in the drift region (where it should have a constant cross section) before striking the simulation boundary and terminating. The drift area is not needed in a production design; it is included here purely so that the quality of the electron beam produced from the gun can be studied. The pole plate on the right-hand side is also not needed in a production system; it is again included here so that the magnetic field is not affected by the boundary conditions.
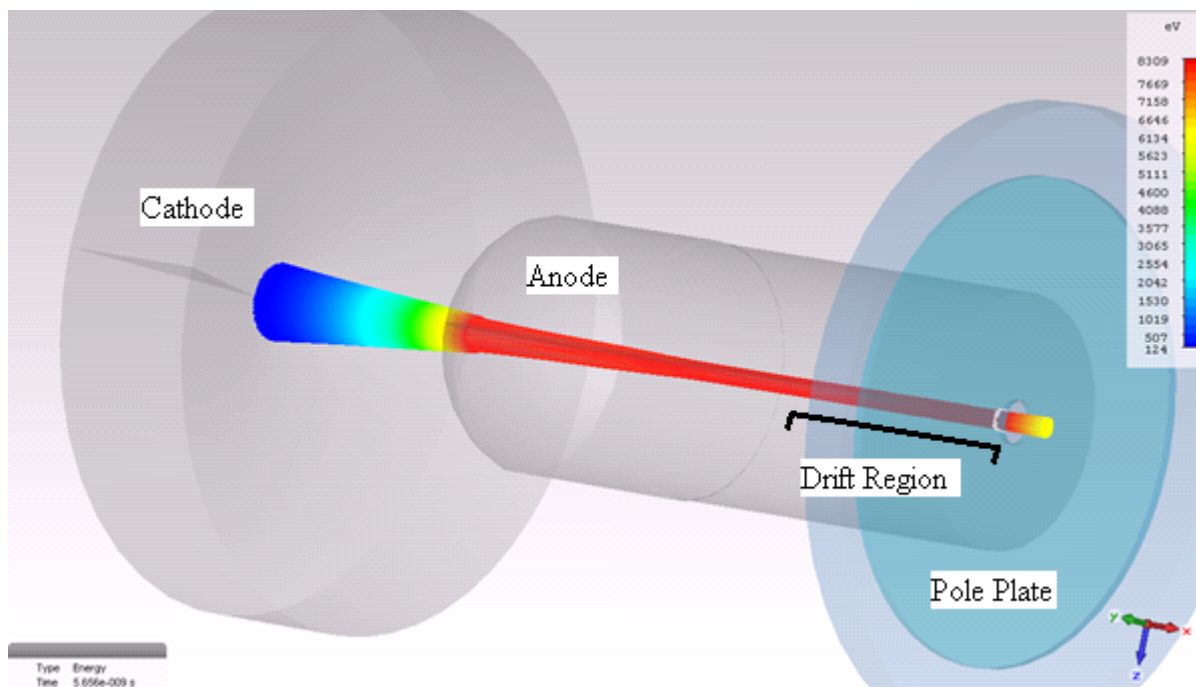
Figure 5.4 - 3D Electron trajectory simulated in CST Particle Studio.

5.1.4 Design

Table 5.1 shows the parameters required for the electron beam used for the slow wave structure designed in Chapter 2. Whilst the goal was originally to build the tube investigated Chapter 3 it was considered to be wise to prove the electron gun on a well-known design first.

Table 5.1 – Desired electron gun performance.

Parameter	Symbol	Value	Unit
Normalised Velocity	v_{beam}	0.18c	
Current	I_0	25	mA
Beam radius	r_b	1	mm
Cathode Emissivity	ε_e	0.01	A/cm^2
Perveance	P	0.0662	

The Pierce gun is extremely well known, and Vaughn [7] describes an iterative technique for calculating its geometry. This solution is also presented as a worked design example in [8], which has been used here to calculate an initial set of parameters as shown in Table 5.2.

Table 5.2 – Gun geometry from analysis.

Parameter	Symbol	Value	Unit
Anode Radius	R_a	32.56	mm
Cathode Radius	R_c	91.81	mm
Beam waist	b_m	1	mm
Axial cathode radius	r_c	8.92	mm
Cathode Angle	θ	5.57	°
Voltage	V_0	8.2	kV

Figure 5.5 shows the variation of beam radius with distance in a simulation of a Pierce electron gun with the parameters listed in Table 2. The electron beam starts at the left-hand side and initially has the same radius as the emitter. As it travels towards the anode, the beam is focussed and reduces in radius. At 0.06 m axial distance there is a sudden reduction in the beam radius, as the outer part of the beam strikes the anode. The inner part of the beam continues, although it is again clipped at 0.12 m. The beam then reaches a minimum radius of 2 mm at 0.015 m, before it begins expanding under the effects of

space charge. This value is significantly larger than the design radius. However, since the beam is inside a tunnel, the diverging electrons eventually strike the tunnel wall itself, limiting the maximum radius.
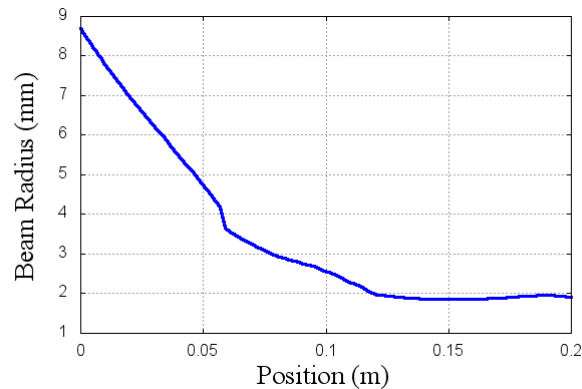
Figure 5.5 - Beam profile of simulated electron gun using the parameter set in Table 2.

From the simulation, it is clear that the geometry requires further tuning in order to meet the specification. However before tuning the gun it is worth determining whether any changes can be made to the geometry that would improve manufacturability. As the structure is fairly simple, the most obvious change is to approximate the curved cathode using a flat disc. Considering the parameters presented in Table 2 this change is quite likely to be possible as, due to the perveance of the gun, the cathode angle (θ) is sufficiently small that a small angle approximation should not result in significant error.

Figure 5.6 shows a comparison between the variation between beam radius and position for flat and round cathodes for an electron gun geometry with the parameters in Table 2. The focussing power of the gun is clearly reduced by the change to flat electrodes, resulting in a wider electron beam and significantly more collision with the anode. Whilst the rate of change of beam radius has clearly been reduced near the cathode, between 0.02 m and 0.06 m both cathode styles show a similar rate of change in beam radius against distance. This indicates that the flat cathode has only affected the shape of the focussing field near the cathode, with the majority of the electric field remaining similar.
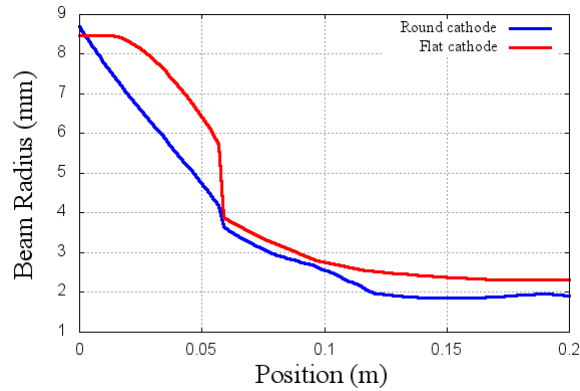
Figure 5.6 - Comparison between the beam profiles obtained with round and flat cathodes.

Figure 5.7a and b show close-up views of the electric field around round and flat cathodes respectively with iso-potential lines drawn. Both plots have a very similar shape and spacing of isolines on the right-hand side of the plot. However, on the left hand side, near the cathode, there is a significant difference, with the field from the flat cathode having a significantly straighter shape than that from the round cathode. As the electron beam will be roughly perpendicular to the isolines we can say that a reduction in the curvature of the iso-potentials within the electric field will result in a decrease in focussing power. Since the effect is quite small, it should be possible to compensate for it by increasing the power of focus from the electrostatic field by changing the electrode geometry.
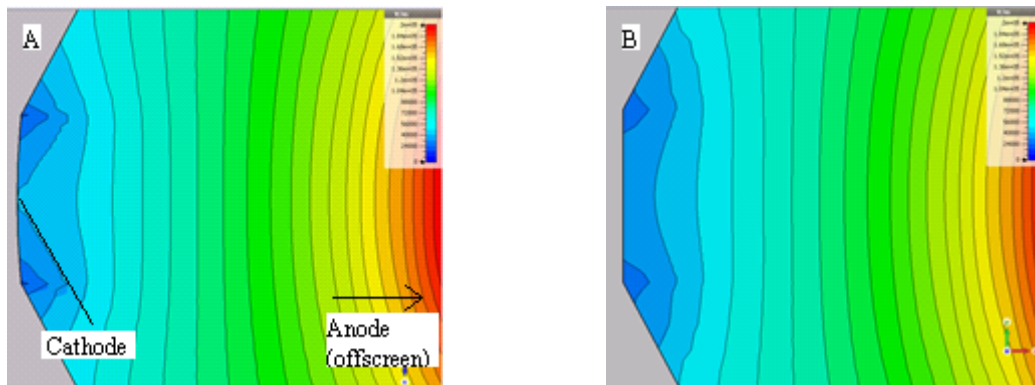
Figure 5.7 Electric fields near a) round, and b) flat cathodes

Whilst the focussing power of the electrostatic field is controlled by the shape of the electrodes, attempting to tune them individually is unlikely to be successful as the gun parameters are heavily interlinked [7]. Consequently, it is better to redo the earlier analytical design with a smaller target beam

waist, which will require a higher focusing power. The parameter set obtained after carrying out this iterative design is shown in Table 5.3 .

Table 5.3 – Revised parameter set for a gun geometry with a reduced target beam waist.

Parameter	Symbol	Value	Unit
Anode Radius	R_a	32.56	mm
Cathode Radius	R_c	91.81	mm
Beam waist	b_m	0.05	mm
Axial cathode radius	r_c	8.92	mm
Cathode Angle	θ	5.57	°

Figure 5.8 shows the effect of the new parameters on the electron beam radius. As can be seen from the figure the electrostatic focussing power has been increased: the gradient of the beam is steeper for the new parameter set. However, there is still significant interception of the beam by the anode, which is undesirable as it wastes emitted current from the cathode and heats the anode, which as it is in a vacuum will be awkward to cool.
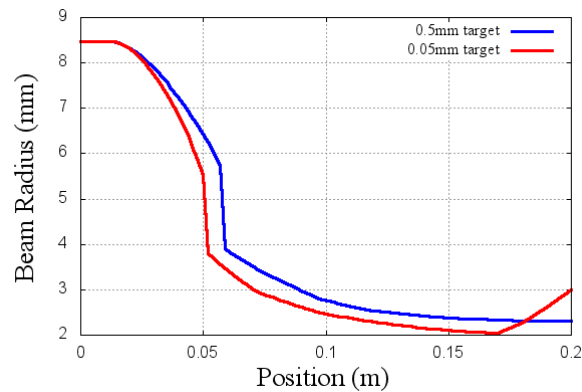
Figure 5.8 – Beam profile of the previous 0.5 mm target beam waist electron gun compared to a 0.05 mm target waist.

One method of reducing the amount of interception would be to increase the size of the aperture in the anode. However, as the aperture increases, the amount of field that penetrates into the anode will also increase, causing the electric field to distort and the beam to defocus. An alternative way of reducing the amount of interception, without increasing the aperture, is simply to reduce the axial cathode area.

This not only reduces the ratio between the axial cathode radius and target beam radius but also reduces the current. A reduction in beam current also means a reduction in the debunching forces from space charge, so the beam will require less focusing power.

Figure 5.9 shows the effect of sweeping the axial cathode radius from 5 mm to 9 mm on the beam waist. The effect on beam waist cannot be seen for the initial reduction in axial cathode radius (from 9 mm to 8 mm) as there is still significant interception by the anode. From 7 mm onwards, the outside of the electron beam passes through the anode with minimal interception, although there is still a slight kink in the beam profile caused by the distortion in electric field around the aperture. The severe kink in the traces for 5 and 6 mm radius is due to an effect similar to spherical aberration (detuning the gun has caused different parts of the beam to have different focal points). Considering the results from 7 mm to 5 mm we can clearly see that there is a non-linear relationship between the beam waist and the axial cathode radius. Before a judgment can be made on a suitable axial cathode radius, the corresponding effect of beam current therefore needs to be studied.
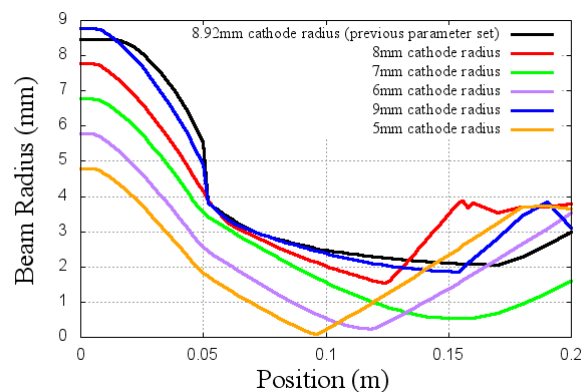
Figure 5.9 – Beam profile against position over a sweep of the cathode radius from 9 mm to 5 mm.

Figure 5.10 shows the effect of decreasing the cathode radius on the beam current which (as expected) decreases consistently as the cathode radius is reduced- the beam current is roughly in proportion to the cathode area as expected. Figure 5.11 shows the effect of reducing the cathode radius on the required cathode emissivity. Surprisingly, the required emissivity of the cathode also reduces as the cathode radius is decreased.

Considering both sets of results, while a 7 mm axial cathode radius gives an acceptable beam waist and nearly the specified current it has little tuning room, which is highly desirable in an experimental design. As beam waist can be traded for current by moving the electrodes closer together (increasing the electric field strength increases the amount of current emitted for a cathode operating in the space charge limited region) then it makes sense to detune a slightly smaller cathode radius, as then it offers the possibility of retuning if manufacturing tolerances cause the beam waist to be larger than desired.
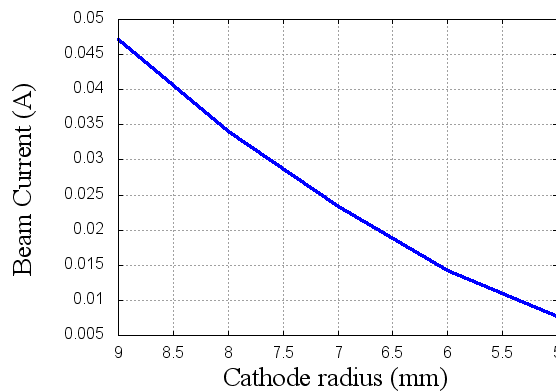
Figure 5.10 - Beam current generated by electron guns by reducing cathode radius
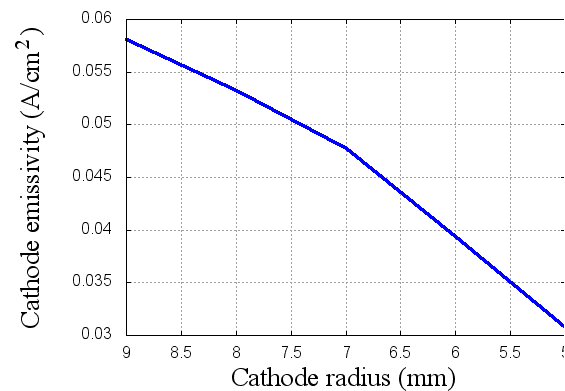
Figure 5.11 - Calculated cathode emissivity against axial cathode radius

Figure 5.12 shows the resulting beam current when the cathode to anode spacing is swept over a 15 mm range for an axial cathode radius of 6 mm. Clearly, the beam current increases with spacing. Figure 5.13 shows the corresponding effect on beam current as the cathode-to-anode spacing is swept. These results show that, as the cathode to anode spacing is reduced, both the beam waist and current increase. The minimum beam radius in the tuning range is significantly below the design goal which is highly desirable as the anode to cathode spacing can be tuned after manufacture. Therefore, manufacturing tolerances that affect the beam waist (e.g. machining tolerances causing the anode to be non-spherical) can be compensated for through post-production tuning.

145
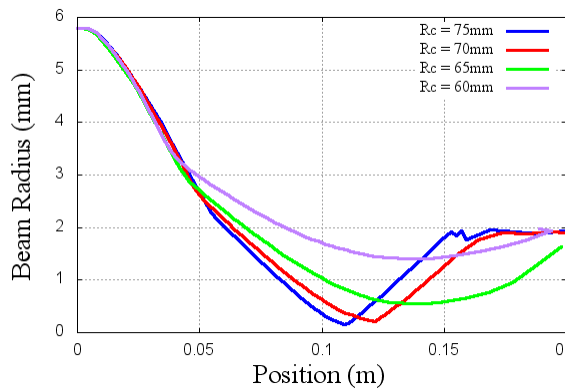
Figure 5.12 – Beam radius of different anode to cathode separation distances.
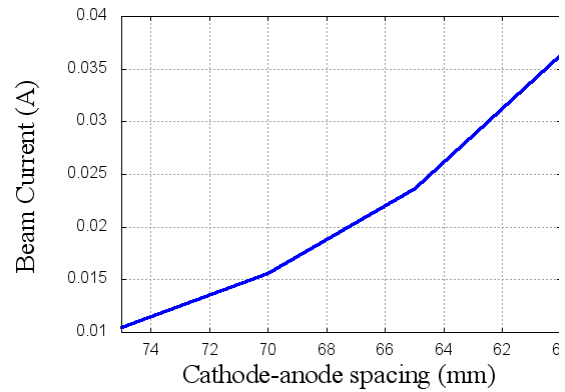
Figure 5.13 – Beam current generated from electron guns of reducing cathode to anode spacing.

As the current parameter set produces a beam current and waist close to the design goal but involves the simultaneous tuning of two variables it is worth using an optimiser to sharpen the design. Figure 5.14 compares the variation of beam waist with distance for the optimised design with the corresponding result for manually tuned parameters. The optimised beam profile is clearly narrower.
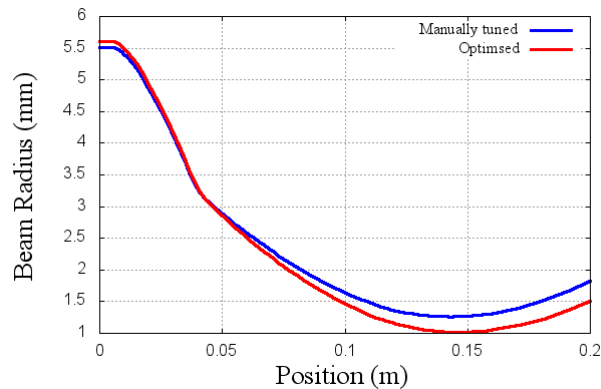
Figure 5.14 - Comparison of optimised beam curve to results obtained by manual tuning.

Table 5.4 summarises the performance characteristics of the final electron gun design. As seen in the table, the maximum beam current (noting that it should be possible to tune through moving the electrodes) is above specification by 20%, giving some headroom. The emissivity of the cathode is 0.028 A/cm^2, which is towards the low end of the range of commercial tungsten cathodes, again suggesting a conservative design. As we have now seen, a given design of electron gun requires the

cathode to have a sufficient emissivity and to be a certain shape. Consequently, before a complete gun can be designed, the cathode must be investigated to determine whether the cathode emissivity assumed earlier can be achieved in practise.

Table 5.4 – Parameter values in the final electron gun design.

Parameter	Symbol	Value	Unit
Normalised Velocity	v_{beam}	0.18	c
Voltage	V_0	8.3	kV
Current	I_0	29	mA
Beam radius	r_b	1	mm
Cathode Emissivity	ε_e	0.028	A/cm^2
Perveance	P	0.069	

Table 5.5 shows the parameter set defining the geometry of the final electron gun. Compared to the starting geometry, the anode to cathode spacing (difference between cathode and anode radii) has reduced, yielding a more compact gun, which has mechanical advantages. The cathode angle has also increased slightly; this change represents a slightly higher compression ratio, since the reduction in cathode to anode spacing has clearly been greater than the reduction in cathode area. Overall the gun geometry is highly manufacturable, possessing no small features, and the aspect ratio for the beam tunnel is such that it can be milled using standard bits. The cathode, complete with extended ground planes, is sufficiently large that the taper can be worked on a lathe using a conventional boring bar (since the axial cathode radius is large enough that the tool will not collide with the other side of the taper) The only awkward part of the geometry is the hemisphere needed for the anode but the radius is a round number and the gun can be tuned post production by altering the cathode to anode spacing.

Table 5.5 – Parameter values of the final gun geometry.

Parameter	Symbol	Value	Unit
Anode Radius	R_a	20	mm
Cathode Radius	R_c	62	mm
Beam waist	b_m	1	mm
Axial cathode radius	r_c	5.7	mm
Cathode Angle	θ	7	°

5.2   Hot Cathode

5.2.1 Introduction

The cathode is the source of electrons in the electron beam. Several different methods are commonly used to generate electrons in high power sources [16]. These include thermionic emission, field emission and the excitation of a plasma [17]. However, for travelling wave tubes, thermionic emission sources have traditionally been used [18], and this is the approach taken here.

Briefly, a thermionic emission cathode (hot cathode) works by heating a low work function material until the electrons within the cathode have sufficient kinetic energy to overcome the work function and escape into free space. It should be noted here that, without an electrostatic field removing the emitted electrons from the cathode, an electron cloud would form with a resulting electrostatic field that would act to reduce the rate of emission. This effect is known as the space charge limited emission [19]. As the process is independent of cathode material and dependant on the perveance of the beam it is covered later in the cathode design section (section 5.2.3). The first three design decisions to be made therefore are: the cathode material, the approximate temperature of operation and the method of heating. These must be chosen so that the specified minimum current density and shape are met (assuming the design of the electrodes previously found above).

Cathode lifetime is of great importance in a travelling wave tube, as this determines the overall lifetime of a sealed tube. Great research effort has therefore been spent on extending cathode life [20]. However, as the gun detailed here was originally intended for use in an experimental system, the lifetime (beyond a few hours) is unimportant as it is easy to replace the filament. Therefore, this section will focus on cathode types suitable for laboratory use.

As the cathode material choice is the most crucial to its operation, this aspect will be considered first. Broadly a material with a low work function is desired but at the same time it must be able to withstand the temperature needed to overcome the work function without distorting - remember that, as described earlier, the cathode must be shaped to focus the electron beam.

In addition, an electron gun intended for a lab bench system therefore it faces slightly different operating conditions than commercial guns. The first is that it is fairly easy to replace, therefore its lifetime need only be in range of 1-10 hours, rather than thousands of hours [21]. The other important difference is that the vacuum will not be that high and the system will be regularly raised up to atmospheric pressure to modify the slow wave structure. The cathode must therefore be fairly rugged, and able to survive multiple heating and cooling cycles and repeated exposure to air ambient.

These requirements rule out most of the better cathode types (oxide, dispenser etc.), which can only operate under high vacuum and require a lengthy bakeout procedure [22, 23] after exposure to atmosphere. Popular cathode materials containing thorium, such as thorium oxide or tungsten thorium alloys, can also be ruled out as the small improvement in performance is not worth the difficulties around safe handling [24]. The remaining cathode materials include metals such as tungsten (W) and tantalum (Ta) and compounds such as lanthanum hexaboride, LaB_6. As the latter is quite expensive it can be eliminated, leaving a refractory group metal as the most suitable material.

Figure 5.15 shows a variety of thermionic cathodes, including a tungsten filament, a LaB_6 crystal and dispenser types. Tungsten filaments are clearly the simplest and cheapest; however LaB_6 has a lower work function and is resistant to poisoning. Dispenser cathodes have provisions for continuously replacing evaporated electron-emitting material.
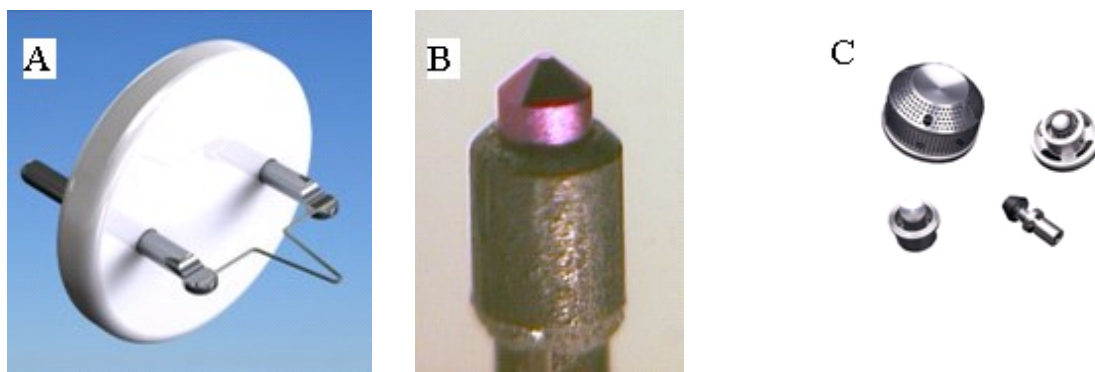
Figure 5.15 - Hot cathode electron emitters: a) tungsten filament [9] b) LaB_6 crystal [25] c) dispenser [26]

Figure 5.16 shows the variation of emission density with temperature for several common cathode materials. Whilst not having the highest emission, tungsten is the traditional choice, mainly as it is more resistant to poisoning, easier to work and lower cost than the other refractory group metals. Another good choice would be tantalum, which has an advantage in that it has a slightly lower work function but most of the same advantages as tungsten. However, as Ta is significantly more expensive, W is normally preferred (unless the cathode construction requires welding, as a W-Ta weld is much easier to execute than a W-W weld).
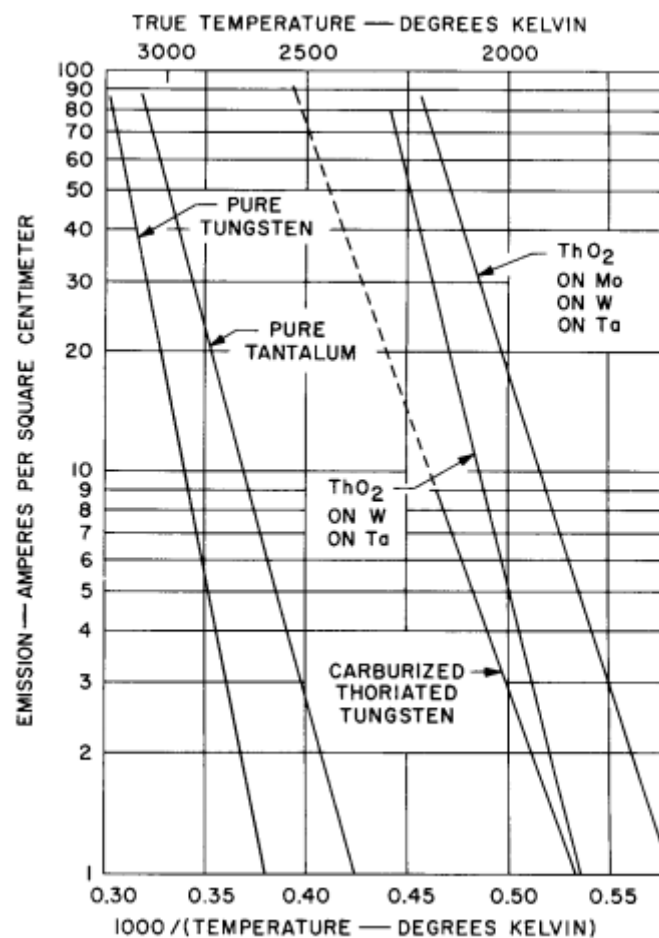
Figure 5.16 - Graph of emission versus temperature for common cathode materials from [27].

Whilst more exotic cathode materials are normally preferred for production systems, a directly heated tungsten filament has many advantages. W is fairly inexpensive and widely available, the metal is hard to poison (other materials' emissivity can be ruined by trace impurities), it is rugged enough to operate in a relatively low vacuum and is unaffected by exposure to atmosphere. The only disadvantages are

that the emissivity is lower than more advanced cathode materials and that it has to be directly heated to a rather extreme temperature (approximately 2500K [28,29]), which severely limits its lifetime. However, as discussed earlier the filament can be easily replaced in a lab system so the lifetime is not a major disadvantage. The high required temperature complicates the design, as a reasonably large area of tungsten must be uniformly heated to a fairly high temperature. Therefore, analysis and simulation were performed on several different cathode designs to determine possible geometries, the results of which are presented in the next section.

5.2.2 Operating Temperature

In order for the cathode to be operating in the space charge limited region it must have a certain minimum emissivity across its entire emitting surface, which is set by the perveance of the electron gun. As there are no detrimental effects to the normal operation of a gun from a higher emissivity, the cathode is generally designed to exceed this minimum. Since the emissivity can be increased by increasing the heater current (up to the point where the cathode melts) it makes sense to design the cathode for a low operating temperature. Any errors or poorly chosen approximations can then be compensated for by increasing the heater current. Designing for a lower emissivity than what is likely to be possible also allows the use of wire wound cathodes with a low fill factor, which is desirable as these are much easier to manufacture than tightly wound spirals.

However, in a directly heated cathode, the losses due to thermal conduction into the mounting points of the cathode enforce a temperature gradient along the filament, which must be considered. Figure 5.17 shows a sketch of a typical temperature profile along the filament with the dotted line representing the minimum temperature needed to meet the desired emissivity. As shown by the figure, the temperature of the cathode is significantly below the desired temperature at the mounts (due to thermal conduction) although it rises in the middle beyond the temperature needed to meet the emissivity requirements.

151
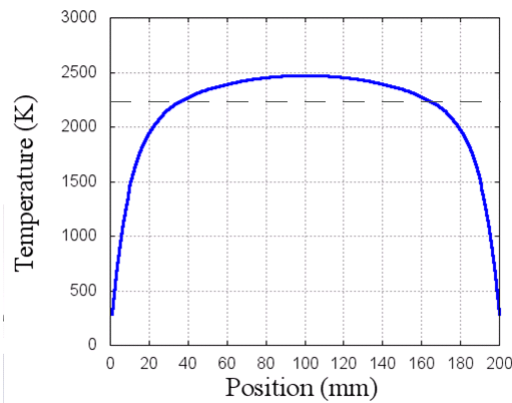
Figure 5.17 - Example of a typical filament temperature profile.

Since the temperature of the filament is significantly reduced at the mounts, these sections cannot be used as part of the emission surface. The usual solution for these redundant sections is to loop them around at the back of the cathode. Of course, the lifetime of the cathode is strongly linked to its operating temperature. Exceeding the required temperature is undesirable as it limits cathode lifetime for no increase in performance. In the limit, this could result in an unusable cathode even for an experimental system.

Figure 5.18 shows a diagram of a typical cathode assembly, with the inclined ground plane, cathode itself and mounting lugs labelled. Lower resistance wire is used in between the mounting lugs and the supply so that the resistive losses are concentrated in the cathode. As shown by the diagram there is an additional length of wire between the cathode and the mounting lugs to insulate the emitting surface from thermal conduction losses into the mounts such that the entire path of the cathode inside the inclined ground is at elevated temperature i.e. the section of wire between 0 to 40 mm in Figure 5.17 is kept behind the emitting surface.
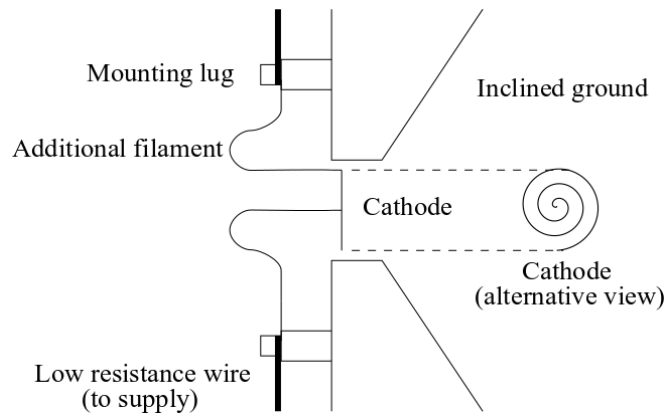
Figure 5.18 - Typical layout of filament.

Figure 5.19 shows desirable and undesirable cathode temperature profiles. The blue trace represents the ideal case – the temperature rises quickly to a suitable value, but no part of the wire is over the minimum temperature needed for the specified emissivity. The red trace shows a temperature profile with excessive overshoot; while the operating region (the length of wire with a temperature equal to or larger than the blue trace) is reasonable, the peak temperature is at a level that will severely limit the lifetime of the cathode. The green trace shows another undesirable case, where the operating region is small compared to the length of the wire. Whilst the below-temperature wire could be looped behind the emitting surface, a non-uniform wire radius could lead to the peak temperature being offset from the middle of the wire, necessitating careful cathode alignment. Consequently, calculations were performed to choose a suitable filament, to analyse the dimensions and currents needed in arrangements with different cross sections such as ribbon and wire.
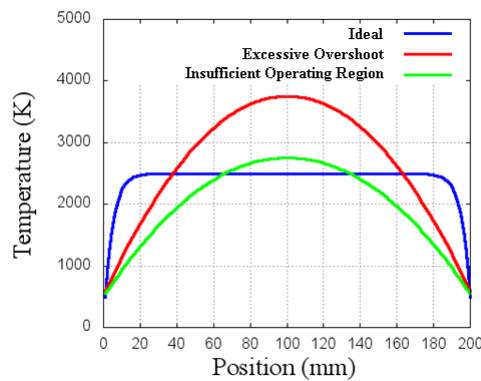
Figure 5.19 - Ideal and undesirable filament temperature profiles.

5.2.3 Cathode design

This section will discuss the analysis and CAD simulations performed in order to design the cathode (using a differential solver within MATLAB). The purpose of the work is to choose a filament geometry and determine its likely heater current. An approximate figure for the emissivity that can be achieved with a tungsten cathode heated by a realistic current is required as the electron gun was designed using the textbook figure for emissivity of W at a moderate temperature [15,14] and it is important to determine whether this emissivity can be achieved with a cathode of the calculated size.

A thermionic cathode is a thermal system whose equilibrium is described by the following power-balance equation:

$$P_T(I) \ = \ P_R(T) + P_C(T) + P_E(T) \tag{5.1}$$

Where:

$P_I(I)$ - Power from restive heating of the cathode, dependant on heater current I

$P_R(T)$ – Power of radiative cooling, dependant on temperature T

$P_C(T)$ – Power of conductive cooling, dependant on temperature T

$P_E(T)$ – Power of emitted electrons, dependant on temperature T

It is desired to solve this differential equation for *T* such that the relation between current and temperature of various cathode geometries can be plotted. Starting from the left, we can write:

$$P_T(I) \ = I^2 R \tag{5.2}$$

As the cathode is assumed to be a length of wire (possibly of a non-circular cross section) the standard equation [30] for cathode resistance can be used, namely:

$$R_{cathode} = \frac{\rho L}{A} \tag{5.3}$$

Here ρ is the resistivity, L is the length of the wire and A is its cross-sectional area. However, as the range of temperatures will be fairly extreme (2000-2800K) then the resistivity will be a function of temperature. In a linear model, the temperature variation of resistivity can be taken as:

$$\rho = \rho_0 + \alpha T \tag{5.4}$$

Here α is a proportionality constant. Substituting (5.) and (5.) into (5.) gives an expression for the heating power, expressed in terms of I and T, as:

$$P_I(I) \;=\; I^2 \frac{(\rho + \alpha T)L}{A} \tag{5.5}$$

Moving onto the right-hand side of the equation, there are three terms, each representing a different path for energy to leave the cathode. The energy leaving through black body radiation is represented by the term $P_R(T)$ and is given by the Stefan–Boltzmann law [30]:

$$P_R(T) \;=\; S\epsilon\sigma T^4 \tag{5.6}$$

Here S is the total effective surface area of the body (the surface area of the wire), ϵ is the emissivity, σ is the Stefan–Boltzmann constant and T is the surface temperature. For small bodies, the surface temperature is similar to the bulk temperature so the latter can be used. Note that (5.) can only be used if none of the radiation is reabsorbed by the structure (as would be the case for a concave mirror). When an arrangement is used that shadows part of itself the effective surface area is used instead; this quantity is the total cross-sectional area of the radiating body viewed from a Gaussian surface.

The conductive losses are given by the term $P_C(T)$ and represent the power flow out of the hot filament into the mounts. $P_C(T)$ is governed by Fourier's law of heat conduction [30] which, for the 1D case, can be written as:

$$P_c(\text{T}) = -Ak\frac{dT}{dx} \tag{5.7}$$

Here k is the thermal conductivity and x is the position along the filament. The system of equations can now be solved by constructing a further equation that represents the energy balance. Figure 5.20 shows a diagram of an infinitesimal segment of the filament with the radiated heat, resistive heat generation and conductive heat flow into and out of the segment labelled.
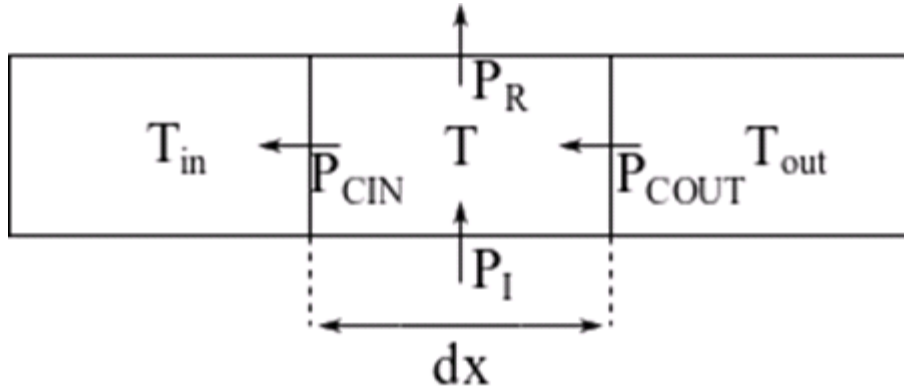
Figure 5.20- Thermal flow block diagram.

In the steady state the power balance is:

$$P_I + P_{CIN} = P_R + P_{COUT} \qquad (5.8)$$

Where:

$$P_R = S\epsilon\sigma T^4 dx \qquad (5.9)$$

$$P_I = I^2 \frac{\rho + \alpha T}{A} dx \qquad (5.10)$$

$$P_{CIN} = Ak \frac{T - T_{IN}}{dx} \qquad (5.11)$$

$$P_{COUT} = Ak \frac{T_{OUT} - T}{dx} \qquad (5.12)$$

As:

$$P_{CIN} - P_{COUT} = -Ak \frac{d^2 T}{dx^2} dx \qquad (5.13)$$

Then the power balance can be written as:

$$S\epsilon\sigma T^4 - I^2\frac{\rho + \alpha T}{A} - Ak\frac{d^2 T}{dx^2} = 0 \tag{5.14}$$

From inspection, (5.) can be split into two main regions: firstly a 'steady' region where the radiation losses greatly exceed the conduction losses, and secondly a region where the conduction loss is significant. Therefore, for a given geometry, the analysis can also be broken down into two parts, firstly an approximate analysis that gives a relationship between the filament temperature and heater current and secondly an exact differential analysis that yields the filament length needed to reach the operating temperature.

5.2.3.1 Approximate Analysis

Making the relatively crude approximation that the temperature profile is approximately uniform, the second derivative $\frac{d^2 T}{dx^2}$ can be neglected, giving:

$$S\epsilon\sigma T^4 - I^2\frac{\rho + \alpha T}{A} = 0 \tag{5.15}$$

This equation can easily be solved. Figure 5.21 shows a plot of temperature versus heater current for three commonly available forms of tungsten: thin wire (0.1 mm diameter), thick wire (1 mm diameter) and tungsten foil (0.1 mm thickness). As can be seen, the thinner wire requires the lowest heater current, while the foil requires an impractically large current.
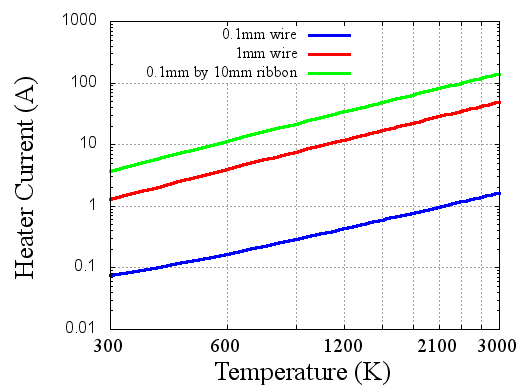
Figure 5.21 - Approximate temperature versus heater current for different possible cathode cross sections.

5.2.3.2 Exact Differential Analysis

We now provide an exact solution of Equation 3.14, with the aim of determining the length of filament between the mounting block and the point where a constant temperature is obtained. Introducing the new variable:

$$X = \frac{x}{L} \tag{5.16}$$

Where L is the length of the filament, then we can write:

$$\frac{dT}{dx} = \frac{1}{L}\frac{dT}{dX} \tag{5.17}$$

$$\frac{d^2T}{dx^2} = \frac{1}{L^2}\frac{d^2T}{dX^2} \tag{5.18}$$

Substituting into Equation 3.14 and re-arranging, we then get:

$$L^2 S\epsilon\sigma T^4 - L^2 I^2 \frac{\rho + \alpha T}{A} - Ak\frac{d^2T}{dx^2} = 0 \tag{5.19}$$

This equation can now be written in simplified form as:

$$aT^4 - bT - c = \frac{d^2T}{dX^2} \tag{5.20}$$

Where the constants a, b and c are given by:

$$a = \frac{S\epsilon\sigma L^2}{Ak} \tag{5.21}$$

$$b = \frac{\alpha I^2 L^2}{kA^2} \qquad (5.22)$$

$$c = \frac{\rho I^2 L^2}{kA^2} \qquad (5.23)$$

Unfortunately, the equation is a non-linear second-order differential equation and therefore hard to solve analytically. A numerical method will therefore be used instead. The first step is to rewrite the equation as a system of coupled first order equations by introducing two new variables:

$$T_1 = T \qquad (5.24)$$

$$T_2 = \frac{dT}{dX} \qquad (5.25)$$

Substituting these into the original gives a pair of coupled equations:

$$\frac{dT_1}{dX} = T_2 \qquad (5.26)$$

$$\frac{dT_2}{dX} = aT_1^4 - bT_1 - c \qquad (5.27)$$

Standard differential equation solvers integrate from a single point where all the boundary conditions are specified. Unfortunately, the boundary conditions are split here. Taking $X = 0$ as the middle of the filament, these can be written as $T = T_0$ at $X = \pm 0.5$, where T_0 is the ambient temperature. However, as the temperature profile must be symmetric, only one half of the solution is required, and the boundary conditions can be rewritten as $\frac{dT}{dX} = 0$ at $X = 0$ and $T = T_0$ at $X = 0.5$. To render the equation soluble, a temperature T^* is assumed at $X = 0$, thus moving both boundary conditions to the same point. The equations are then integrated, the temperature at $X = 0.5$ is compared with the boundary condition T_0, and the value of T^* is adjusted until sufficient agreement is obtained.

A simple method of finding an accurate value of T^* is through bisection. First, three trial values are defined: T^*_{high}, T^*_{low}, and T^*_{mid} (the average of the high and low values). For example, if the solution was to be expected within the range of 0-10,000 K then $T^*_{high} = 10,000$ K, $T^*_{low} = 0$ K and $T^*_{mid} = 5000$

K. Next the solver evaluates all three trial values and calculates the temperature error at $X = 0.5$. The sign of the error is then analysed. Assuming the solution lies inside the search range there are two possibilities: either two positive errors and one negative, or two negative and one positive. As the solution must lie between the pair with opposite signs, the process can be repeated using these values as approximations for T^*_{high} and T^*_{low}. Each time this process is repeated, the range within which the solution must lie will be halved. Accordingly, the number of trials required for a specified accuracy can be calculated. For example, a starting range of 0-10,000K requires 14 trials to reach an accuracy of above 1 K (since 10,000 K/2^{14} = 0.61 K). Figure 5.22 shows the output from a solver operating in this manner. T_0 is assumed to be at ambient (300 K) and the parameters are approximated to be $a = 2.5e-9$, $b = 0.02$ and $c = -4$, with the heater current stepping from 10 A to 50 A.
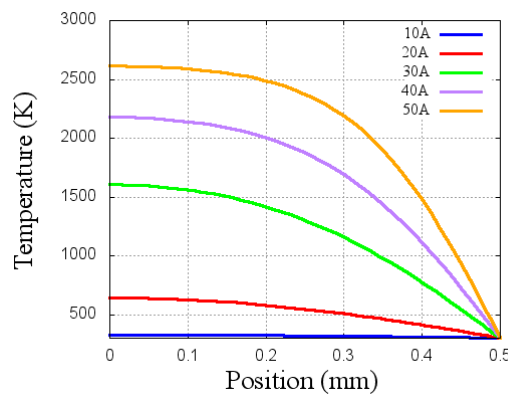
Figure 5.22 – Numerical solution for the temperature profile of a hot-wire filament obtained using approximate parameters.

Next the solver was run for a range of cathode geometries with accurate constants for a range of currents. Table 5.6 shows the constants used. Several geometries were investigated, based on commercially available tungsten wire: thin wire (0.1 mm diameter), thick wire (1 mm diameter) and tungsten foil (0.1 mm thickness). From the earlier discussion, and the variations of emissivity with temperature, a tunable range of 2000-2800 K at a moderate current (under 50 A) is highly desirable.

Table 5.6 - Constants used by differential equation solver.

Parameter	Symbol	Value	Units	Reference
Thermal emissivity	ϵ	0.2		[30]
Stefan-boltzmann constant	σ	5.67E-08	W/m^2K^4	
Thermal conductivity	k	175	W/mK	[31]
Resistivity	ρ	6.00E-08	Ω/m	[32]
Temperature dependant resistivity	α	3.00E-10	Ω/m	

Figure 5.23 shows the simulated temperature profile obtained for 0.1 mm tungsten wire, 30 mm long over a sweep of heater current from 0.3 A to 1.5 A. From the graph we can see that the desired temperature range corresponds to a current range of 1 A to 1.5 A, with the wire taking around 30 mm to reach the operating temperature from a mount held at 300 K. In practice, the mount will not be a perfect sink so this distance will be somewhat lower
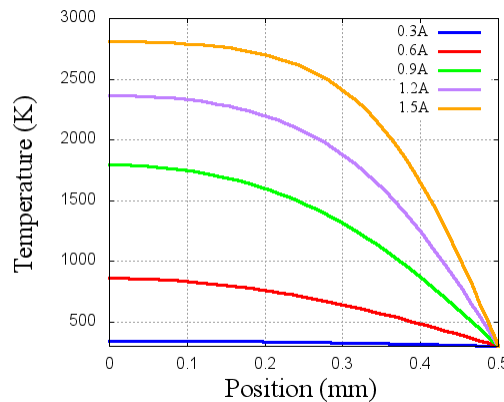
Figure 5.23 – Temperature profiles obtained for different heater currents, assuming 0.1 mm tungsten wire, 30 mm long.

Figure 5.24 shows the temperature profile of 1 mm tungsten wire, 100 mm long over a sweep of heater current from 10A to 50A. Looking at the graph we can see that a temperature range of 2000-2800 K can indeed be achieved, using a current range of 30-50 A. The wire takes around 40 mm to reach operating temperature although the temperature profiles are noticeably more rounded than those from the 0.1 mm wire, despite the increase in wire length.
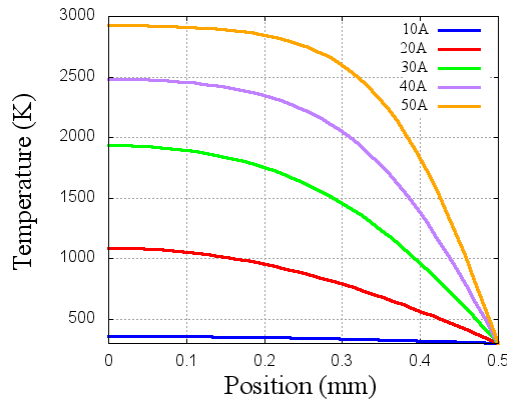
Figure 5.24 - Temperature profiles obtained for different heater currents, assuming 1 mm tungsten wire, 100 mm long.

Figure 5.25 shows the temperature profile of 0.1 mm by 1 mm tungsten foil, 50 mm long over a sweep of heater current from 25 A to 125 A. These results show that the desired temperature range (2000-2800 K) now requires a heater current of between 100-125 A. Whilst these curves are fairly pessimistic (as it is unlikely that the mounts would remain at ambient temperature while passing a 100A current), the required current is far too high to be practical.
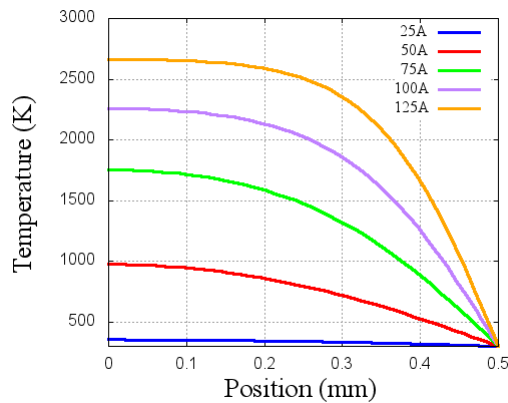
Figure 5.25 - Temperature profiles obtained for different heater currents, assuming 0.1 mm by 10 mm tungsten ribbon, 50 mm long.

5.2.4 Intermediate Conclusions

From the simulation results, we can see that the required heater current (as expected) is strongly dependant on the diameter of the wire. Whilst tungsten foil would allow a uniform cathode, it would require an extremely large heater current, which could be hard to generate. The design would be greatly simplified if a coil of a smaller diameter wire could be used instead. Accordingly, further simulations

were carried out to investigate the effects of a non-uniform cathode and whether these would prevent the gun's usual operation.

Figure 29 shows a diagram of the simulated cathode structures, which include a series of concentric circles (approximating a spiral) and the original uniform disc. Figure 30 shows the variation of beam width with axial position obtained in each case. From these simulations we can conclude that the degradation in beam uniformity caused by using a planar spiral cathode is not significant enough to affect the operation of the gun. Therefore, a planar spiral cathode will be used, as reducing the input current and minimising the material costs are more important than a slight increase in beam uniformity.

Whilst a 1.5 A current is more manageable than a 50 A current, 0.1 mm diameter wire could prove difficult to form into the tight spiral without causing any thermal shorts (i.e without any part of the spiral touching the inclined ground plane). Therefore, it makes sense to design the system for the maximum diameter wire that can be operated with the available vacuum feed through. Since this is 50 A, 1 mm wire was chosen.

Figure 5.26 Hot cathode geometries: a) approximate spiral   b) solid cathode.

Figure 5.27 – Simulated variation of beam width with axial position obtained using a solid cathode and one made from a series of concentric circles approximating a spiral.

5.3   Magnet

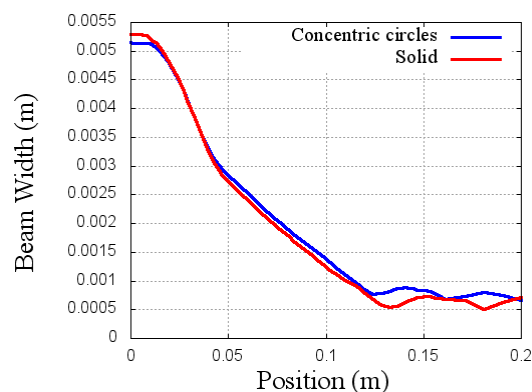### 5.3.1 Introduction

As mentioned before, the electron beam requires a magnet to remain collimated. The purpose of the magnetic field is to provide a force to overcome the space charge, which, if unopposed, will cause the beam to diverge. The following sections discuss the space charge force, the magnet types used and their implementation in more detail, with the aim of providing a suitable magnet design for the gun described earlier. To simplify the discussion, we start by considering steady state behaviour, assuming that the beam is focussed, inside a magnetic field and there are no end effects, i.e. that both the beam and field extend to infinity. Figure 5.28 shows a section of the steady state beam with the beam diameter, direction of electron motion, magnetic field and the space charge force labelled.
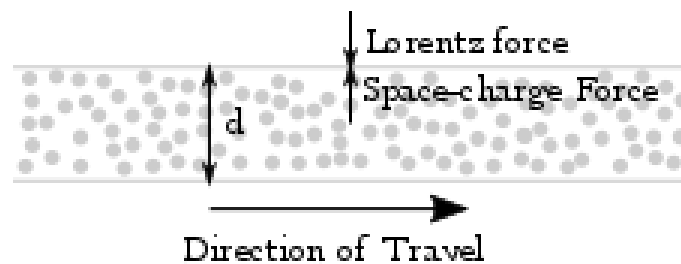
Figure 5.28 - Steady state electron beam under magnetic focussing.

The space charge force is opposed by the Lorentz force that any moving charge will experience when passing through a magnetic field [11], given by:

$$\boldsymbol{F} = q\boldsymbol{v} \times \boldsymbol{B}$$

Here q is the charge, $\boldsymbol{v}$ is the velocity, and $\boldsymbol{B}$ is the magnetic flux density. Initially it appears that the magnetic field would have to be perpendicular to the direction of travel to obtain a suitable force, which would require the field lines to be circular. As generating a field with this amount of curl using an external magnet is extremely difficult, an axial magnetic field is generally used in conjunction with a rotating beam. In this case, the electrons move in a corkscrew path, so that the rotational part of their velocity combines with the axial magnetic field to provide an inward force which opposes the space charge force, allow the beam to be in equilibrium.

The radius of rotation of an individual electron is determined by the amount by which the Lorentz force exceeds the space charge force, implying that the radius will reduce as the space charge force decreases. Similarly, the space charge force experienced by an electron depends on the density of the beam (implying that the space charge force will reduce as it expands the beam). The combination of these two effects means that the radius of an electron beam using axial magnetic focusing will be determined by its current and the strength of the axial magnetic field, as shown in the next section.

5.3.2   Types of Magnetic Insertion

The section above discusses the steady state behaviour of the beam, assuming that the beam and magnetic field both extend to infinity. However, in a physically realisable tube, the beam and the magnetic field must clearly start and end at finite positions. Further analysis is required to determine the effects of these discontinuities. Those caused by an increasing magnetic field are generally referred to as 'insertion'. The behaviour of the electron beam in a declining magnetic field is usually grouped together with the design of the collector. Normally the beam is simply allowed to diverge under its own space charge forces; however, the degree of divergence depends on the style of collector used. As the design of the collector is covered in a separate section it will not be discussed here; this section is dedicated to the discussion of insertion.

There are two main types of insertion, which are normally referred to as Brillouin insertion and immersed flow [4]. In Brillouin insertion, the magnetic field has the exact calculated value for a Brillouin field and starts abruptly (through the use of a pole plate) at the waist of the focused beam as it emerges from the electron gun.

Figure 5.29 shows a Brillouin insertion, with the magnetic field, pole plate and electron beam labelled. Theoretically a Brillouin insertion is ideal. However, the magnetic field cannot start instantaneously, and it is unlikely to be possible to align the field start point exactly with the beam waist. Undesirable behaviour caused by these effects must therefore be studied.
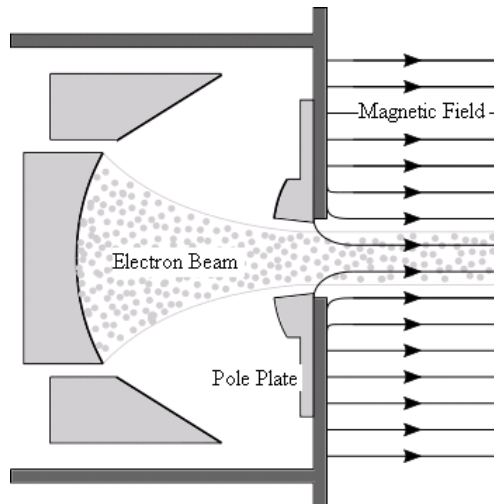
Figure 5.29- Electron beam with Brillouin insertion.

As shown in earlier, a specific strength of axial magnetic field is required to balance the space charge forces for a given beam, called the Brillouin value. By starting this field at the beam waist (where the electrons have no radial component of velocity) the space charge force will be cancelled and the electrons will continue forward with their radial velocity remaining zero. However, if the field starts at a slightly different point, the beam will enter the field with a radial velocity component and simple harmonic motion (SHM) will occur in the radial direction. Because the magnetic field only provides a radial force, it does not damp this motion. Figure 5.30 shows the macroscopic effect of an oscillating radial velocity component. The beam expands and contracts as it travels, an effect commonly known as scalloping [2]. This effect is undesirable as it causes a reduction in the filling factor of the beam tunnel, which in turn reduces the interaction impedance and the gain.
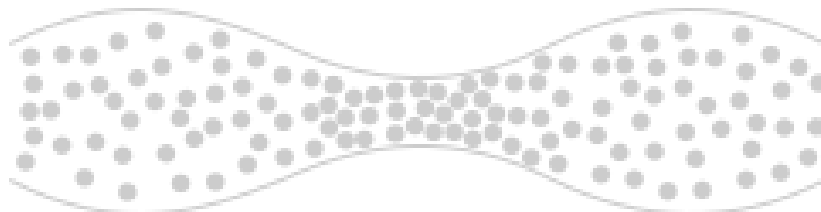
Figure 5.30 – Example of a scalloped electron beam.

If magnetic field strengths beyond the Brillouin value are used, scalloping again occurs. If a magnetic field beyond the Brillouin limit starts at the beam waist then the electrons will experience a radial acceleration as the magnetic focusing force will be greater than the space charge debunching force,

which again results in radial SHM. The Brillouin limit applies to quiescent conditions. When the electron beam is used for amplification, the electromagnetic forces in the slow wave structure will compress the beam in the direction of travel [33]. As the space charge force will be increased by this compression, it will exceed the force provided by the magnet, causing the beam to diverge radially.

The final (and most major problem) is that abrupt insertion requires a magnet with a pole plate carrying a very small hole, with the quality of the insertion being dependent on the size of this hole. Figure 35 shows a sketch of an ideal and a non-ideal insertion. The use of a pole plate with a small aperture poses a serious fabrication challenge as either the ferromagnetic pole plate must penetrate the vacuum chamber or the vacuum chamber has to be extremely thin at the insertion point.
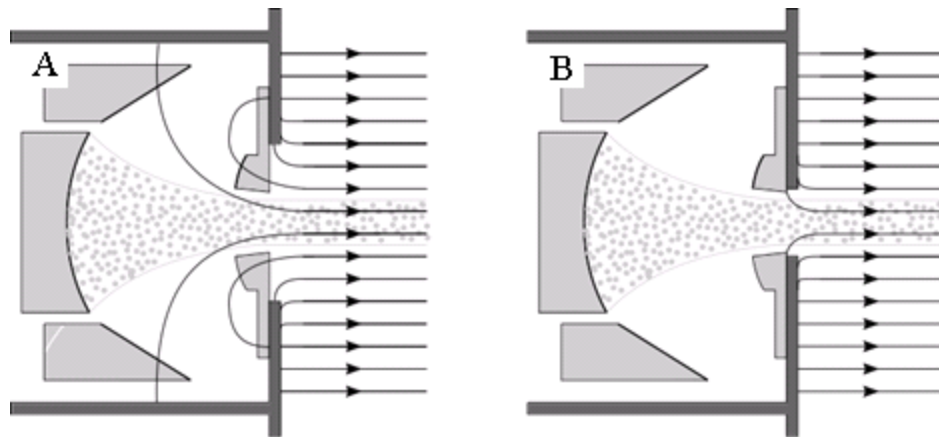
Figure 35 Pole plates: a) non-ideal (wide aperture), and b) ideal (narrow aperture).

While Brillouin insertion has been used successfully, it has several significant drawbacks, with the only advantages being a simple design procedure and the lowest magnetic field strength of any method. The alternative is immersed flow as shown in Figure 5.31. Here the pole plate has been removed so the magnetic field no longer starts abruptly, and there is significant magnetic flux at the cathode. The flux lines tighten with the electron beam, representing an increase in the magnetic field strength. Provided the rate of change of magnetic field is matched with the rate of increase in space charge density the beam will remain well formed. Therefore, it is desired to calculate the shape of the magnetic field for this insertion and the parameters of a suitable magnet to generate it.
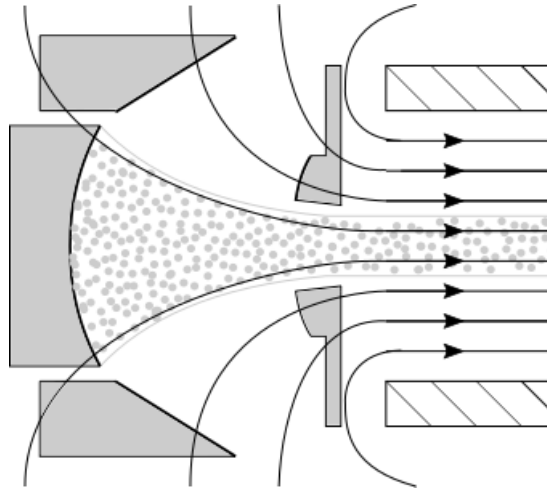
Figure 5.31 - Electron gun using immersed flow.

5.3.3 Magnet Design

The simplest solution for matching the rate of compression of the beam to the rate of increase of magnetic field strength is to assume that they will differ by a scalar value at all points and that the strength far down the beam tunnel is given by the steady-state value. The usual source for such a field is an open-ended air cored solenoid [33], which provides a decaying field beyond its ends, with the rate of decay being determined by the diameter of the coil (at least, for long solenoids). Figure 5.32a shows the area of a focussing beam against position, and Figure 5.32b shows the corresponding variation in magnetic field strength from a large open-ended solenoid. As can be seen in the diagram the area of the beam falls rapidly before reaching a plateau, following a similar variation to the magnetic field itself. Therefore, it should be possible to match the beam area curve to the shoulder of the magnetic field strength curve.
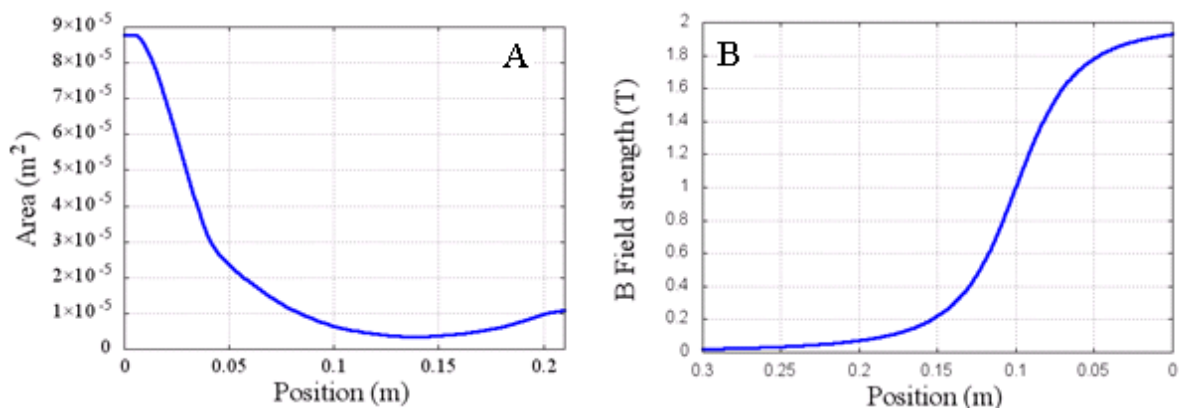
Figure 5.32 Immersed flow electron gun design: a) axial variation in beam area, and b) axial variation in flux density from open-ended solenoid.

The rate of decay of the magnetic field near the end of a solenoid is determined by the size of the solenoids's aperture, with the overall field shape being unaffected by the absolute value of the current. The diameter of the solenoid needed to match the compression produced by a given electron gun can therefore be found as follows. The first step is to calculate the required 'final' field strength of the beam, which is given by the beam equilibrium equation [8]:

$$a = \frac{1}{B_z} \sqrt{\left(\frac{2I_0}{\pi \eta \epsilon_0 u_0}\right)} \tag{5.28}$$

Here B_z is the axial magnetic flux density, ϵ_0 is the permittivity of free space, $u_0 = 0.18c$ is the axial velocity, η is the electron charge to mass ratio, a is the equilibrium radius and I_0 is the beam current. Rearranging, the magnetic field strength needed to contain this beam at the Brillouin limit is clearly:

$$B_z = \frac{1}{a} \sqrt{\frac{2I_0}{\pi \eta \epsilon_0 u_0}} \tag{5.29}$$

For an immersed flow focussed system, a flux density 2-3 times this value is normally used. Using the electron beam parameters determined in the slow wave structure design, namely $a = 1$ mm and $I_b = 30$ mA then gives a target magnetic flux density of $B_z = 0.015\ T$.

Now, the magnetic field strength at the centre of an open ended, air core solenoid far from the ends is [11]:

$$B = \frac{\mu_0 N I_w}{l} \tag{5.30}$$

Here N is the number of turns, I_w is the current in the windings and l is the length of the solenoid. Calculation of the number of turns and current needed requires a detailed approach that considers both the assembly and thermal issues, so for this analysis the combined value (known as the current-turns product) will be used instead. The next step is to match the rate of change of field strength from an open-ended solenoid to the rate of change of increase in the beam density.

Assuming that it runs from $z = z_{\text{offset}}$ to $z = L + z_{\text{offset}}$), the axial magnetic flux density of an open-ended solenoid, far outside the ends and on its axis is given by [30]:

$$B_z = \frac{\mu_0 N I_w}{2} \left(\frac{L + z}{\sqrt{(L + z)^2 + R^2}} - \frac{(z - z_{offset-})}{\sqrt{R^2 + (z - z_{offset})^2}} \right) \qquad (5.31)$$

As the current-turns value in this equation is set by the steady state value calculated above and the length is set by the length of the drift tube and slow wave structure then there are only two degrees of freedom: the diameter of the aperture of the magnet and the offset between the solenoid and the electron gun.

For values of L that are large with respect to the radius of the solenoid R, and correcting the sign to match the beam narrowing with increasing distance, Equation 5. reduces to:

$$B_z = \frac{\mu_0 N I_w}{2} \left(1 + \frac{(z - z_{offset})}{\sqrt{R^2 + (z - z_{offset})^2}} \right) \qquad (5.32)$$

The condition for immersed flow is that the increase in magnetic field matches the decrease in beam area and finished with the magnetic field being some multiple of the brillouin limit (typically 2-3). Therefore we can write

$$k = B_z \, \pi r_b^2 \qquad (5.33)$$

As the current-turns is a scalar quantity k can be absorbed into B_z (allowing k to be set to 1) thus

$$\pi r_b^2 = \frac{1}{B_z} \qquad (5.34)$$

Which can then be solved using standard curve fitting techniques to find R and Z_{offset}. Since the value of B_z and the beam width far into the solenoid is known from the beam equilibrium equation, both the beam width and B_z can be normalised to their final values, allowing them to be plotted on the same axes. Standard curve fitting techniques can then be used to find values of z_{offset} and R such that f(z) matches the beam curve. Since the increase in magnetic field should match the decrease in beam area

(so that the amount of flux the beam intersects remains constant) then the ideal magnetic field is simply the inverse of the beam area against position. Figure 5.33 shows a comparison between the ideal axial magnetic field variation and that obtained from a solenoid of 0.035 diameter after carrying out such an exercise with the MATLAB curve fitting toolbox (with both functions inverted to aid presentation). Clearly, there is reasonable agreement.
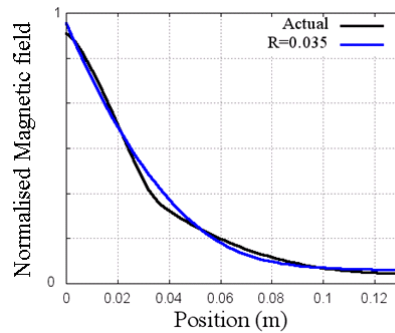
Figure 5.33 - Comparison between the ideal axial magnetic field variation and that obtained from a solenoid of 0.035 diameter (inverted).

However, a 35 mm radius magnet represents a relatively small internal bore, which is likely to hinder mechanical construction of other parts of the system. To increase the room available for the slow wave structure, the effect of increasing the solenoid radius was therefore studied. Figure 5.34 presents curves of normalised field strength against position for coil radii varying from 35 mm (the current best fit) up to 60 mm. In each case, the parameters shown in Table 7 were used. The results suggest that a 40-50 mm radius represents a reasonable compromise between the error in the definition of the field and tolerance for manufacture.
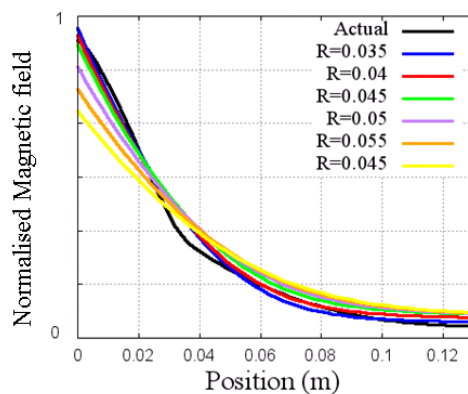
Figure 5.34 – Axial variation of magnetic fringing fluxes obtained from solenoids of different radii.

171

Table 5.7 - Parameter values used to calculate the curves in Figure 5.34.

R	z_{off}	a
0.03551	0.07478	2.79E-06
0.04	0.07257	3.50E-06
0.045	0.07393	3.98E-06
0.05	0.0785	3.95E-06
0.055	0.0828	3.87E-06
0.06	0.08688	3.75E-06

As the curves are only similar, there is still some error in the magnetic field, which may cause an undesirable beam shape. Because magnetic fields follow the principle of superposition, additional correction coils can be added with different diameters and currents to reduce the error between the ideal and actual magnetic field curves. The parameters for such a coil can be calculated using the method above but matching to the error in the magnetic field, rather than to the beam density.

Figure 5.35 shows a comparison between the ideal magnetic field and that produced from a two-coil system against position. From the plot we can see that the two-coil system produces a significantly-improved approximation, with a slight ripple. Using additional coils, the ripple could be further reduced, and specified using the usual techniques. However, an additional coil adds complexity to the system so it should only be used if it improves the performance of the electron beam sufficiently.

Figure 5.36 shows a comparison of the beam profiles obtained using one- and two-coil systems, showing that the scalloping in the beam is slightly reduced by the additional coil. However, the secondary coil has a limited effect and it appears that the design goals can be met with only one coil. Despite this, the secondary coil may allow for the correction of manufacturing errors within the gun, but as it is possible to retrofit the secondary coil (the apertures for the main coil are the same in both systems, while the secondary has a smaller radius) it makes more engineering sense to try the one coil system first, and add the second only if the original's performance is unsatisfactory.
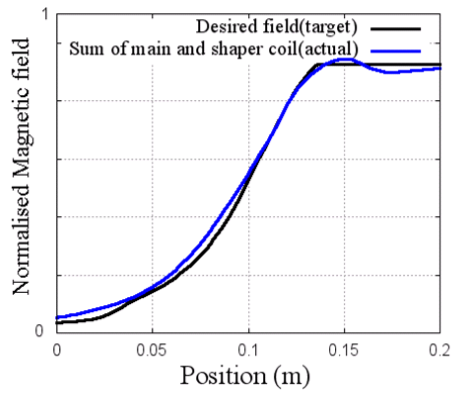
Figure 5.35 - comparison between the ideal field and that from the proposed two coil system
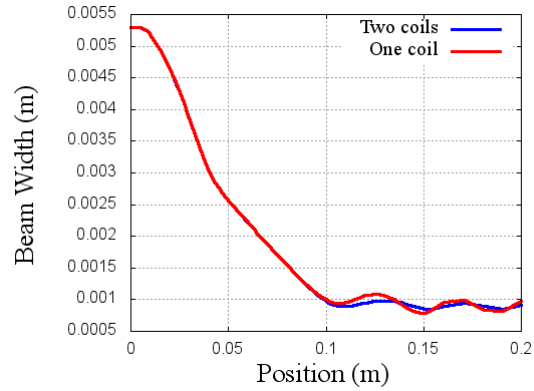
Figure 5.36 - Comparison on one and two coil focussing on simulated beam radius.

In order to evaluate whether the analytical parameters are optimal, a series of parametric sweeps were performed. The design has three parameters of which one, the bore, has been defined by mechanical considerations (suitable coil formers are only available in certain diameters). Therefore, only the other two, offset and field strength are of interest. As the beam waist should be relatively insensitive to the magnetic field strength within an immersed flow system [33] then the primary parameter is the relative position of the electrodes to the start of the magnet. Consequently, a sweep of the magnet's position was performed. Based on earlier results, the optimal position is the one that produces the least scalloping. Figure 5.37 shows the beam profiles for a sweep of the relative position of the magnet to the electrodes. As can be seen, the calculated value of offset (95 mm) is far from optimal, with an offset of 140 mm providing a narrower beam with smaller scallops. It is also notable that a relatively large change in offset is needed to degrade the beam width, so the gun will not need precise alignment.

Figure 5.37 - Sweep of solenoid offset. Magnetic field strength (0.05T) and radius (50 mm).

Finally, as stated earlier, when operating correctly under immersed flow the beam profile should be insensitive to changes in the magnetic field strength (i.e. adjusting the current in the solenoid). Therefore, the quality of the insertion can be tested by observing the change in scalloping from changes in the magnetic field. The assumption itself can also be tested by also sweeping the magnetic field for a relative p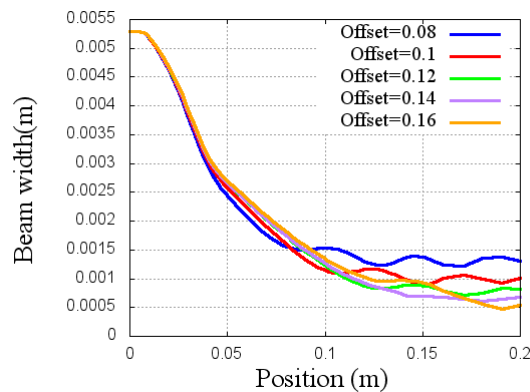osition thought not to be optimal. For example, Figure 5.38 shows a sweep of the normalised magnetic field (i.e. ± 20 % of the calculated current turns) for a non-optimal relative position (100 mm) showing that the scalloping is strongly influenced by changes in the magnetic field strength from the solenoid. Figure 5.39 shows a similar sweep of the normalised magnetic field (again ± 20% of the calculated current turns) but for the optimal position (140 mm), given by the previous results. As can clearly be seen, even large changes in the magnetic field produce a minimal change in the beam profile. Therefore, we can say that the insertion has been designed correctly.
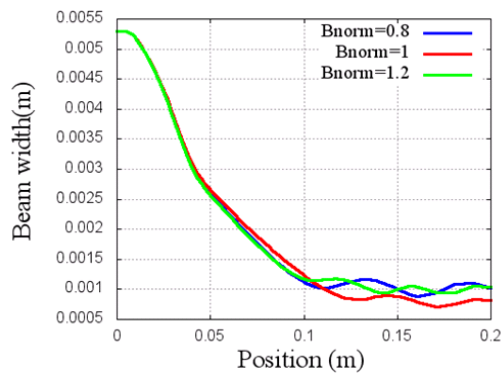
Figure 5.38 - Sweep of normalised magnetic field strength, fixed solenoid offset of 100 m and radius 50 mm.
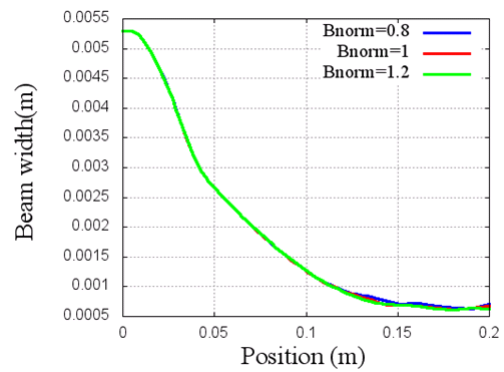
Figure 5.39 - Sweep of normalised magnetic field strength. Fixed offset (140 mm) and radius (50 mm).

5.3.4 Interim Conclusions

The basic theory of magnetic focussing of charged particles has been presented and used to understand and evaluate the different engineering decisions needed to produce an operational system. A solenoid with immersed flow insertion has been chosen, and the design was presented above. The electron gun presented earlier has been re-simulated with the magnetic field from the solenoid in place; the resulting beam has been found to be acceptable.

5.4 Collector

The electron beam must be contained within the vacuum chamber so a device, normally known as a collector, is used to gather the power from the beam. The most important function of the collector is to absorb the power from the beam in a way that does not affect the vacuum system. Obviously, the main problems that could occur are outgassing or simply evaporating a part of the collector. Therefore, the collimating magnet is generally truncated such that the beam diverges, increasing the area over which the beam strikes the collector.

Within experimental systems the collector is normally dissipative, with the beam simply striking the body of the collector, which has some form of cooling (air or water cooling, depending on the power level). In production systems, a much more complicated form of collector known as a depressed collector is used. This approach uses a bias voltage to decelerate the incoming electrons, allowing the energy of the beam to be recycled back into the power supplies of the electron gun. As only a small fraction of the beam energy is coupled into the wave (as the interaction slows the beam which must remain synchronised with the wave clearly the interaction is self-limiting) the majority of the efficiency within a TWT is due to the collector design. As the electron beam used here is low power (a few hundred watts) and has a fairly low current density (1 A/cm^2) then a simple copper or aluminium collector block with cooling fins can be used, although the vacuum pressure should be monitored closely.

5.5 Experimental Work

This section summarises the (unsuccessful) experimental attempt to construct a working TWT system. First there is a brief discussion about the choice of material used to construct the tube, followed by a trial of jointing techniques. Next there is a short summary of the design for manufacture and machining needed to fabricate the components of a working gun. The final section summarises the high voltage power supply designed and built to provide the accelerating voltage for the electron gun.

5.5.1 Material Choice

There are several recommended metals used for vacuum chambers such as: stainless steel, copper or sometimes aluminium. Stainless steel (usually 304 or 314) is the most commonly used because it has a good mix of machinability, ease of welding and good outgassing performance. As the electron beam uses a collimating magnet there is an additional requirement that the chamber needs to be non-magnetic, which is typically defined as a permeability of less than 1.004.

Whilst 304 stainless is austenitic (thus non-magnetic) certain manufacturing processes such as cold working and welding can locally change the crystal structure and introduce areas of higher permeability within the metal. Though these problems can be mitigated using careful process control, allowing the use of stainless steel in systems with extremely high magnetic fields, the complexities are far beyond in-house techniques and therefore it is not suitable for this specific application.

The obvious choice is then copper as it can be easily soldered, has good conductivity and acceptable vacuum performance though difficult to machine (compared to other metals). In addition, the high conductivity and good heat dissipation make it ideal for use within a slow wave structure for a travelling wave tube. However, the cost of manufacturing the entire structure out of copper is beyond this project therefore aluminium must be used.

Aluminium has key advantages of being cheap, non-magnetic, excellent machinability and reasonable vacuum characteristics. However, it has a major downside which is that welding aluminium, especially vacuum tight welds, is quite difficult and that brazing aluminium is considered to be extremely difficult and unreliable. As the former can be immediately ruled out due to cost this leaves a brazed aluminium construction as the only option for the tube, which is far from ideal.

The main issue with brazing aluminium is that that the oxide layer on top of the aluminium is extremely difficult to remove and verges on impossible (with normal workshop techniques) if the magnesium content of the metal is over a few percent, which is the case with certain common aluminium alloys. Therefore, it is recommended to use a low magnesium alloy (for example 1000 or 2000 series) and essential to avoid a high magnesium alloy (5000 series). Fortunately, the most commonly found alloys

(like 6061 or 6082) both have a borderline magnesium content so should be solderable using conventional techniques. Therefore, a test weld was carried out to confirm that the alumimum alloys available were solderable and that the joint that could be done by the author were vacuum tight. Figure 5.40 shows a picture of the 'top hat' added to a standard ISO flange which was chosen as it required two separate joints. The joints could then be tested by comparing the pump down rate and final pressure of the chamber shown in Figure 5.41 when a standard blank flange was used to that found when using the top hat. As both the pump down rate and final pressure (10e-6 mbar) were similar then the joints were clearly vacuum tight and the process used to create them was successful.

Figure 5.40 – Vacuum side of the test flange and a close-up of the atmosphere side of the joint n.b jointing has not been polished
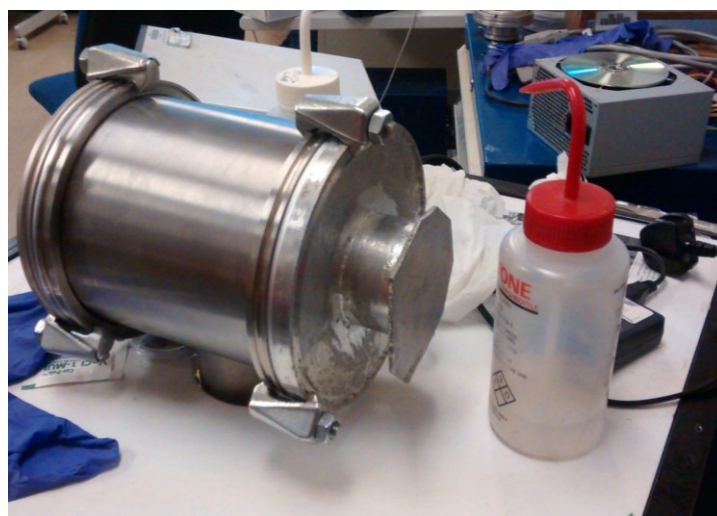

Figure 5.41 – Vacuum chamber with test flange mounted.

5.5.2 Design for Manufacture

5.5.2.1 Electron Gun

The theoretical electron gun design presented earlier is purely an inclined ground plane and a hemisphere with a beam aperture cut through, consequently several changes were needed to turn this into a practical system. Firstly, both parts need to be mechanically supported in a way that allows the gun to be aligned to the slow wave structure and without shorting the accelerating voltage between the electrodes. As the gun needs to operate under vacuum the entire system needs to fit inside a sealed chamber and be capable of mounting to the slow wave structure without comprising the vacuum performance of the system.

In addition, the design needed to take into account the restrictions imposed by conventional 3 axis machining using a mill and a lathe. The most important limitation is that there needs to be adequate clearance for the tool to fit inside the part, for example the cathode slope, length of the shell and minimum possible size of the cathode are all limited by the need to fit a boring bar inside the part.

Finally thought was given to the relative position of the parts, as some distances needed to be fixed with a good degree of precision, for example the centres of the cathode and anode must be on the same axis, whereas it is beneficial to be able to tune other dimensions to account for manufacturing tolerances elsewhere in the design such as the cathode-anode spacing.

Figure 5.42 shows a drawing of the final design. As can be seen from the diagram the electron gun is mounted onto a standard ISO vacuum flange with the electron gun protruding out of the rear of the flange where the slow wave structure could be attached. Mounting all the parts to the same plate allows a significantly more precise alignment, although it requires that the cathode is insulated from the anode/chamber which can be done using PEEK, a vacuum compatible plastic, pegs.

The lip of the anode has a tight fit inside the flange ensuring the centres (of anode and flange) are aligned and precisely defines the distance from the tip of the anode to the face of the flange. It should

be noted that the screws are simply for additional mechanical support so the assembly can be removed from the chamber rather than for alignment.

The cathode is held in place by the pair of arms. The design of the arms allows the inside edge of the groove and the side of the arm that mounts to the baseplate to be cut in a single operation ensuring that they are perpendicular. Unfortunately, the part must be rotated in order to drill the alignment holes, thus requiring careful machining fo the top edge of the arm so it can be indicated off. An alternative to this is to cut an alignment surface into the end of the arm although making this vacuum compatible would require a complicated series of vent holes. Therefore, a loss of precision was accepted as simulation results suggested that the beam performance of the gun was relatively insensitive to a small misalignment here.
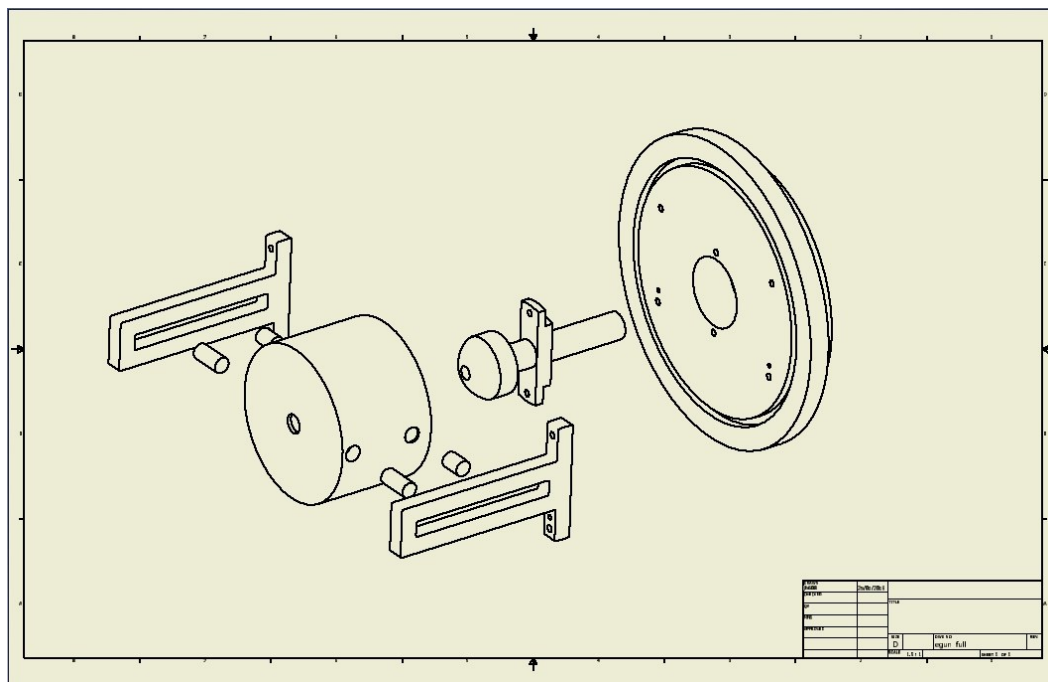

Figure 5.42 – Drawing of final design

Figure 5.43 to Figure 5.46 show pictures of the parts machined according to the drawing in Figure 5.42, as can be seen in the pictures the parts have good surface finishes (required for acceptable outgassing performance). Of particular note is the hemisphere of the anode with was ground by hand.

Figure 5.43 - Cathode

Figure 5.44 - Anode
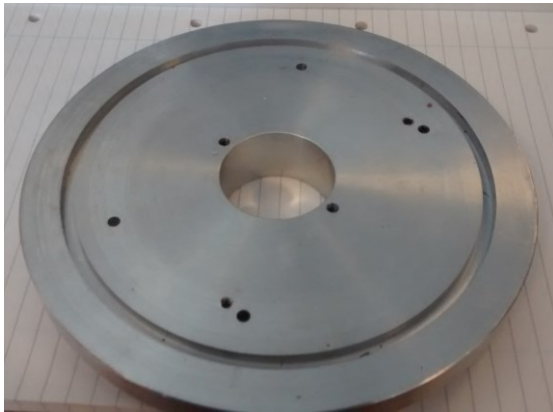
Figure 5.45 – Mounting flange

Figure 5.46 – Cathode support arms

5.5.2.2 Slow wave structure

The serpentine slow wave structure can be machined using normal split block techniques, where the groove is machined into two matching blocks (top and bottom) which are then brazed together. The advantage of this machining style is that the waveguide is split along the line of Electric symmetry thus the losses introduced by the brazed joint have a minimal effect on the circuit operation

As this is a simple structure there are fewer additional complexities compared to the electron gun. The first and most important is that the entire structure needs to fit inside the collimating magnet imposing a maximum size on the slow wave structure and any required waveguide tapers. Luckily the scaling laws are favourable here and the magnet bore diameter (determine by the required beam compression on the electron gun) neatly matches the size of the tube if the coupling tapers are positioned carefully.

The other limitation is that the electron beam needs to fit inside the beam tunnel. Due to machining tolerances it is possible that the electron gun will produce an electron beam of greater than the designed diameter. However, this could be compensated for by reducing the operating frequency of the serpentine structure and thus increasing the maximum permitted diameter of beam tunnel. Therefore, it is highly advantageous to machine the slow wave structure after the electron beam system has been built, aligned and measured.

5.6   Conclusions

A full electron beam stick consisting of a Pierce gun, tungsten wire cathode and solenoidal magnet has been designed. The electron gun has been designed with consideration to its machinability and to possess a tuning range that should compensate for some manufacturing imperfections. A low emissivity was used so a very conservative cathode design could be used. Modelling was then performed on the cathode to calculate a likely operating range. The beam is inserted into the collimating magnetic field using an immersed flow insertion, which has shown to be operating correctly. The gun was successfully machined and tested under vacuum, although as the cathode heater supply was not finished in time the complete assembly could not be tested. Table 5.8 summarises all the parameters of the final electron beam system showing that it meets the design goals.

Table 5.8- Summary of electron gun parameters.

Parameter	Symbol	Value	Units
Accelerating voltage	V_0	8.3	kV
Normalised velocity	u_0	0.18c	
Beam current	I_0	29	mA
Beam radius	r_b	1	mm
Beam power		240	W
Heater current		<50	A
Filament diameter		1	mm
Filament standoff		50	mm
Magnet diameter		100	mm
Magnet offset		140	mm
Magnet required field strength		~0.05	T

References

[1] Kimball Physics, "An introduction to electron and ion guns," Available:

http://www.kimphys.com/electron_guns/catalog_PDFs/Gun_intro_prelim.pdf

[2] G. R. Brewer, "Some characteristics of a magnetically focused electron beam," *Journal of Applied Physics,* vol. 30, no. 7, pp. 1022-1038, 1959.

[3] H. G. Kosmahl, "Modern multistage depressed collectors—A review," *Proceedings of the IEEE,* vol. 70, no. 11, pp. 1325-1334, 1982.

[4] C. Süsskind, "Electron guns and focusing for high-density electron beams," in *Advances in Electronics and Electron Physics*, L. Marton, Ed. no. v. 8): Elsevier Science, 1956.

[5] J. R. Pierce, "*Theory and design of electron beams*," Van Nostrand, New York, 1954.

[6] E. Linder and K. Hernqvist, "Space-charge effects in electron beams and their reduction by positive ion trapping," *Journal of Applied Physics,* vol. 21, no. 11, pp. 1088-1097, 1950.

[7] J. R. M. Vaughan, "Synthesis of the Pierce gun," *IEEE Transactions on Electron Devices,* vol. 28, no. 1, pp. 37-41, 1981.

[8] A. S. Gilmour, *Klystrons, Traveling Wave Tubes, Magnetrons, Crossed-field Amplifiers, and Gyrotrons*. Artech House, Boston, MA, 2011.

[9] Kimball Physics "ES-020 Tungsten (W) Filament," Available:

https://www.kimballphysics.com/PDFs/cathode_specs_W.pdf

[10] R. Jenkins and W. Trodden, "The poisoning of thoriated tungsten cathodes," *International Journal of Electronics,* vol. 12, no. 1, pp. 1-12, 1962.

[11] D. J. Griffiths, *Introduction to Electrodynamics*. Prentice Hall, New Jersey, 1999.

[12] L. Brillouin, "A theorem of Larmor and its importance for electrons in magnetic fields," *Physical Review,* vol. 67, no. 7-8, p. 260, 1945.

[13] Omega Engineering Ltd., "Table of total emissivity," Available:

https://www.omega.co.uk/temperature/Z/pdf/z088-089.pdf

[14] A. Worthing, "The true temperature scale of tungsten and its emissive powers at incandescent temperatures," *Physical Review,* vol. 10, no. 4, p. 377, 1917.

[15] R. D. Allen, L. F. Glasier Jr, and P. L. Jordan, "Spectral emissivity, total emissivity, and thermal conductivity of molybdenum, tantalum, and tungsten above 2300 K," *Journal of Applied Physics,* vol. 31, no. 8, pp. 1382-1387, 1960.

[16] G. Kuznetsov, "Cathodes for electron guns," *Physica Scripta,* vol. 1997, no. T71, p. 39, 1997.

[17] E. L. Murphy and R. Good Jr, "Thermionic emission, field emission, and the transition region," *Physical review,* vol. 102, no. 6, p. 1464, 1956.

[18] S. Yamamoto, "Fundamental physics of vacuum electron sources," *Reports on Progress in Physics,* vol. 69, no. 1, p. 181, 2005.

[19] I. Langmuir, "The effect of space charge and residual gases on thermionic currents in high vacuum," *Physical Review,* vol. 2, no. 6, p. 450, 1913.

[20] S. Tanaka and Y. Ohara, "Tapered tungsten filament for a long life cathode," *Review of Scientific Instruments,* vol. 55, no. 10, pp. 1625-1631, 1984.

[21] Electron Microscopy Sciences, "Cathodes for Electron Microscopes," Available: https://www.emsdiasum.com/microscopy/products/brochures/cathodes.pdf.

[22] Spectra-mat inc, "Guidelines for Processing of Dispenser Cathodes," Available:

http://www.spectramat.com/pdf/TB-147-

D%20Guidelines%20for%20Processing%20of%20Dispenser%20Cathodes.pdf

[23] Spectra-mat inc, "Handling and care of cathodes," Available:

http://www.spectramat.com/pdf/TB-106-

C%20Handling%20and%20Care%20of%20Cathodes%2001-13.pdf

[24] T. S. S. Dikshith, *Hazardous Chemicals: Safety Management and Global Regulations*. Taylor & Francis, New York, 2013.

[25] Wikipedia article "Hot Cathode", Available:

https://upload.wikimedia.org/wikipedia/commons/3/37/LaB6HotCathode.jpg

[26] 3M Advanced Materials Division, "3M Tungsten Dispenser Cathodes", Available:

http://multimedia.3m.com/mws/media/968840P/3m-tungsten-dispenser-

cathodes.jpg?boundedSize=310

[27] W. Harbaugh, "Tungsten, thoriated-tungsten, and thoria emitters," *Electron Tube Design,* pp. 90-98, RCA,New Jersey, 1962.

[28] S. Sharma, *Objective Physics*. Krishna Prakashan, Delhi, 1994

[29] RCA, "Types of cathodes," 1943, Available:

http://www.tubebooks.org/tubedata/HB-3/General/Types_of_Cathodes.pdf

[30] H. D. Young, R. A. Freedman, and A. L. Ford, *Sear and Zemansky's University Physics: with Modern Physics*, ed: Pearson Education Inc, San Francisco, 2008.

[31] International Tungsten Industry Association, "Tungsten Properties", Available:

http://www.itia.info/tungsten-properties.html

[32] Pasco Scientific, "Temperature and Resistivity for Tungsten", Available:

http://physics.usask.ca/~bzulkosk/Lab_Manuals/EP354/ep354_thermal-radiation-lab_Tungsten-Temp-Resistivity.pdf

[33] G. R. Brewer, "Some characteristics of a cylindrical electron stream in immersed flow," *IRE Transactions on Electron Devices,* vol. 4, no. 2, pp. 134-140, 1957.

6   Conclusions

Within this thesis, several aspects of travelling wave tube design have been covered: the design of a serpentine travelling wave tube, improvements to the serpentine slow-wave structure, and possible application of photonic crystals as alternative slow-wave structures.

In Chapter 2 the small signal theory of travelling wave tubes was first introduced, and then applied to the specific case of a serpentine slow wave structure. The traditional analysis was used to derive a set of design equations, which were then verified by using them to synthesise a serpentine TWT that was then successfully simulated using modern numerical techniques.

In Chapter 3, the high frequency operation of the serpentine slow wave structure was covered. A survey of approaches used to extend the operating frequency was presented and used to identify a gap in the literature: the exploitation of spatial harmonics. Analysis was then performed to see if a higher harmonic design offered any advantages over fundamental operation. This analysis showed that operating a serpentine on the second peak of the coupling impedance reduces the aspect ratio of the design and could allow a larger beam tunnel. Whilst the interaction impedance is lower, the ohmic losses are also reduced and significantly more current can be passed through the beam tunnel, for the same current density. Alternatively, rather than enlarge the beam tunnel, this approach could allow the rest of the structure to be miniaturised, allowing higher frequency operation for a given beam diameter. Ultimately, whilst the design does work as an amplifier, it might be better suited for use as a backward wave oscillator, a promising topic representing an avenue for further work.

In Chapter 4, the use of photonic crystals within slow wave structures for travelling wave tubes was investigated. As the topic is new the literature survey mainly covered passive device applications in this case. A coupled-cavity hole-based photonic crystal, often called a coupled resonator optical waveguide (CROW), was then studied to see if it could be used within a travelling wave tube. This type of structure is highly suitable for high frequency operation as it is all-dielectric, self-supporting and has been fabricated up to optical frequencies. Several cavity types were evaluated with the most suitable found to be a chevron style cavity. Beam coupling was also briefly considered, it is thought that the beam

could be placed outside the structure (as been done elsewhere) which is a significant advantage over other types. However further work is required, especially to study the interaction impedance and suitable coupling structures.

Finally, Chapter 5 covers the design work carried out for a possible experimental verification of a complete travelling wave tube. A full electron beam stick was designed, with calculations and simulations provided for a Pierce gun, tungsten wire cathode and a solenodial collimating magnet. The electron gun was specifically designed for in house machining capabilities, possessing a good post-production tuning range to compensate for low tolerances and a geometry that offered adequate clearances for tooling. The system was designed for a low cathode emissivity, allowing conservative material parameters to be used for the cathode design, significantly reducing risk. The cathode was modelled using standard analytical techniques to determine a likely geometry and operating current. Design equations for an immersed flow insertion were derived, and used to design a solenoid magnet for beam collimation. Finally the entire design was verified through numerical simulation techniques.

The overall conclusion of this work is that travelling wave tubes, originally invented over half a century ago and the mainstream of high-bandwidth, long-distance telecommunications ever since, have significant prospects for further development, allowing higher powers to be reached at higher frequencies than ever before.

Suggestions for Further work

The most obvious suggestion for further work would be to build and experimentally verify operation of the higher-harmonic serpentine structure. Also of interest would be to carry out additional theoretical work to investigate whether even larger beam tunnels could be used, if some of the techniques used by other authors were to be applied in conjunction with high-b operation.

For photonic crystal structures, the next steps would be to develop mode transducers and a sever so that a full crystal can be simulated in a basic frequency domain solver. Key tasks would be to check the phase characteristics, and verify single-mode operation. If the simulations are successful, further PIC

simulations would be needed to confirm that the structure was capable of coupling to an electron beam. Further work could also be done to investigate the interaction impedance and consider how the crystal parameters could be changed to increase the strength of the fringing field and hence the coupling to the electron beam.

Finally, it would be of interest to consider how the photonic crystal structure could be used in a solid state travelling wave tube, where the drift current in a semiconductor is used instead of an electron beam. Previous work in this area has shown some promising results (for example, a difference in insertion loss with and without a bias current) but no net terminal gain. The proposed structure should have significantly lower loss than those previously studied, and a coupled cavity structure, with infinite higher harmonics, is ideal for synchronizing with a drifting beam, which moves much more slowly than a vacuum beam (thus needing a very large slow wave factor), and consequently warrants further study. However, resistive heating by collisions between the electrons and the lattice would be a major concern, and would almost certainly limit application to low-power, high frequency devices.